Control Algorithm Design, Testing, and Use Cases for the INSTAR [INertial STorage And Recovery] System

A Flywheel-Based Dedicated High-Power Energy Storage System for Improved Hybrid Vehicle Fuel Efficiency and Performance with Special Application in Urban Commercial Vehicles

By

John Michael Madura

A Dissertation submitted in partial satisfaction of the requirements for the degree of

Doctor of Philosophy

in

Engineering - Mechanical Engineering

in the

Graduate Division

of the

University of California, Berkeley

Committee in charge:

Professor Dennis K. Lieu, Chair

Professor George C. Johnson

Professor Seth R. Sanders

Fall 2018

Control Algorithm Design, Testing, and Use Cases for the INSTAR [INertial STorage And Recovery] System

A Flywheel-Based Dedicated High-Power Energy Storage System for Improved Hybrid Vehicle Fuel Efficiency and Performance with Special Application in Urban Commercial Vehicles

by

John Michael Madura

Abstract

Control Algorithm Design, Testing, and Use Cases for the INSTAR [INertial STorage And Recovery] System

A Flywheel-Based Dedicated High-Power Energy Storage System for Improved Hybrid Vehicle Fuel Efficiency and Performance with Special Application in Urban Commercial Vehicles

by

John Michael Madura

Doctor of Philosophy in Engineering - Mechanical Engineering

University of California, Berkeley

Professor Dennis K. Lieu, Chair

This thesis describes the design of control algorithms, modelling, testing, and analysis of use cases of the INSTAR system, a dedicated high-power, low cost energy storage system designed to increase energy efficiency and performance in hybrid vehicles, with special application in urban commercial vehicles. The system is intended to be combined with an electrochemical battery and small energy generator to provide 3 distinct magnitudes of power delivery and absorption to the traction motors. The advantages of such a system would be decreased generator size, decreased component size, and potentially increased battery service life.

Flywheel control algorithms were developed and tested to absorb excessive electrical energy during regenerative braking, as well as to augment electrochemical battery power during vehicle accelerations. During laboratory testing battery charging currents reaching the battery were controlled through modulation of flywheel throttle signals. These algorithms were applied in road driving conditions to decrease vehicle energy use by 8.9 percent over a predetermined acceleration and deceleration event while decreasing the charging rate of the battery. Laboratory testing showed potential to reduce battery discharge rate during acceleration events by pre-charging the flywheel so that it may be discharged during the acceleration event. Road tests demonstrated that energy use could be reduced by 2.6% over a pre-determined acceleration and deceleration event while simultaneously reducing the magnitude of battery discharge current by around 15%.

Such a system has use in urban vehicles where much of the vehicle driving is in stop and go type traffic. These vehicles typically have a large internal combustion engine to accelerate the vehicle from a stop. The INSTAR system may be able to reduce the engine output requirement while still providing the same performance. The INSTAR system is particularly applicable in commercial vehicles where fully electric vehicle may not be practical.

Contents

Chapter I: Introduction

This thesis describes the testing of a novel triple hybrid vehicle. This vehicle is similar to the hybrid vehicles on the road today, but also incorporates an electromechanical flywheel. It is the continuation of work started in 2009 at the University of California, Berkeley in the mechanical engineering department.

Section 1.1 Background

Few technological advances have had the widespread impact on society that the automobile has. For many, the car is more than just a mode of transportation, it is a symbol of independence and freedom. Before the advent of the automobile, transportation was limited to walking, which is slow, horses, which are troublesome to maintain, and trains and ships, which are restrictive in the destinations they serve. The automobile set the average individual free to travel as they wish, and explore the vast stretches of our great world. Such a great innovation is the automobile that it has become a pop culture icon. The automobile has become the subject of songs, motion pictures, magazine, and has spawned a large customization market allowing owners to customize their cars to play off their image.

Though the automobile has been an undeniably great innovation, the underlying technology has changed little since it was invented. The average vehicle still uses an internal combustion engine running on either gasoline or diesel fuel, and fuel economy is not much improved over the vehicles of years past. In today's world of changing climate, we must be careful to not let our want of travel independence irreversibly harm the environment we depend upon to live.

Greenhouse gas emissions (GHG) have increased in the transportation sector and accounted for 33.4% of USA CO_2 emissions from fossil fuel combustion [1]. Of the 33.4%, 60% is from light duty passenger vehicles and light duty trucks less than 8,500 lbs. In an effort to reduce the impact on GHG production, the U.S. EPA required that manufacturers meet an average fuel economy of 35 mpg by 2016 for all light duty vehicles [2]. To accomplish this goal, many manufacturers increase production of hybrid vehicles, which have several benefits related to increased fuel economy, one of which is the ability to recover energy during braking (regenerative braking).

The U.S. government has put into law a Corporate Average Fuel Economy (CAFE) Standard requiring that manufacturers greatly raise their average passenger car fleet efficiency by 2025 [3]. The CAFE standard is based on a production of CO_2 emissions of 163 gram/mile fleet average production, which means that if manufacturers were to accomplish this by fuel economy alone, the fleet average fuel economy would be equivalent to 54.4 mpg by 2025. Because of American's affinity for large trucks and sport utility vehicles, reaching a fleet wide average of 54.4 mpg may require that small hybrid style vehicles have fuel economies of 75 mpg or more. More efficient regenerative braking is a way that fuel economy can be further increased along with more efficient engine and electric motor combinations.

Though hybrid vehicles are common on the roads today, much more work and innovation are needed to further reduce their fuel consumption to bring greenhouse gas emission to an acceptable level. Furthermore, a decrease in fuel consumption may decrease the cost of operating a vehicle to the owner. This work is intended to investigate an electromechanical flywheel to increase the efficiency of hybrid vehicles to meet the needs of next generation road travelers.

Chapter II: State of the Art

Section 2.1 Hybrid Vehicles

Modern vehicles come in three common varieties; conventional internal combustion type vehicles, full electric vehicles, and hybrid vehicles. Conventional and full electric vehicles rely upon a single energy source to propel the vehicle, while hybrid vehicles utilize both an internal combustion engine (ICE) and electric motors to propel the vehicle. Hybrid type vehicles come in many different architectures ranging from the traditional type where the electric motors act as auxiliary drive devices to the ICE, to the more recent plug-in type hybrids, where only electric motors are used to propel the vehicle, and the ICE is used solely as a generator to recharge the electrochemical batteries. This study will focus mostly on the more traditional type of hybrid vehicle where the electric motors are used as an auxiliary to the ICE.

In this type of hybrid vehicle, increases in efficiency come from the ability to recapture energy from regenerative braking, and from the ability to not operate the ICE when only low levels of power are needed to propel the vehicle. Regenerative braking is when the electric motors usually used to propel the vehicle are instead used to slow the vehicle down. When the electric motors are used in this mode, they generate an electric current which can be used to charge the battery. In a conventional internal combustion engine vehicle, this energy would instead be dissipated as heat through the friction brakes located on each wheel. Rather than waste this energy, the hybrid vehicle is able to recapture it, and re-use it. The amount that can be captured is limited by the capabilities of the vehicle technology, which will be discussed later in this paper.

There are several technologies which may be employed to create hybrid vehicles, not all of which require electric motors or batteries for operation, though this is the most common configuration seen on the road today. This study will focus on the hybrid vehicle system consisting of an internal combustion engine, electric motors, and an electrochemical battery. Internal combustion engines and electric motors are well studied, and fully developed technologies. However, batteries, especially the lithium-ion batteries seen on modern electric type vehicles, are only moderately developed, and have several issues which are holding back the efficiency potential of hybrid vehicles. This study focuses on the addition of a dedicated high-power device to the existing hybrid vehicle platform, which may offset some of the short comings of electrochemical batteries.

Section 2.2 Batteries

At the core of electric and hybrid vehicles lie the battery packs. These battery packs are typically either NiMH or Li-ion in construction, and range in size depending on the vehicle. The first commercially available hybrid vehicles utilized NiMH batteries, but as Li-ion battery technology improves, a trend toward Li-ion batteries has been observed. Although these batteries have great energy density [Wh/kg], they typically have relatively lower power densities [W/kg] when compared to other energy storage technologies discussed later [4].

Batteries are susceptible to degradation during use, and degradation is the main reason for battery replacement or failure. Battery end of life is normally defined as when the battery reaches a 20% reduction in storage capacity, or a 100% increase in internal resistance [5]. Degradation occurs from a variety of factors within the internal chemistry and structure of the battery, but the two most major are the number of charging cycles, and the temperature of the battery.

It has been shown that Li-ion batteries are highly sensitive to charging rate, however are relatively insensitive to discharging rate. It is common to display the battery currents in terms of C-rate, and the current may be displayed as 1C, 2C, 2.5C, 3C, etc. 1C would be 1 times the C-rate for any given battery, where the C-rate is the discharge current which would empty the battery in 1 hour if discharged at the rated voltage. The concept of C-rate will be important for full understating of this work.

Li-ion batteries are sensitive to even small changes in charging rate. An increase in the charging rate could decrease the battery capacity 60% over an identical battery after 500 cycles if the charging current is increased from 1.0 C to 1.4 C. In the cited study, a battery charged at 1C experienced around a 15% degradation as seen in Figure 1, however, a battery charged at 1.4 C experienced around a 75% degradation [6].

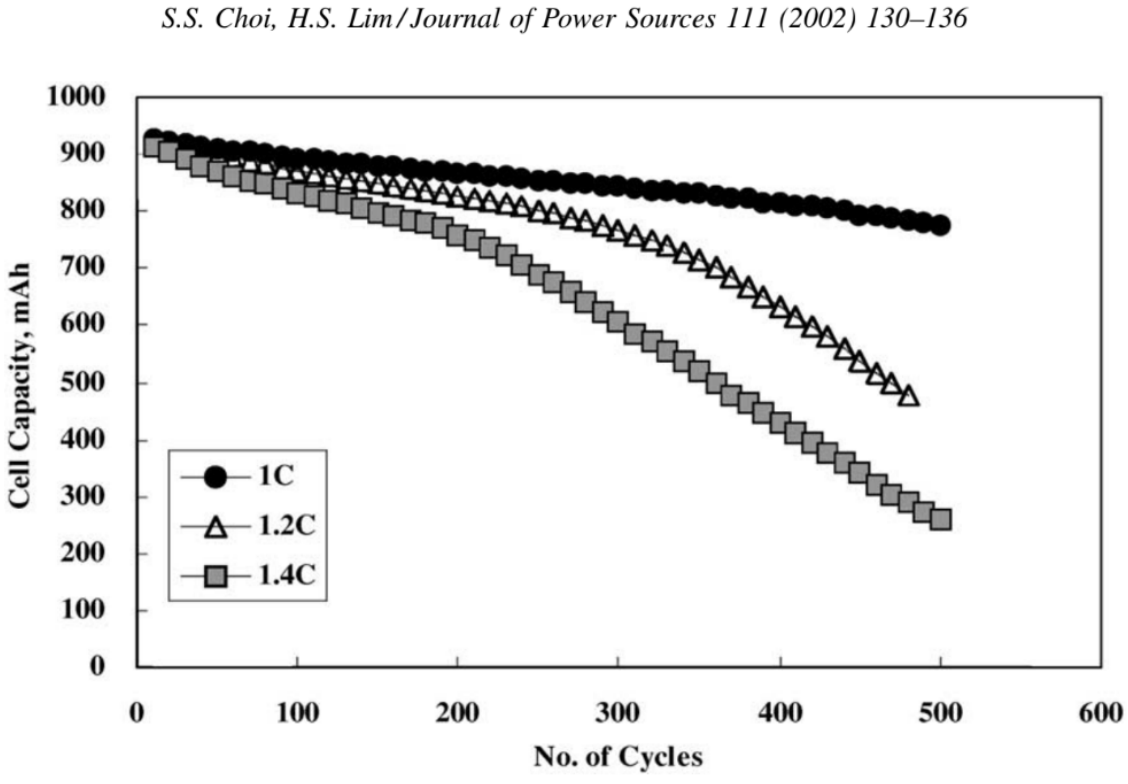

Figure 1: Capacity Fade vs Number of charging cycles for variable charging rates, reproduced from Choi et al. [6].

Though batteries are also sensitive to discharging rate, they appear to be less sensitive. Capacity fade only increased to 13.2% from 9.5% when discharging rate is increased from 1C to 2C over 300 cycles, as seen in Figure 2 [7].

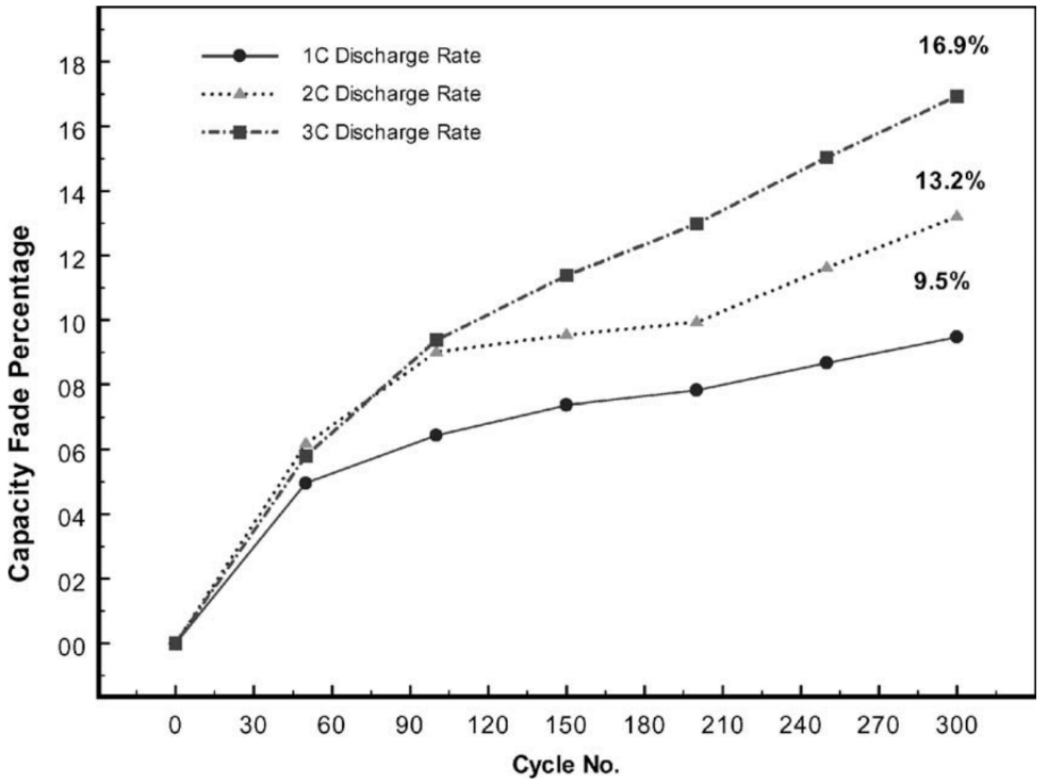

Figure 2: Capacity fade vs number of cycles for variable discharging rates, reproduced from Ning et al. [7].

An additional factor that can adversely affect battery life are elevated temperatures. Elevated temperatures of 60^{o}C have been shown to reduce battery capacity by as much as 65% Figure 3 [8], and play a large role in battery cell degradation [7]. Increased charging and discharging rates are known to increase the internal temperature of Li-ion battery packs [7]. This phenomenon can easily be felt by touching the surface of a charging or discharging battery pack, and increased charge and discharge rate have been shown to increase the battery pack temperature in hybrid vehicles [9].

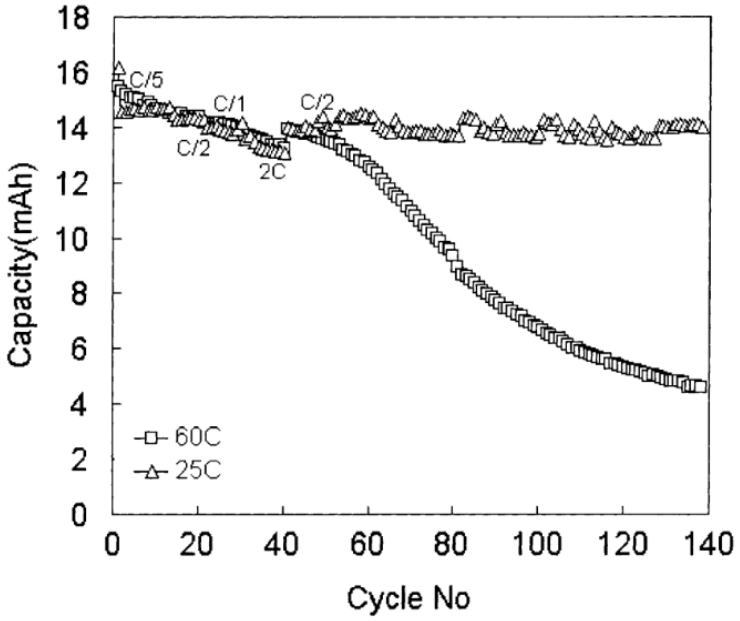

Figure 3: Battery capacity v number of cycles for batteries at 25C and 60C, reproduced from Shim et al. [8]

Section 2.3 Regenerative Braking

A DC motor can operate in 3 states, coast, where no power is being drawn or directed to the motor windings, drive mode, where power is being directed through the windings to apply a torque to the output shaft of the motor, and generator mode, where an input torque is used to generate electrical power in the windings and send it away from the motor. In many electric vehicles today, when a driver depresses the brake pedal, some amount of the braking effort is regenerative braking, and is used to provide power back into the vehicle's batteries. The remainder of the braking is usually accomplished with conventional friction type brakes. Regenerative braking can have an overall positive effect on the vehicle's range of operation, or fuel efficiency for hybrid vehicles, especially in heavy traffic situations [10].

An issue which needs to be addressed when implementing a regenerative braking system in a vehicle is that batteries are limited in the amount of charging power they can sustain while maintaining battery service life. Many manufacturers have limited the amount of energy recovered during regenerative braking [9]. This becomes especially relevant in hybrid vehicles where the battery packs are small, and the amount of available braking power exceeds what the battery pack can sustain, necessitating a significant amount of energy be dissipated as heat through the friction brakes of the vehicle. Research on round trip efficiencies, where the vehicle is accelerated from an initial zero velocity to some cruising velocity then decelerated back to a final zero velocity, has shown current hybrid vehicles are only capable of a maximum 35% round trip efficiency during a 30 mph to 0 mph, to 30 mph cycle [11]. Research has been conducted to evaluate methods of capturing this excess power using alternative methods of energy storage.

The low efficiency of regenerative braking limits the effectiveness of the hybrid vehicle, which gain much of their efficiency from the ability to recapture this energy, reducing energy waste. With the increase in minimum fuel economy required by the EPA, more of this energy must be recaptured if brands are to meet the minimums cross their fleets. The problem is that energy recovery is at the moment, limited by battery technology. A solution to the problem is to place a secondary energy recovery device in the system to absorb the energy which would otherwise be rejected.

Section 2.4 Types of Secondary Energy Recovery Devices

This work focuses on a triple hybrid model, where there are three energy storage or generating devices within the vehicle. It is assumed that two of those devices are decided, one being a lithium-ion battery, the other being an electromechanical flywheel battery. The third device could be an internal combustion engine, hydrogen fuel cell, solar panels, or some combination. Even though this work will focus on the integration of an electromechanical flywheel, it is important to note that there exist other technologies at play in the field. The most ideal technology for an automobile would be one with both a high power and high energy density. Gasoline internal combustion engines have been widely used in automobiles because they do provide both a high energy and high power density, allowing them to be used as standalone units to propel the automobile, despite the downside of being relatively inefficient [12]. None of the technologies being researched or implemented to replace or augment the gasoline engine have the same combination of power and energy density of the gasoline engine, as seen in Figure 4.

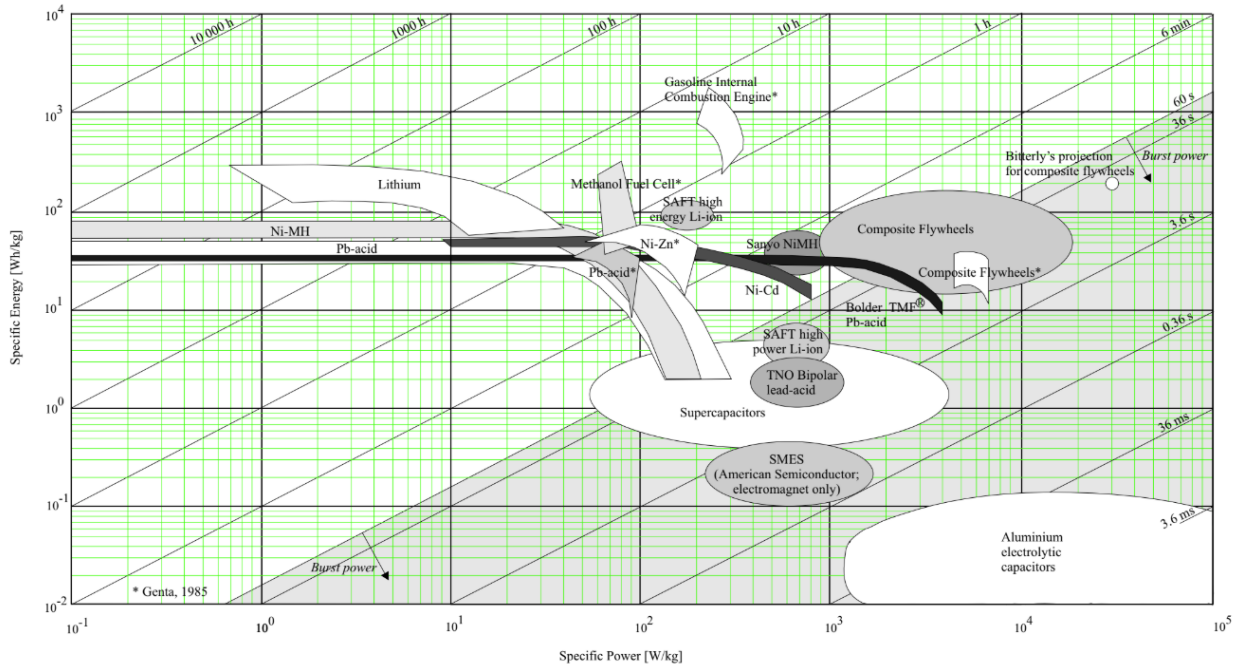

Figure 4: Energy and power density of several energy storage technologies, reproduced from Holm et al. [12]

Section 2.4.1 Hydraulic/Pneumatic Energy Recovery

Hydraulic and pneumatic energy recovery systems are one option for auxiliary energy storage in hybrid vehicles. In these systems, energy is stored in a hydraulic or pneumatic accumulator and can be released on command (Figure 5). This is accomplished through the use of a pump and accumulator [13]. Inside the accumulator is often a bladder containing a gas which is pressurized as the pump does work on the fluid to move it into the accumulator [14]. The benefits of such a system are that hydraulic/pneumatic systems are well understood, and do not introduce any high-speed devices into the vehicle which could affect its dynamics [15]. These systems have high power densities of around 10,000 kW/kg, but relatively poor energy densities of around 1 kWh/kg. Such systems also may require additional mechanical systems be fitted directly to the drivetrain of the vehicle, which poses a packaging problem. The so far implemented systems are also heavy and large, and thus are most relevant to large vehicles such as delivery trucks [16]. The work here is targeted at smaller consumer and commercial vehicles, and thus other technologies are investigated.

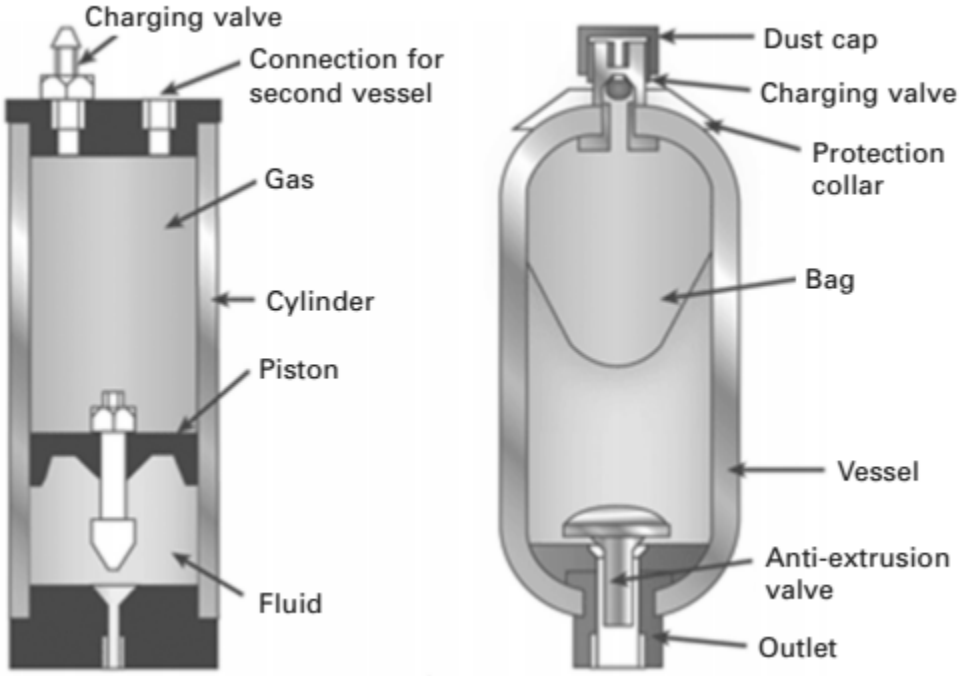

Figure 5: Schematics of Hydraulic/pneumatic accumulators. Piston type (Left) and bladder type (right) [13].

Section 2.4.2 Capacitors

To safely capture more of the energy available from regenerative braking, some researchers have implemented capacitors in vehicles to store otherwise battery-harming braking energy [17] [4] [18]. An example of such a vehicle can be seen in Figure 6. These capacitors are attractive because of their lack of moving parts, elimination of mechanical inefficiencies in their operation, and very high power densities of around 1000 W/kg. Ultra-capacitors are still improving as new technology emerges, but are still in a development stage, are prohibitively

expensive, and have relatively low energy densities of around 1 Wh/kg. They are however being investigated as a replacement for batteries in fuel cell vehicles, as the use of an ultra-capacitor may actually yield a lower cost per km travelled than batteries [17].

Figure 6: Ultra-capacitor powered truck [4]

Section 2.4.3 Flywheels

Flywheels have been used for many decades as mechanical energy storage devices, their design, and operating principles are well understood. They represent an attractive option because of their small size compared to hydraulic systems, low cost as compared to ultra-capacitors, and high power density as compared to batteries [19]. Flywheels were developed for use in conjunction with an ICE as an auxiliary power storage device in 1964, with application potentials in buses and passenger cars [19]. In these early applications, the flywheel acted as a buffer between the ICE and driveline, allowing the ICE to operate at peak efficiency independent of vehicle speed.

More recently, researchers have implemented flywheels to recover kinetic energy that would otherwise be lost as heat through friction braking. Systems installed in conventional, non-electric vehicles have been shown to increase fuel economy by 22% for cars, and 33% for buses, by virtue of having the ICE shut down when the flywheel is spinning [19]. There are several companies, such as Flybrid-Torotrak (Figure 7), pursuing a mechanical, flywheel based kinetic energy recovery system. Flywheel systems are also used in Formula 1 racing to recover energy from braking and provide higher acceleration after braking.

Figure 7: Flybrid system in place in Jaguar Test Vehicle [11]

For hybrid electric vehicles, electromechanical flywheels have been researched and developed to increase mileage and fuel economy of the vehicles. These electromechanical devices are sometimes called flywheel batteries, or electromechanical batteries [19]. These systems have been shown to be between 4% and 6% smaller in size than a comparable ultracapacitor or battery respectively, and cost about the same or less than a comparable battery and about 2.8 times less than a ultracapacitor [20]. A notable example of such a system are the 17 urban buses in Switzerland equipped with electromechanical flywheels that have been in service since 1988 [11]. These systems have approximately 60,000 hours, or 1 million cycles each, and are claimed to have a brake cycle round trip efficiency of 87% (Figure 8). A similar system was successfully installed on a fuel cell bus operating in Austin, TX [21]. These examples show potential for flywheel energy recovery for use in buses and other large vehicles.

Figure 8: L-3 Communications Magnet-Motor GmbH fitted to an urban hybrid bus [11]

Chapter III: INSTAR Test Kart

The INSTAR flywheel system is not new to this study and has been operational for previous research projects [22]. The flywheel and testing platform were developed to demonstrate the possibilities a flywheel energy recovery system can add to a hybrid electric vehicle. The goal of the INSTAR lab is to test the impacts a low-cost flywheel can have on the efficiency, environmental impact, and performance of a hybrid vehicle. One goal of the research project is to create a low-cost system which may be applicable to the economically priced urban commuter cars found in the United States.

Section 3.1 INSTAR Flywheel

The flywheel of the INSTAR system is comprised of an 8-inch diameter, 1-inch thick stainless steel rotor mounted to a spindle, and supported by 2 deep groove ball bearings. The flywheel in the INSTAR system can spin up to 25,000 RPM, having maximum energy storage of 113 kJ. The flywheel is powered by a 24kW motor rated at the same voltage as the INSTAR battery packs to eliminate the need for a DC-DC converter. The rotor of the motor is directly mounted to the flywheel spindle and is of a 4-pole design utilizing 42 MGOe neodymium permanent magnets. The stator is a 6-tooth design utilizing 0.007” thick M19 silicon steel laminations and allowing for a 0.020” air gap between rotor and stator. An image of the flywheel as well as a cross section can be seen in Figure 9.

The Motor is controlled by a commercially available Sevcon Gen4 controller, which was tuned with the help of Mr. Raul Agulair at ElectricMotorSport of Oakland, Ca. The Gen4 controller is specifically designed to be used with 3 phase DC brushless motors or 3 phase AC induction motors. They are commonly used in vehicle type applications and have regenerative braking capability built into the internal control algorithms. The GEN4 controller can be controlled with a throttle, brake, and forward/reverse switch, or can be controller with supervisory control via a CAN bus.

In previous research, much work has been done to create a safe and high performing device. Different bearing lubricants, grease and oil, as well as the effect of vacuum was tested to determine their efficacy [22]. The design in use was selected for its low cost, durability, and performance.

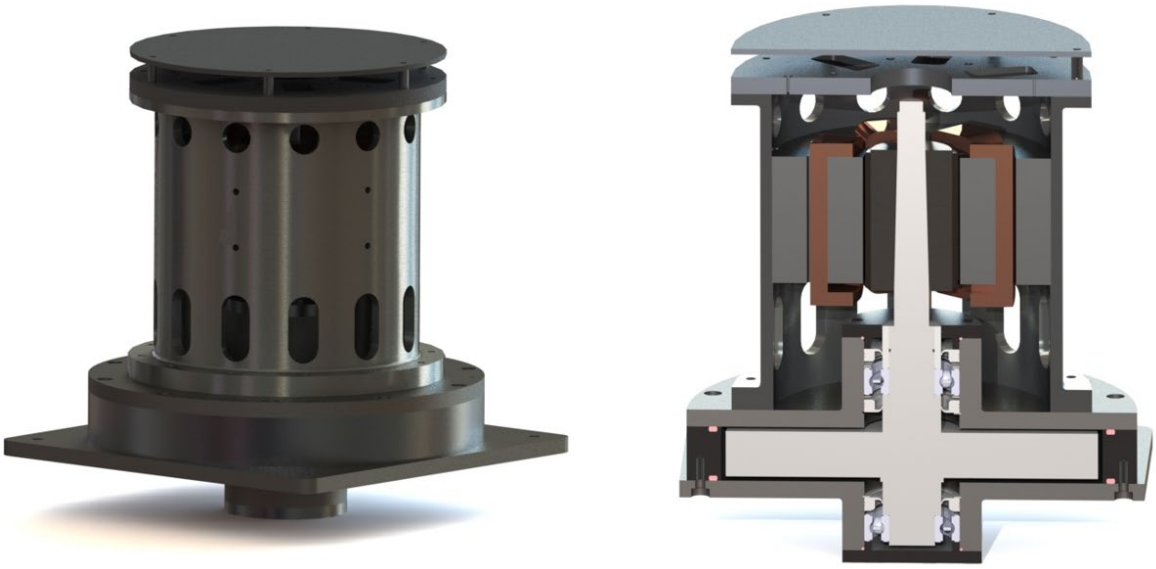

Figure 9: INSTAR Flywheel and Flywheel Cross Section [22].

Section 3.2 Testing Platform

The testing platform for the INSTAR is designed to resemble a vehicle. Because of laboratory constraints, the platform consists of only the electrical components of a hybrid vehicle. The use of a combustion engine would require ventilation systems be installed in the lab, as well as fire suppression systems in case of fuel fires. Because of this, and because the goal of the project is to determine the feasibility of the incorporation of a flywheel into a vehicle, not to create a fully functioning vehicle, it was determined that an internal combustion engine is not necessary for the experiments. A small Go-kart was chosen as the chassis for the experimental set up because it can be easily maneuvered in and out of the lab for real world testing, and is set up in a fully electric configuration.

The go kart uses two traction motors. These are 12 kW, DC brushless Mars Motors with a maximum speed of 5,000 RPM, and a stall torque of 53 N*m. The motors are rated for 80 amps with continuous operation, and can surge up to 300 amps for 1 minute. The motors are capable of 53 N*m of regenerative braking torque, which can provide up to 290 amps based on the 0.7830 N*m/amp torque constant. The motors are controlled via separate Sevcon Gen4 motor controllers. The motors operate independently to allow for different motor speeds while executing vehicle turns. The traction motors power the wheels through a chain drive system.

The battery packs on the kart platform are two 20Ah, 80V LiFePO4 battery packs connected in parallel, providing the equivalent of a 3.2 kWh battery pack. Lithium-ion battery pack chemistry was chosen because it is widely thought that lithium will replace nickel metal halide battery packs for vehicle applications [7]. The battery pack size for the vehicle was chosen to provide reasonably long testing sessions without back up power. They are however larger than

the typical battery pack found on a commercially available hybrid vehicle. The battery packs on commercially available vehicles are generally between 5 and 10 Ah, and operate under various voltages based on the other hardware of the hybrid vehicle. The larger battery packs of this kart mean that the C-rate of the battery is larger than that of a hybrid vehicle with the same rated voltage, and thus these batteries can sustain more regenerative braking before battery pack damage. An image of one of the battery packs can be seen in Figure 10.

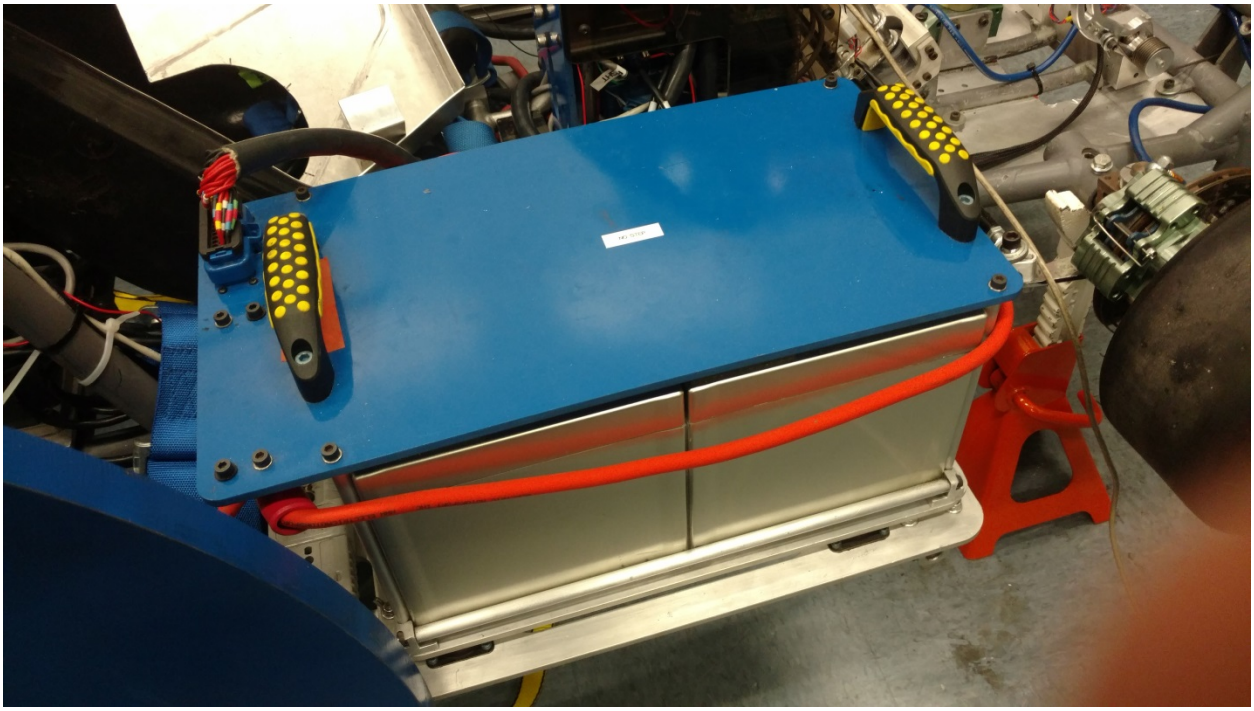

Figure 10: One of the Two INSTAR Battery Packs

To monitor the current leaving and entering the battery packs, a Temura L03S200D15 hall effect current sensor was placed in the system. The sensor is non-invasive and reads the electromagnetic field surrounding the power cables to determine battery charge or discharge current. This current sensor is capable of measuring up to 200 amps, with a 5 µs response time and 1% accuracy. An image of the current sensor can be seen in Figure 11. The system voltage is measured using a voltage divider directly reading the battery pack voltage.

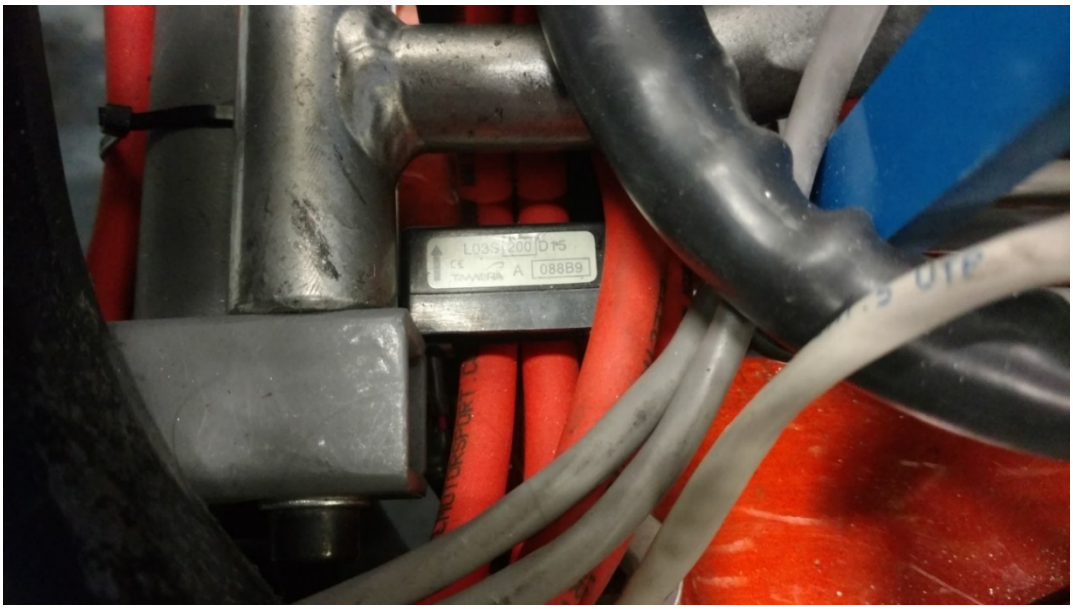

Figure 11: Temura Hall Effect Current Sensor. The sensor in this image is the black rectangle surrounding the two orange power cables. There is one cable for each battery pack.

Control of the kart is done through the implementation of code using National Instruments LabVIEW. The hardware on the kart is a National Instruments cRIO-9076, equipped with a 400 MHz real-time processor and a Spartan-6 LX45 FPGA. The use of FPGA allows for faster computational speed than can be achieved through other means. All communication with the Sevcon Motor Controllers is achieved through a CAN bus using CANOpen protocol.

Chapter IV:Testing Procedure

Section 4.1 Testing apparatus set-up

To provide reasonably repeatable testing circumstances, the INSTAR kart needed to be tested in a laboratory setting. The INSTAR kart was placed on stands such that the wheels were free to spin. To prevent the kart from falling off the stands during testing, causing damage to laboratory equipment and possibly injury to the laboratory personnel, the kart was secured to the ground. Two drop-in style concrete anchors were installed at a depth of 2.5 inches into the concrete floor. These concrete anchors have a pull-out strength of 1,500 lbs., and an internal thread type of ½-13 UNC. Matching lifting eye bolts with shoulders were installed into these anchors, and the kart was secured to them via ratcheting tie down straps. The set-up proved sufficient for all testing performed.

To replicate the energy of a moving kart, 35-inch diameter 1-inch thick steel discs with a mass of 123kg which were placed on the ends of the axels. The rotational energy of the discs can be calculated from Equation 1 and Equation 2.

Equation 1: Kinetic Energy of a Rotating Mass

$$KE_{rotational} = \frac{1}{2} I \omega^2$$

Equation 2: Moment of Inertia of a solid disc

$$I = \frac{1}{2} m m_w r^2$$

In Equation 1 and Equation 2, ω is the rotational velocity of the wheels, *m* is the mass of a wheel, *r* is the radius of a wheel, and *I* is the moment of inertia. The complete set-up of the INSTAR kart can be seen in Figure 12.

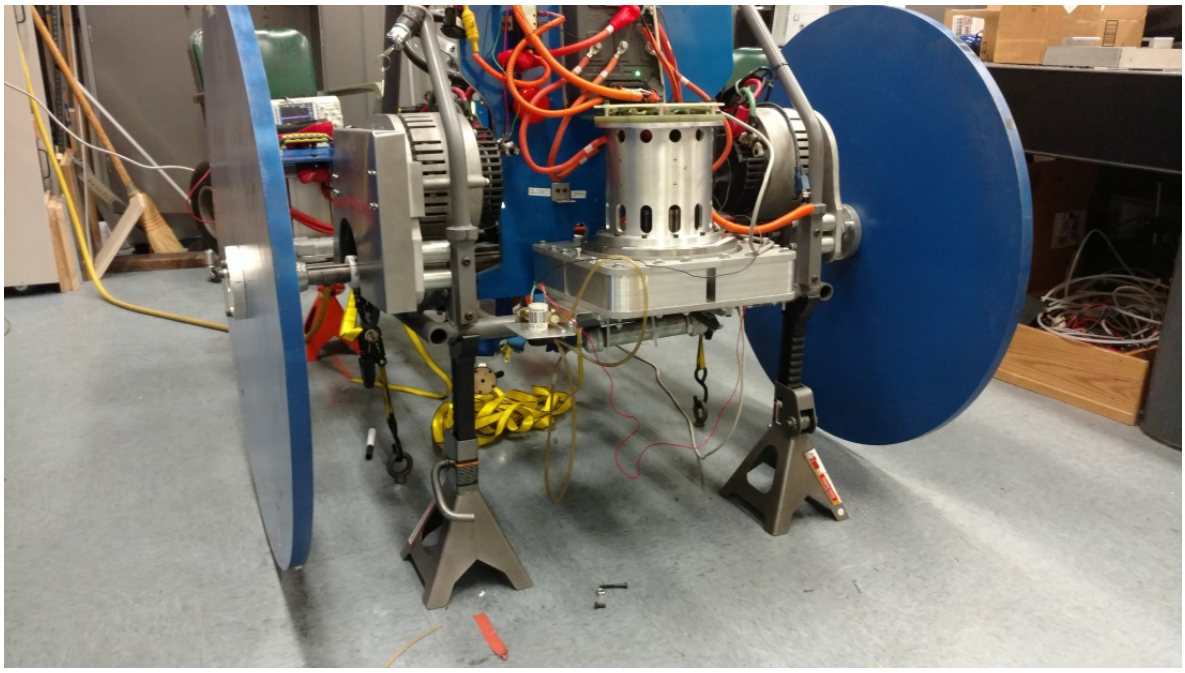

Figure 12: Laboratory set-up of the INSTAR kart

Section 4.2 Driving profile

To conduct testing in the lab, the kart was supplied with a pre-calculated throttle and brake profile. This profile was used for every test to limit the number of variables between different tests. The profile was based on the Urban Dynamometer Driving Schedule (UDDS). The UDDS is used by the United States Government to test light duty vehicles for fuel efficiency in city driving environments [23]. The UDDS can be seen in Figure 13.

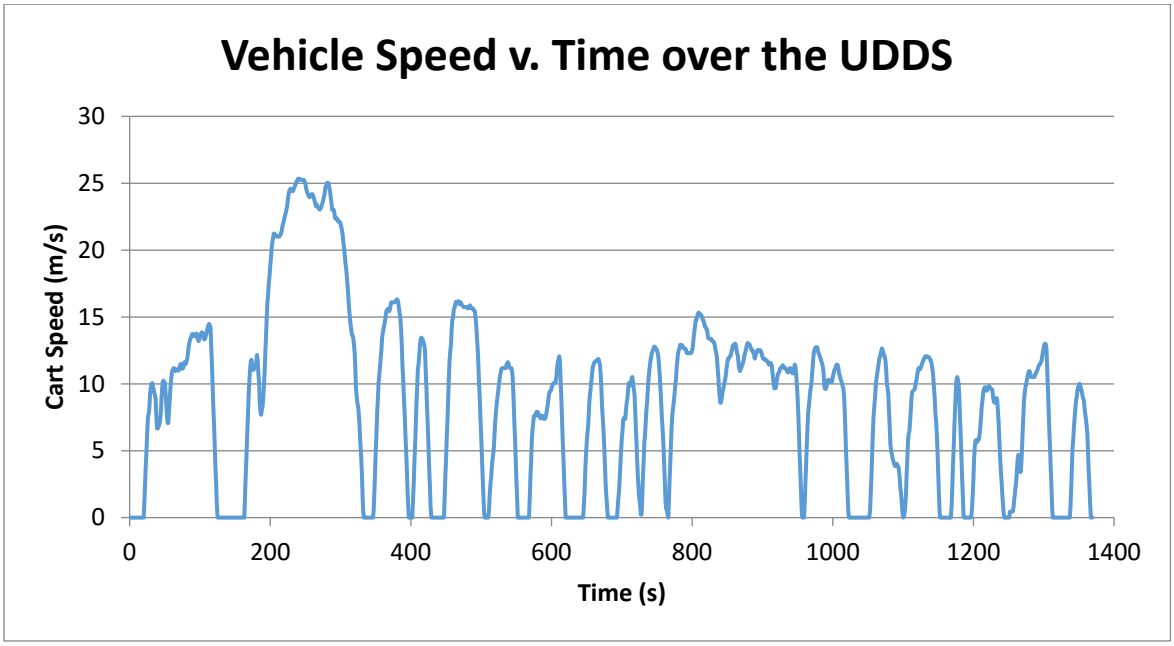

Figure 13: Vehicle speed v. Time over the UDDS

For safety concerns, all laboratory tests were conducted at energy levels 10% of what would be expected for the full 225kg kart. To replicate the energy of the kart over the driving profile, the change in energy was calculated over time, and from this, the necessary torques could be calculated. The change in energy is calculate from Equation 3.

Equation 3: Change in kinetic energy of INSTAR kart during laboratory testing

$$\Delta KE = \frac{1}{2} I\left(\omega_f^2 - \omega_i^2\right) = \frac{1}{2} m_{kart}(v_f^2 - v_i^2)$$

In Equation 3, Δ*KE* can be calculated from the mass of the INSTAR kart (225 kg), and the velocity profile of the UDDS. The moment of inertia (*I*) of the steel discs are known, as well as ω_i as the initial velocity of the kart is 0. Stepping through the time-incremented velocity profile can yield the required torque to match the UDDS. A time increment of 0.25s was used for the experimental tests, but because the UDDS is incremented over seconds, the missing values were calculated using a linear interpolation method. The torque required can then be calculated from Equation 4.

Equation 4: Torque required from traction motors

$$\tau = I\alpha$$

where $\alpha = \frac{\Delta\omega}{\Delta t}$ in Equation 4. Because the traction motors operate on torque commands, this value could be input as a fraction of the maximum torque. For instance, a torque of 5.3 Nm is 1/10 of the maximum torque (53Nm) of the traction motors. The motor controllers operate of a hexadecimal system, where 2560 is the maximum brake or throttle signal that can be communicated. Multiplying the fractional torque values by 2560 provided the brake and throttle signals for the kart.

A plot of the expected combined energy in both wheels, compared with the observed energy in the wheels can be seen in Figure 14. There are some differences in the actual energy state of the wheels from the expected energy state. However, the purpose of this work is not to exactly replicate the UDDS, but to test the efficacy of using a mechanical flywheel to work with a hybrid energy system. So long as the energy state is similar enough to the UDDS, we can say that we are replicating a real-world driving situation in the lab. If it was desired to exactly replicate the UDDS, a closed loop PID controller could be implemented. Because it is only desired to replicate an urban driving situation, it was deemed not necessary to implement a PID control algorithm, and this simplistic approach will suffice.

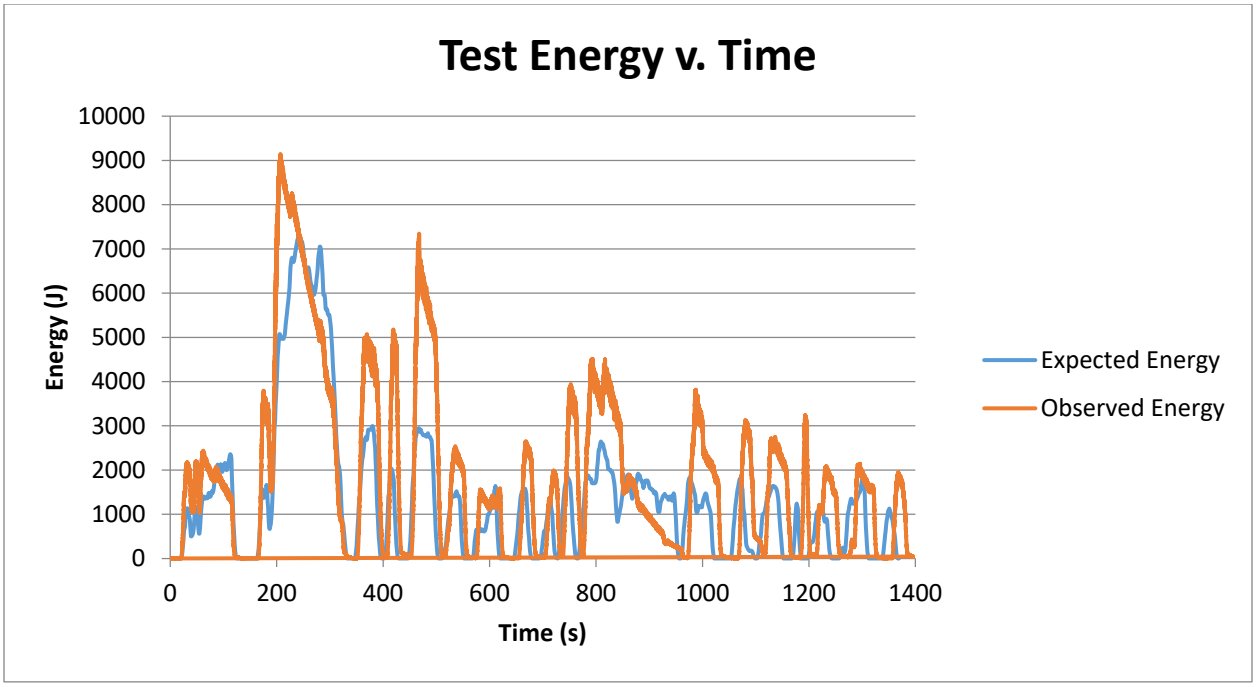

Figure 14: Kart energy v. time during driving profile testing

Section 4.3 Current Flow over the UDDS

The traction motors use electricity to move the kart, or to spin the steel wheel analogs. The amount of current the motors will use can be roughly estimated by the torque constant, which is 0.1830 Nm/Amp (0.0180 Volt/RPM) for the experimental setup. The two motors combined could require as much as 580 amps to accelerate the kart and could likewise regenerate up to 290 amps over the full scale UDDS. This braking current is far in excess of what the batteries can handle without damage, and much of this regenerated energy would have to be dissipated if only the battery and motors were used to transfer power. Because the laboratory tests are conducted at a 1/10 scale of the UDDS, the regenerated currents observed in testing were far below 290 amps, but were still high enough to cause damage to a vehicle battery.

Discussed in section 3.2, the current flow out of the battery was measured using the noninvasive Temura hall effect sensor. To get a baseline, the current was measured without the INSTAR flywheel. The C-rate (current rate to empty the battery within one hour) of a typical hybrid vehicle is between 1 and 10 amps. Thus, for the purposes of this study, it is desired to keep the charging current below 10 amps, even though the C-rate of the testing batteries used is 40 amps. The current flow into and out of the batteries can be seen in Figure 15.

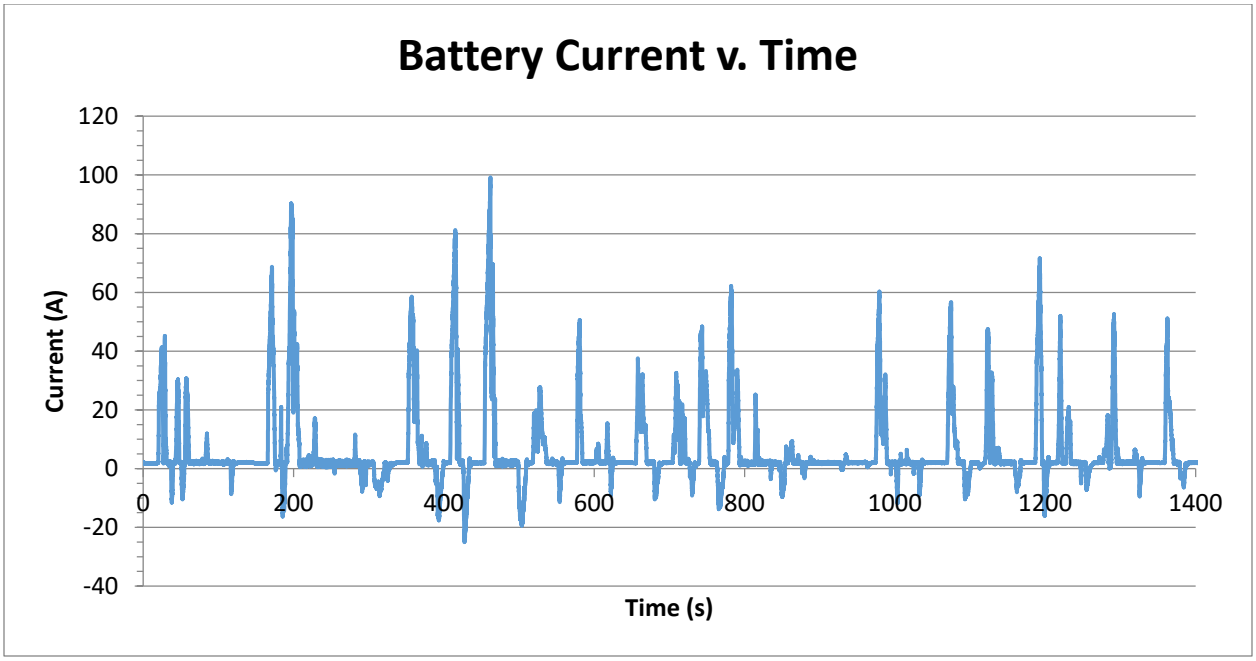

Figure 15: Battery Current v. Time over the test-driving profile.

During testing, the highest discharge current was 99 amps and the peak charge current was 25 amps. These values are too high, and will decrease the lifetime of the batteries significantly. It is important to note that there is a constant draw of about 2 amps needed to power the motor controllers and LabVIEW module. This constant draw is evident by the non-zero resting current observed in Figure 15. For improved battery lifetime, battery charging rates should not exceed the C-rate of the battery.

Chapter V: Flywheel Control for Battery Charging Current Optimization

The purpose of this project is to use the electromechanical flywheel to absorb potentially dangerous charging currents generated from the traction motors. The flywheel is controlled by a Sevcon Gen 4 motor controller, which reacts to throttle signals fed to the controller. These throttle signals are generated by the supervisory controller, and a control algorithm was created to generate flywheel throttle signals from signals read from various sensors on the kart, as well as throttle and brake signals fed to the traction motors. If a positive throttle value is fed to the flywheel, current travels through the Sevcon controller, and into the flywheel motor, where it is converted from electrical energy into the mechanical energy of the spinning flywheel. The algorithm is responsible for determining the correct amount of throttle to send to the Sevcon controller. Too little throttle will result in the flywheel not absorbing enough current, leading to an unacceptable charging current at the batteries. Too much throttle will cause the flywheel to pull electricity out of the battery pack, which is undesirable because of the parasitic losses associated with the flywheel. A schematic of the power flow can be seen in Figure 16.

Section 5.1 Open Loop Control Algorithm

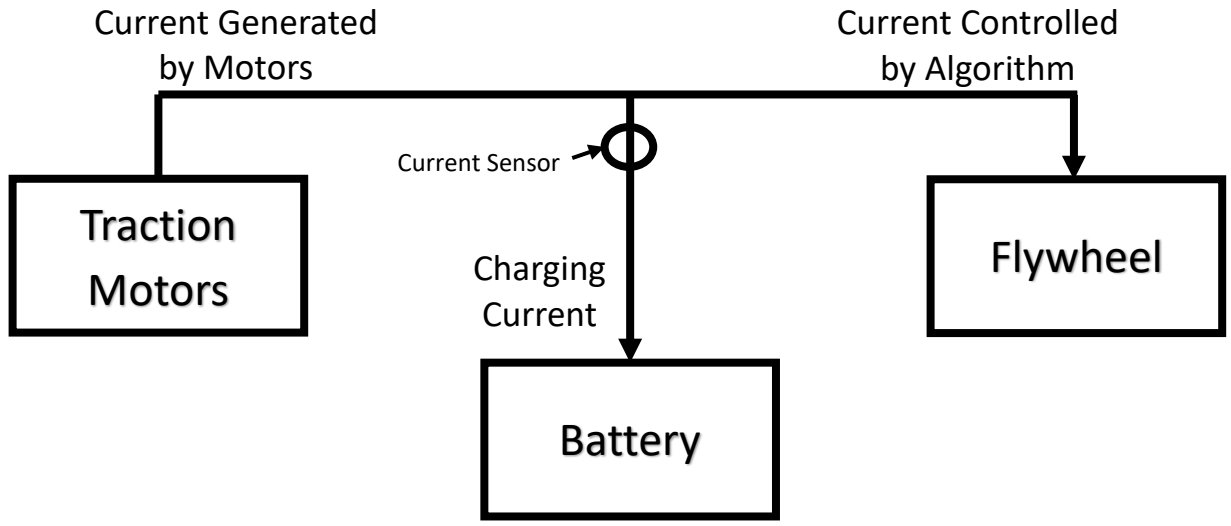

Figure 16: Schematic of power flow in INSTAR system

The purpose of this work is to demonstrate the possibilities that a flywheel can give to a hybrid vehicle, not to create an optimized controller algorithm. In previous INSTAR work, it was found that an open loop controller was capable of limiting the current to the batteries. It was chosen to implement the same open loop controller for these experiments. The open loop algorithm is seen Equation 5 below, and the corresponding coefficient values can be seen in Table 1. A derivation of the open loop control algorithm completed by previous INSTAR researchers can be seen in Appendix A.

Equation 5: Open Loop Algorithm

$$Flywheel\ Throttle\ Signal = F\left[\frac{A(T_B * \omega_V) - BT_B + C\omega_V}{(D\omega_f + E)}\right]$$

Table 1: Open Loop Coefficients

A	0.4
B	0.4
C	-0.12
D	0.4
E	2.7
F	2.1

The algorithm consists of 3 main parts. The numerator of the algorithm is designed to predict the current the drive wheels will generate during the braking cycle. In the numerator, T_B is the braking torque sent to the traction motors and ω_v is the speed in rpm of the traction wheels. Because the testing platform is not a perfect system, the coefficients in the numerator serve to tune the algorithm for better prediction. The denominator of the algorithm serves to predict the amount of current being absorbed by the flywheel. In the denominator, ω_f is the rotational speed of the flywheel in rpm, and the coefficients D and E serve to tune the controller for better prediction. The scaling factor *F* is used to increase or decrease the magnitude of throttle signal sent to the flywheel. From previous INSTAR work, the algorithm was tuned to provide the best results when the flywheel was energized from a stopped position, and under controlled, simple deceleration events. It was found during testing under the driving UDDS, that these coefficients were not tuned correctly to account for the much more random driving cycle, and the coefficients had to be changed to the values seen in Table 1. Once tuned the open loop controller was reasonably successful at controlling the battery current. The current at the battery can be seen in Figure 17.

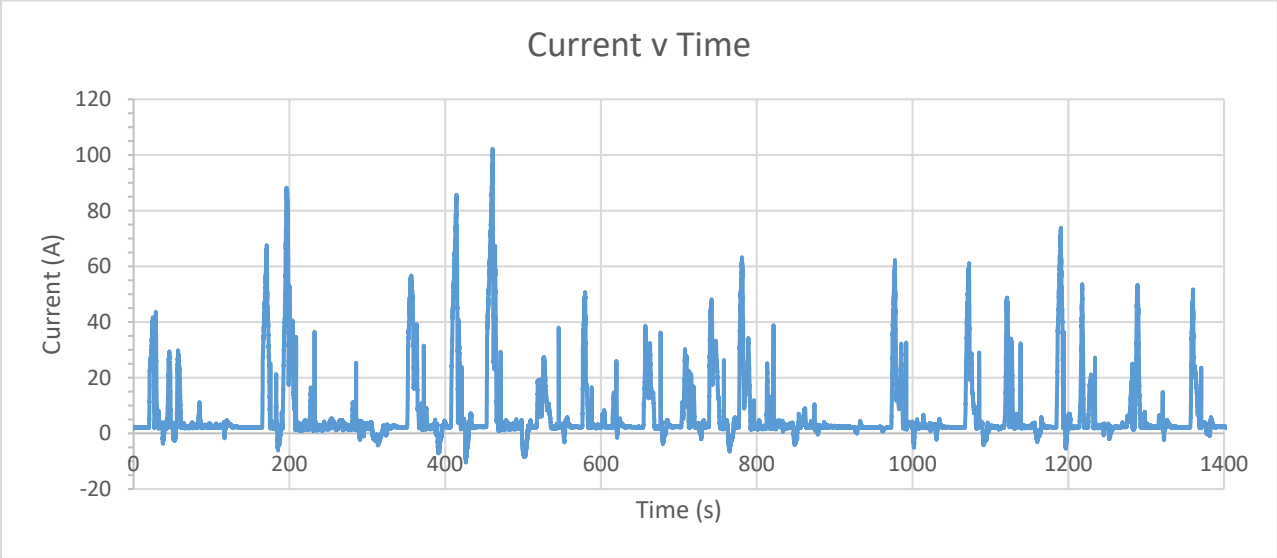

Figure 17: Battery Current Resulting from Open Loop Control Only

The open loop controller was successful in limiting peak battery current, and there was only 1 charging peak in excess of 10 amps, where in the baseline tests there were 11 peaks over 10 amps. The maximum charging current was also reduced from 25 to 13 amps. But upon further inspection, it is obvious that the open loop control alone could be improved upon. Figure 18 shows an isolated braking event. It can clearly be seen that the open loop control underestimates the amount of throttle needed to absorb the charging current, then overshoots the current at the end of the braking cycle, pulling current out of the battery. Further tuning of the control algorithm was unable to remedy this problem, and in an effort to solve the issue, a hybrid control system was attempted.

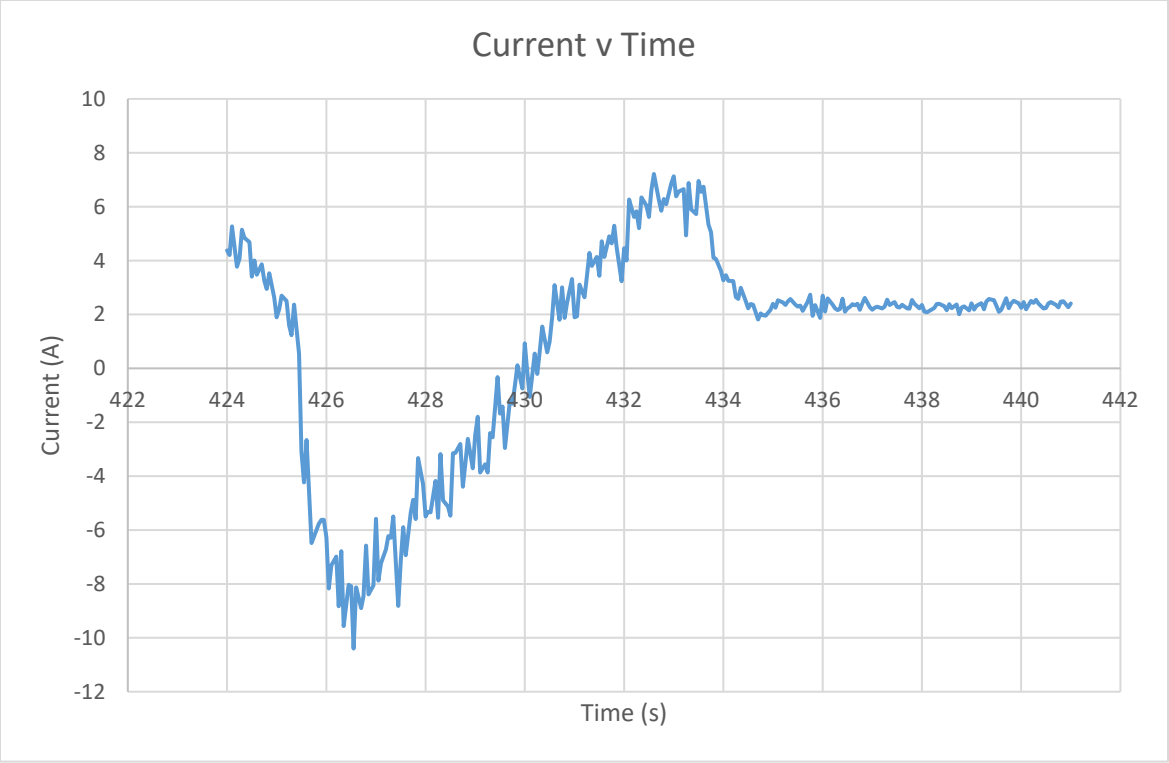

Figure 18: Figure Showing Close up of Braking Cycle Using Open Loop Control Only

Section 5.2 Hybrid Control Algorithm

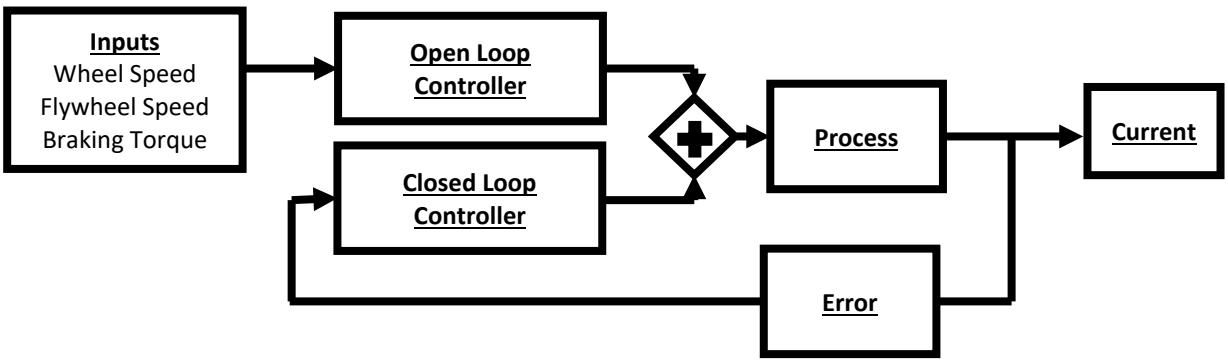

Figure 19: Schematic of hybrid controller

In a hybrid controller, an open loop algorithm is combined with a feedback control to better respond to the needs of the system. This method gives the benefit of a having an initial value present from the start of the process, without the need to wait one cycle for an error to be generated. The error can also be smaller than in a strictly closed loop control system if the underlying open loop controller is tuned correctly. But like in a true closed loop control system, the controller will respond to the error in the system, and attempt to trend the process to the desired set point.

For this study, a PD controller was placed in parallel with the open loop controller. The output from the PD controller was added to the output of the open loop controller in an attempt to correct the errors of the open loop controller, and to drive the battery current towards the desired set point. A schematic of the controller can be seen in Figure 19. The different variables of the closed loop portion of the control can be seen in Table 2.

Table 2: Hybrid Controller Variables

Manipulated Variable	Flywheel Throttle Signal (0-2559)	Digital CAN Signal to Flywheel Controller
Process Variable	Battery Current, I (Amps)	Hall Effect Current Sensor
Setpoint	Desired Charging Current	Variable, but set to 0 for this Study
Error	Setpoint-I (Amps)	This Error is Only Present when the brake is Applied

Using the hybrid control algorithm, larger open loop values could be used for a faster response of the flywheel. This was accomplished by increasing the F coefficient in the open loop algorithm. The PID controller was tuned using an iterative process where values of P, I, and D were slowly increased from a low initial value until the controller was acting as desired. The embodiment of this hybrid controller resulted in somewhat better results than the closed loop controller attempted in previous INSTAR research, and also allowed for faster response of the flywheel than the pure open loop controller. The tuned values from the controller can be seen in Table 3 below.

Table 3: Tuned Coefficients of Controller

Coefficient	Value
A	0.4
B	0.4
C	-0.12
D	0.4
E	2.7
F	2.7
Proportional Gain	5
Derivative Gain	7
Closed Loop Setpoint	-0.5 Amps

The battery current over the UDDS with the flywheel activated can be seen in Figure 20 below. With the hybrid control algorithm, charging peaks were significantly reduced over the baseline tests. The maximum charging peak was reduced from 13 amps with the open loop control only to 7.9 amps with the hybrid control algorithm. The reduction of charging current below the desired maximum of 10 amps is a positive result, however, the hybrid control algorithm produced some very undesirable side effects.

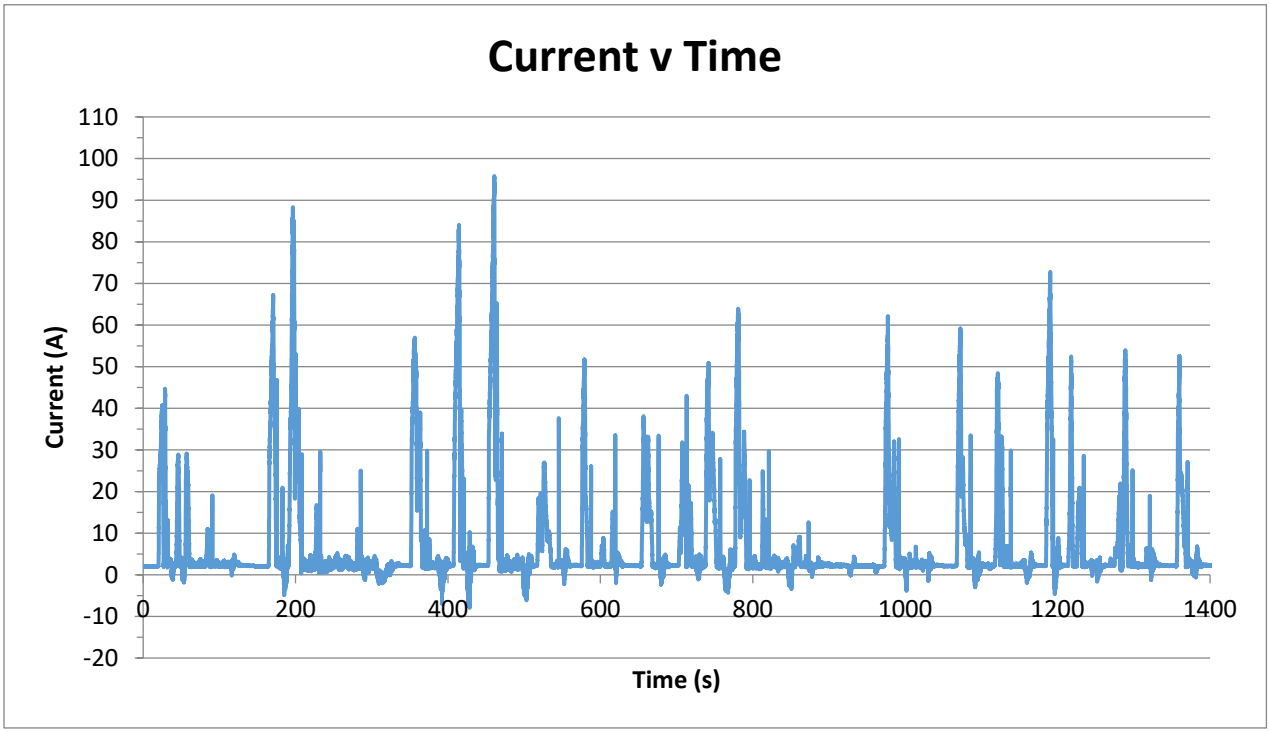

Figure 20: Battery Current from Hybrid Control

Though the charging amps were limited, the hybrid control did induce severe oscillations within the braking cycles. An example can be seen in Figure 21, which shows the same braking even as Figure 18. These oscillations were not present during braking events small enough where the PD control was not active, but as the amperage increased beyond the setpoint they emerged. Many attempts were made to find tuning coefficients to eliminate the oscillations while still providing benefit to the battery current reduction, however a set of coefficients could not be found. For this reason, the hybrid control system was abandoned, and only the open loop control was utilized.

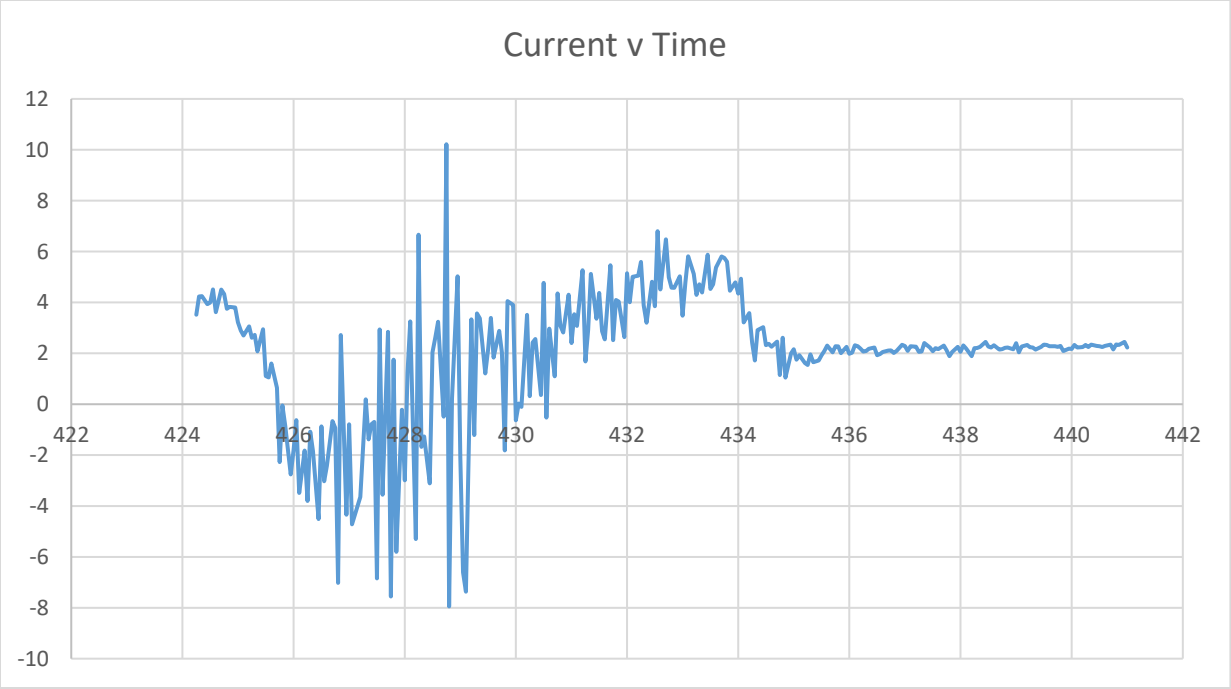

Figure 21: Oscillations induced from Closed Loop Controller

There are many possible reasons for the problems seen with the hybrid control, one of which is the noise seen in the system from the current sensor, as seen in Figure 22. Another may be the interference from the internal PID controller within the Sevcon motor controller. Through more complex control algorithms, and improved filtering of the kart sensors, improved control may be possible. Future work on this is left up to members of the INSTAR lab. If a commercially available INSTAR system is to be developed, the algorithms will likely be incorporated into the motor controller, eliminating the possible interference from the underlying Sevcon internal controls.

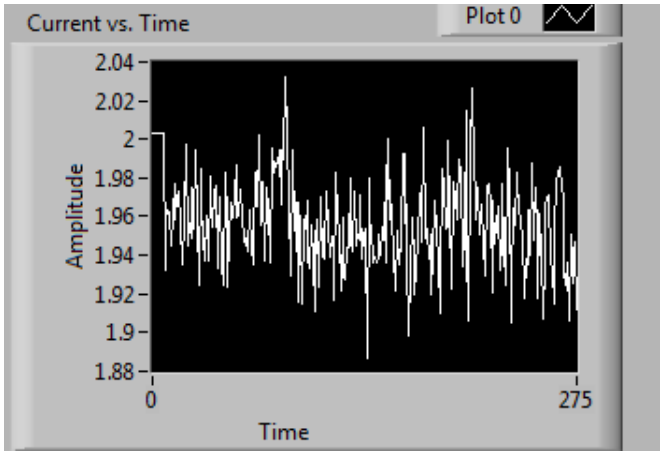

Figure 22: Noise in Current Sensor

Chapter VI Power Removal from flywheel

In the previous trials in this study, energy was only placed into the flywheel, it was not taken out of it. Once the energy is in the flywheel, it will slowly dissipate to 0 if not removed. This is due to the parasitic losses associated with the ball bearings and windage losses of the flywheel rotor. Therefore, removing the energy from the flywheel as fast as possible is desired to reduce the amount of energy dissipated.

Section 6.1 Flywheel Energy Dissipation

Previous INSTAR studies have calculated the energy dissipated during flywheel operation. The studies determined that energy losses could be minimized through the use of open bearings without any sealing elements against the flywheel shaft or bearings. A spin down test from previous work between several types of bearings can be seen in Figure 23. The open bearing design provided the least amount of parasitic losses, however is not without its drawbacks. Using light oil provides less lubrication than bearing grease and can lead to shorter bearing life.

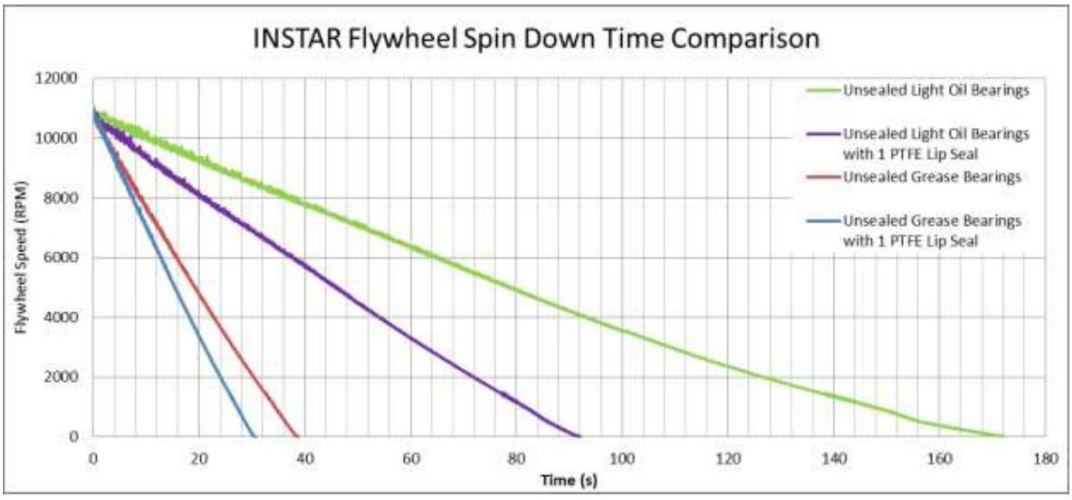

Figure 23: Spin down test of flywheel. Replicated from Talancon (2015)

To provide a constant lubrication system to the bearings, a recirculating oil system was installed in the flywheel. The oiling system injects oil above the top bearing of the flywheel, where it drips down through the bearing, around the flywheel rotor, and down onto the lower bearing. Gravity returns the oil to a reservoir below the flywheel, and a pump starts the process over again. A schematic of the oiling system can be seen in Figure 24.

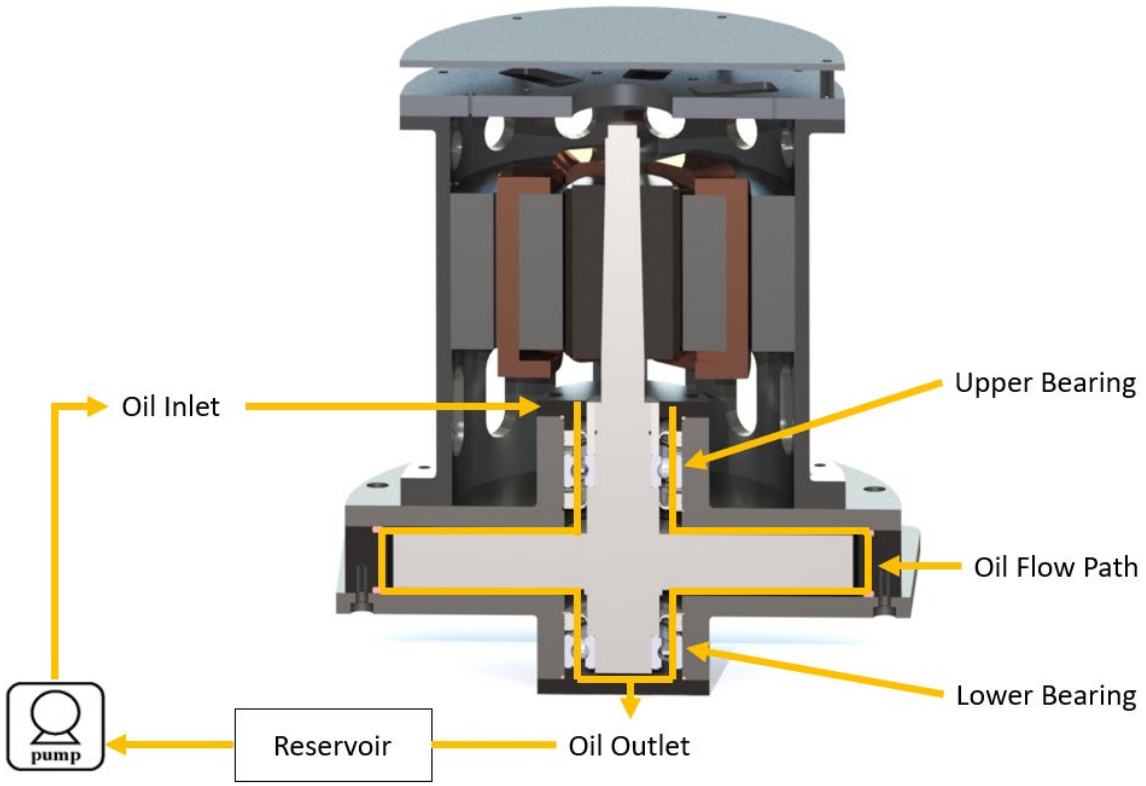

Figure 24: Oiling System

When operating the oiling system, it was found that over oiling the system would produce undesirable results. Too much oil in the bearings would increase the friction losses of the bearings, as the oil was churned in the bearings. Additionally, because gravity was used to move the oil through the system, supplying oil at a faster rate than it could be removed would fill the flywheel casing with oil. When this happened the frictional losses between the oil and flywheel would become excessive, and slow the flywheel at an unacceptable rate. The oiling method providing the best results was to turn the pump on for 1 second every minute, providing only a few cubic centimeters of oil to the bearings. Using this strategy, a lubricating film of oil was maintained in the bearings, while preventing the problems associated with over oiling.

Flywheel losses with this system are kept to the minimum allowable using conventional ball bearings. Conventional ball bearings are used because the desired result of this work is to create a low-cost solution to the current spike problem which can be implemented in consumer commuter type vehicles. Magnetic levitating bearings could provide fewer parasitic losses, but are more expensive than conventional rolling element type bearings, and any increases in performance they provide would likely not outweigh their cost.

Because flywheel losses still exist, it is desired to remove the energy from the flywheel as soon as possible. If the flywheel is just left to spin on its own, parasitic losses will rob energy from the flywheel, and it will spin down to 0 gradually over time. A graph showing the flywheel speed over the UDDS, where no energy was recovered from the flywheel can be seen in Figure 25. One can see that the flywheel speed will decrease towards zero when energy is not being put into the flywheel. It is desired to remove all of the energy as fast as possible after a braking event. However, the current returning to the battery from the flywheel must not exceed the C-rate of the battery. For the purpose of this study, the C-rate is assumed to be 10 amps.

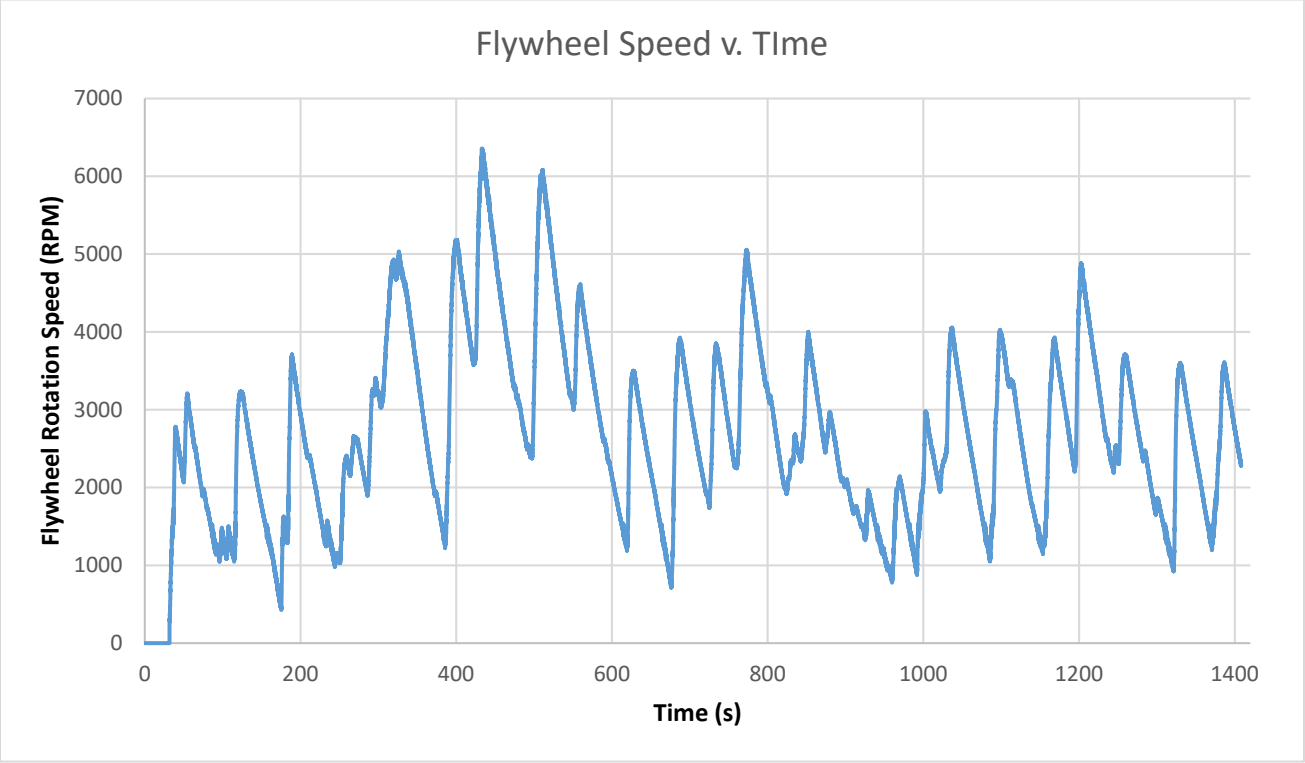

Figure 25: Flywheel Speed v. Time over the UDDS when no energy is removed from flywheel

Section 6.2 Flywheel Energy Removal Strategy

To remove energy from the flywheel, it was determined that providing the flywheel braking signals manually, rather than creating another control algorithm would be sufficient for this study. Because the kart travels over the same driving profile for every trial, and because the flywheel currents, speeds, and battery currents were known, flywheel brake signals could be inferred from previous tests. Flywheel brake signals were sent using the same strategy as the throttle and brake signals for the traction motors.

For this study, a single brake value was sent to the controller whenever the flywheel was in an energized state, but was no longer receiving current from the traction motors. For this strategy to work, a braking value needed to be found which would remove energy from the flywheel at a high enough rate but would not send too much current out of the flywheel to

damage the batteries. This in practice required both tuning of the maximum torque values in the Sevcon internal programming and the selection of an appropriate braking signal from the supervisory LabVIEW control. A table of the parameters set within the Sevcon controller can be seen in Table 4.

Table 4: Table of braking parameters

Parameter	Value
Sevcon Maximum Braking Torque	9.983 N*m
Sevcon Maximum Change of Direction Torque	9.983 N*m
Sevcon Braking Torque Rate	335 N*m/s
Sevcon Change of Direction Torque Rate	67 N*m/s
Sevcon Driving Profile Braking Torque Percentage	100%
Sevcon Driving Profile Direction Change Torque Percentage	80%
Sevcon Driving Profile Ramp up rate during Direction Change	200%/s
Sevcon Driving Profile Ramp up rate during Braking	300%/s
Supervisory Control Torque Value (1-10)	1.33594

An example of a round trip current flow in and out of the flywheel during the UDDS can be seen in Figure 26. This figure shows that the flywheel absorbs current during the braking event, as indicated by the positive current, then after the braking event is over, and there is no more current to absorb, a brake is applied to the flywheel, and current is sent from the flywheel to the batteries and/or traction motors, as indicated by the negative currents.

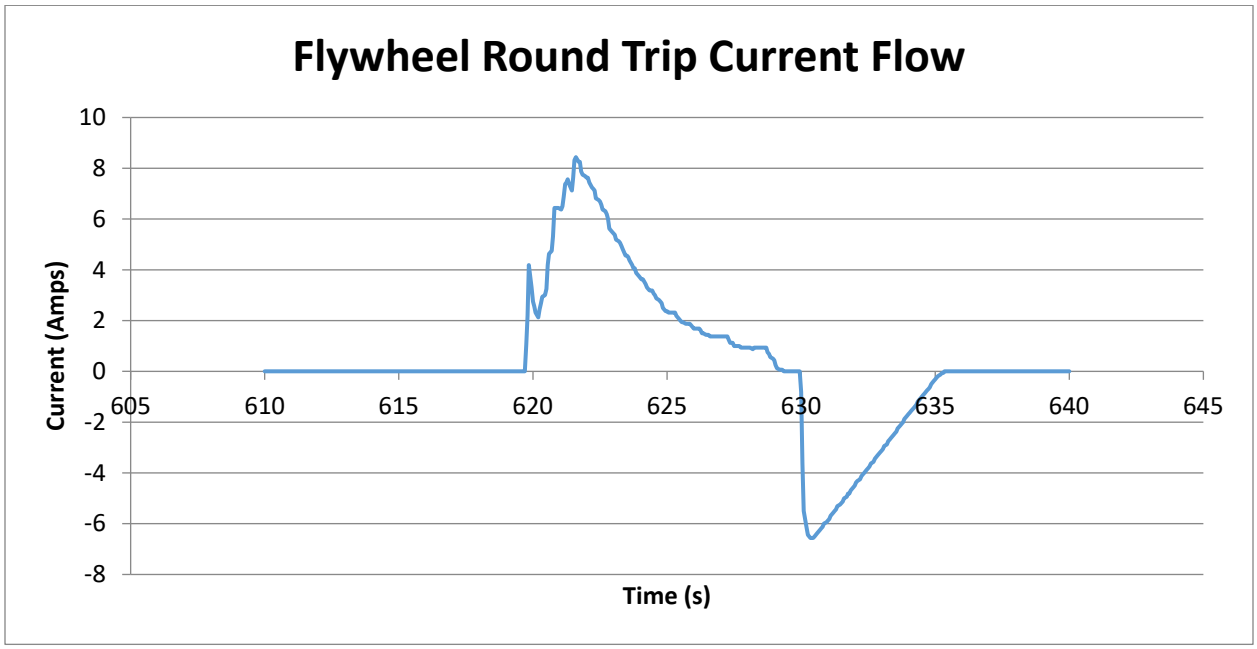

Figure 26: Round trip current flow during braking event in UDDS

Figure 26 demonstrates an inefficiency of the braking algorithms as described, the current removed from the flywheel starts at a high value, and slowly decays to 0 as the flywheel rotational velocity decreases. This is due to a single constant braking signal being sent to the flywheel for the entirety of the braking event. The round-trip efficiency in the braking event shown in Figure 26 is 58.9%, but round-trip efficiencies varied for every braking event based on braking and flywheel conditions and will be discussed in more detail in Section 6.04. This inefficiency could possibly be reduced by increasing the flywheel braking signal through the energy removal phase, to keep the current level more consistent, and to remove the energy faster. This would require either the implementation of a PID control, or open loop algorithm to the energy removal portion of the control. Because this is an exploratory study, further refinement of the control is left to future members of the INSTAR lab.

Section 6.03 Modifications to the Open Loop Algorithm for Energy Removal

The open loop algorithm for flywheel throttle is reproduced here for convenience.

$$Flywheel\ Throttle\ Signal = F\left[\frac{A(T_B * \omega_V) - BT_B + C\omega_V}{\left(D\omega_f + E\right)}\right]$$

As shown earlier, this algorithm proved sufficient in limiting battery current through sending currents over the desired battery threshold to the flywheel. But when energy was removed from the flywheel, the algorithm began to malfunction. Figure 27 shows the battery current when energy removal from the flywheel was activated, while Figure 28 shows battery current when energy was only stored in the flywheel and was not removed. As one can see, the chart in Figure 27 shows many more positive current spikes than the chart in Figure 28. These additional positive current spikes are the result of the algorithm denominator becoming very small when the flywheel has a zero initial velocity, causing the algorithm to output a very high flywheel throttle signal. Once the flywheel gained some rotational velocity, these flywheel signals returned to a more accurate level. An example of this effect can be seen in Table 5 below.

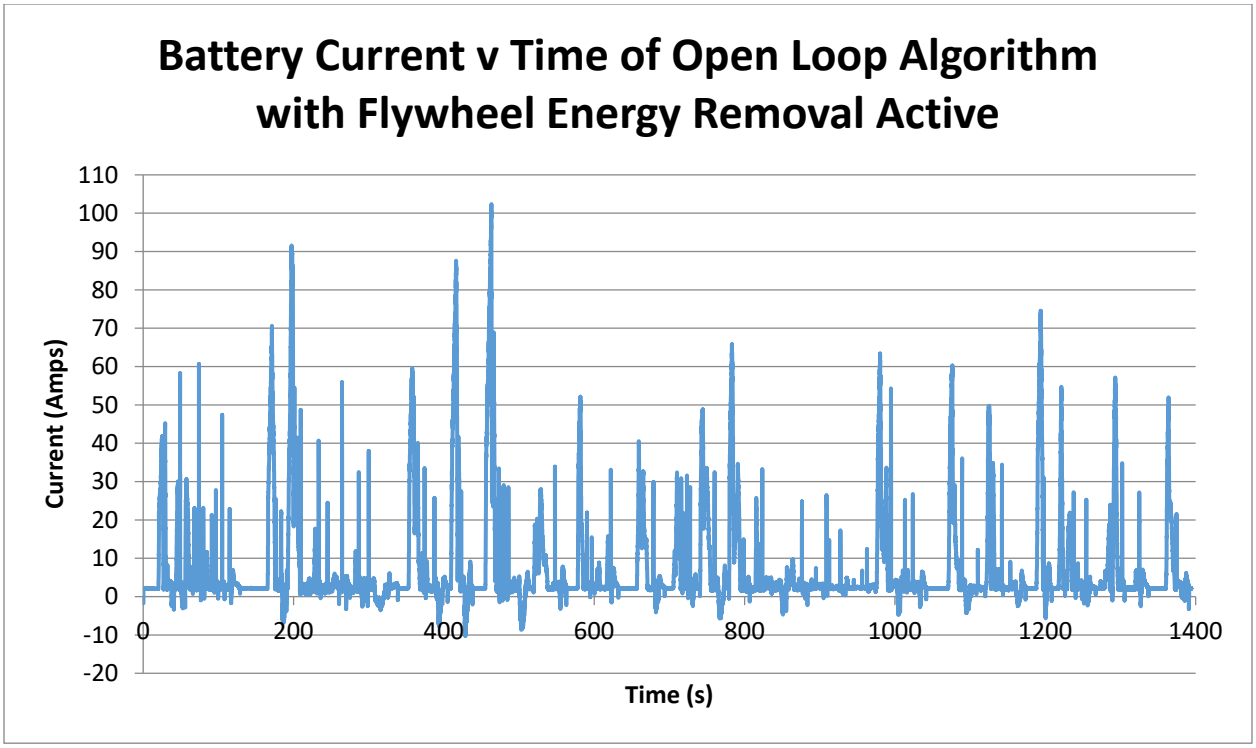

Figure 27: Current v. Time of open loop control with flywheel energy removal activated

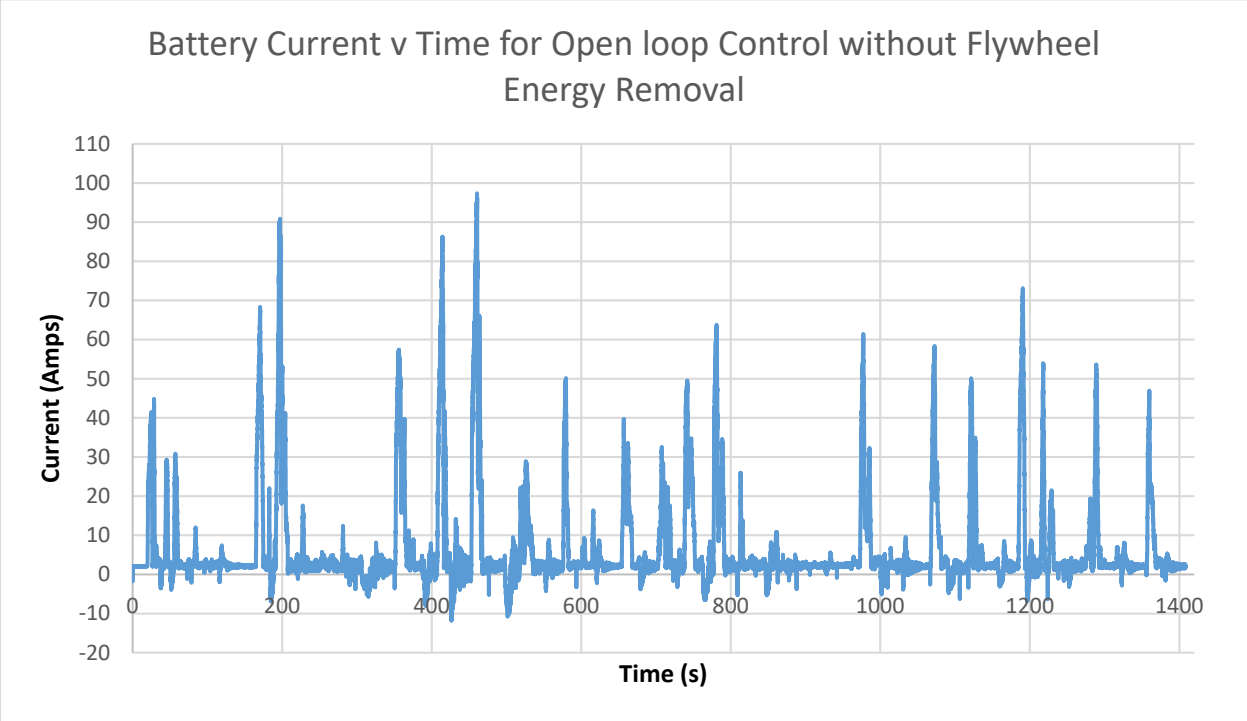

Figure 28: Battery Current v. Time for Open Loop control without Flywheel Energy Removal

Table 5: Example of Flywheel throttle signals during open loop control with flywheel energy removal activated. Artificially high initial values can be seen until the flywheel gained some rotational velocity.

TIME	Flywheel Throttle Signal (0-2559)	Flywheel Speed (rpm)
104.95	485	0
105	501	0
105.05	53	41
105.1	6	414
105.2	9	520
105.251	9	506
105.3	10	491
105.35	9	499
105.45	20	499
105.5	21	489
105.55	21	481
105.6	20	508
105.7	30	493
105.751	28	519
105.8	29	532

These large spikes in flywheel throttle signals result in the flywheel drawing power out of the battery packs, which is undesirable. To combat the break down in algorithm effectiveness a simple threshold filtering of the flywheel throttle signals was implements. For the purposes of this study, it was found that placing an upper limit of 200 on the flywheel throttle signals was sufficient to keep the flywheel from drawing power out of the batteries at the beginning of the braking cycle.

Section 6.04 Energy Removal Results

With the flywheel energy removal strategy in place, as well as the modifications to the open loop algorithm the UDDS throttle signals were applied to the testing apparatus. During the tests, the flywheel successfully limited battery charging current as seen in Figure 27. During the test, all but three of the battery charging events were below the 10-amp threshold, with three events being 12.5 amps, 11.4 amps, and 10.5 amps. These three events were from excessive flywheel discharging currents, and could be eliminated through more sophisticated control algorithms in the flywheel braking strategy. Because the single value braking strategy worked for the rest of the braking events, and because these events were only slightly above the target threshold, no additional work on the braking strategy was performed here, however it should be done by future members on the INSTAR Lab.

Flywheel Speed

One of the goals when removing energy from the flywheel is to not let the flywheel spin in a neutral state because of the parasitic losses inherent in its design, as discussed before. The

flywheel braking strategy implemented in this study brought the flywheel back to zero velocity after every flywheel charging event, thus limiting the amount of time the flywheel spent in a neutral energized state. The effects of this strategy over the UDDS can be seen in Figure 29.

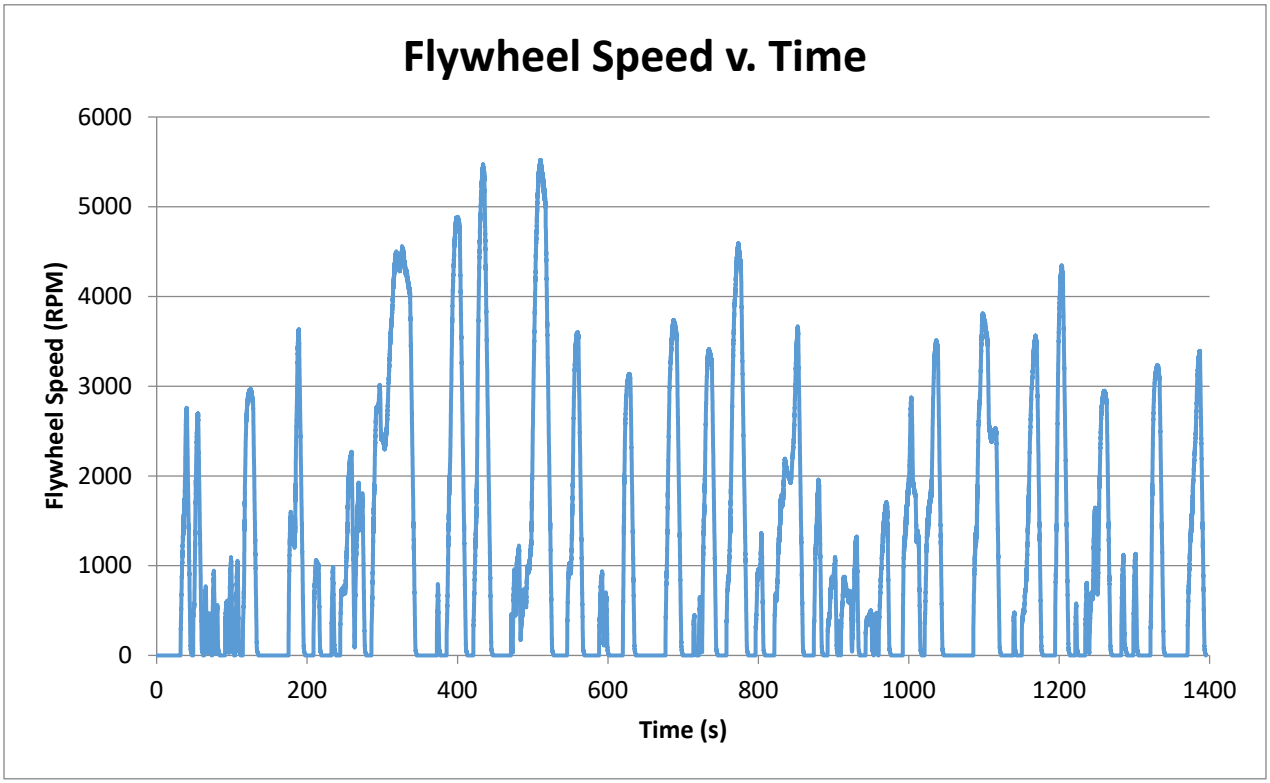

Figure 29: Flywheel velocity over the UDDS with braking strategy implemented.

Power Flow

It was desired to see the power flow in and out of the flywheel. The power flow could have been calculated from the change in rotational energy of the spinning flywheel, however this would not capture the efficiencies of the motor controller. The better way to calculate the power flow is from the voltages and currents read from the flywheel motor controller during the test, and making use of Equation 6.

Equation 6: Flywheel Electrical Power

$$P = I * V$$

The Sevcon controller is capable of reading current going to and from the motor, as well as the voltage the controller is operating at, and conveying this information via the CAN bus to the supervisory control, where it was recorded via the LabVIEW program. An example of the power flow from one round trip flywheel energization and de-energization event can be seen in Figure 30.

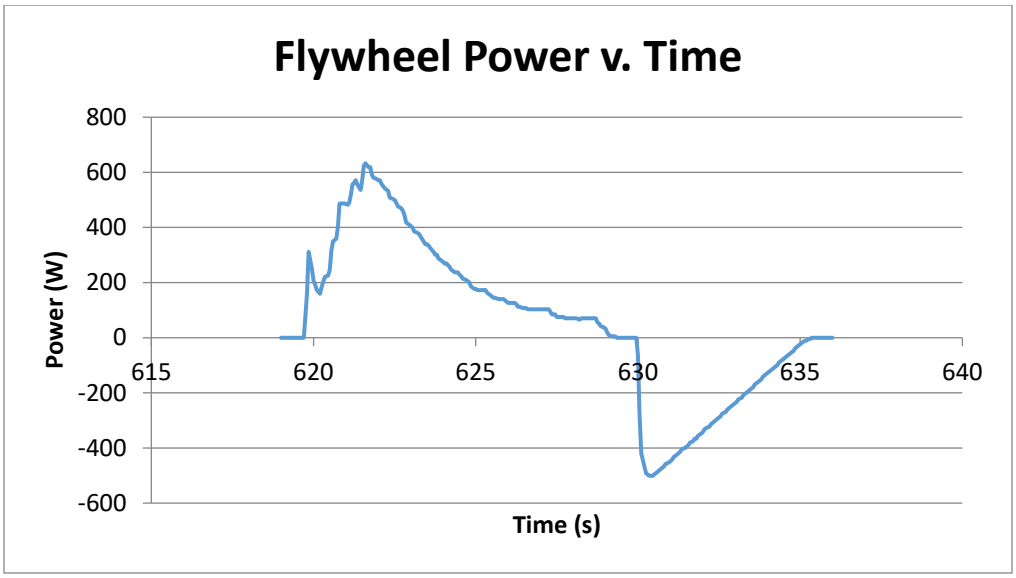

Figure 30: Flywheel Power Flow during one round trip flywheel energization event.

Flywheel Round Trip Efficiency

It is desired to determine the round-trip efficiency of the INSTAR system. The efficiency of the system can be calculated from Equation 7.

Equation 7: Flywheel Efficiency

$$\eta_{INSTAR} = \frac{energy_{out}}{energy_{in}}$$

From the Sevcon controller, the flywheel currents and voltages can be read and recorded throughout the tests. From the current and voltage, the change in energy over a period of time can be calculated from Equation 8, where *P* was determined earlier:

Equation 8: Change In energy of flywheel over a time period t1 to t2

$$\Delta Energy = \int_{t_1}^{t_2} P\, dt \quad \text{or} \quad \Delta Energy = \sum P * \Delta t$$

In previous INSTAR studies, flywheel efficiency was measured under controlled tests. These tests were designed to test the optimal efficiency of the flywheel, where energy was placed into the flywheel, continuously ramping up flywheel speed, and then the energy was removed, again continuously reducing flywheel speed. This is the most ideal flywheel scenario, and a plot showing flywheel speed, and currents over the test can be seen in Figure 31. The flywheel efficiency in these tests was reported to be average 69.05%, and ranged from 68.3% to 70.7%.

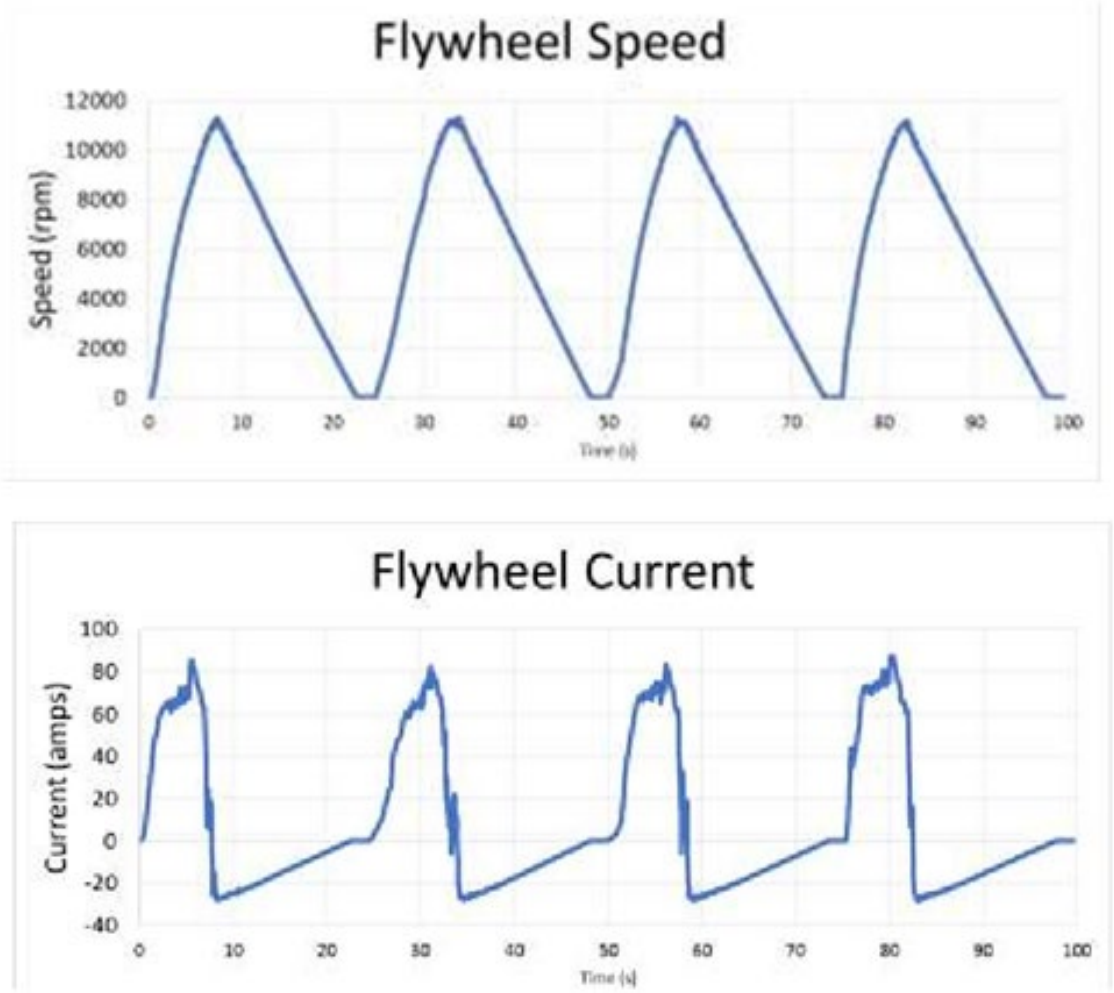

Figure 31: Flywheel Speed and Currents from previous round trip efficiency tests conducted by the INSTAR team. Plots taken from the doctoral dissertation of Daniel Talancon [22]

In practice over the UDDS, the efficiency varied depending on the braking conditions. Two factors could be responsible for the variance and decrease from the optimal flywheel efficiency. One is where the energy is held in the flywheel for longer than necessary, which would obviously incur parasitic losses. The other factor is when the open loop controller provides a throttle to the flywheel, which is insufficient to overcome the losses in the flywheel. In these circumstances the flywheel may decrease in velocity, or simply maintain its velocity, even though power is being sent to the flywheel. An example of this situation can be seen in Figure 32. The efficiency for this flywheel cycle is only 52.1%, substantially lower than the ideal 69%. Flywheel cycles in the full UDDS test ranged from about 50% to about 65% efficiency. It is important to remember that under a more optimized control, only excess energy would be sent to the flywheel, and this energy would otherwise be wasted in a non-INSTAR system.

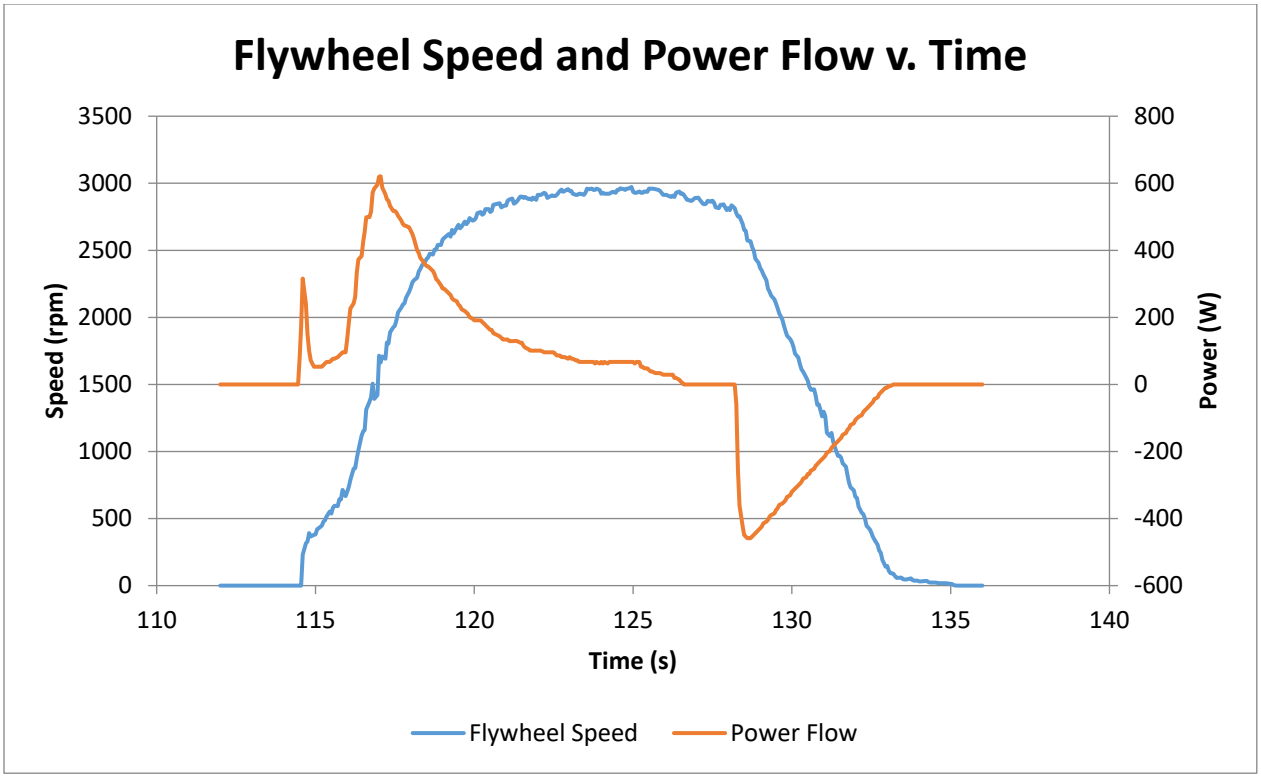

Figure 32: Flywheel speed and power flow for a single kart braking event

The overall efficiency of the flywheel for the entire UDDS test was 55.16%. This number is significantly lower than the maximum efficiency of the INSTAR system, but can likely be improved through a more optimized control algorithm for both flywheel throttle and braking signals.

Total Energy Usage

The total energy usage over the UDDS for various charging situations can be seen in Table 6. It is important to remember that the UDDS cycle as tested is one tenth of the true UDDS for a vehicle the size of the testing kart, and approximately 1/60 the energy levels of a full-size hybrid vehicle. It is also important to note that the data was collected from different tests, for example, the data for the INSTAR system was gathered from a test different than the baseline test. Because of this the raw energy totals should not be compared, but instead the normalized energy usage, and the energy efficiency. The energy efficiency here was calculated from the net energy used by the traction motor controllers, and the energy drop in the batteries. This efficiency does not consider the net result of the traction wheel speed.

Table 6: Energy usage over the UDDS for various charging situations

Situation	Total Energy Use (kJ)	Total Traction Motor Energy (kJ)	Normalize energy usage (Battery energy/Motor energy)	Energy efficiency (Motor energy/battery energy
Full Regeneration with no restrictions	604.2	369.8	1.634	.6121
Maximum 10-amp regeneration	611.1	369.8	1.653	.61052
Maximum 5-amp regeneration	628.7	369.8	1.707	.5892
No regeneration	667.7	396.8	1.811	.5539
INSTAR test	624.3	367.8	1.707	.5891

The maximum efficiency of the testing was found to be 61.21%, which represents a scenario where there are no restrictions on the regenerative braking. The efficiency would drop to a maximum efficiency of 60.52% if up to 10 amps could be absorbed by the battery packs, and 58.92% if only 5 amps could be absorbed by the battery packs. These two current values represent the c-rates of typical commercially available hybrid vehicles. If no regeneration was possible, then the efficiency would be 55.39%. The kart with the INSTAR system has an efficiency of 58.91%, which is less than the 10 amp case, but slightly larger than the 5 amp case. There are several factors limiting the realization of the INSTAR potential in the lab. Firstly, the open loop controller operates whenever the kart begins braking, and sends throttle signals to the flywheel for the entirety of the test. It should be possible to gain efficiency by optimizing the control such that the flywheel receives no throttle when the amperage leaving the controller is less than 10 amps.

Secondly, it is only possible for safety reasons to use a 1/10 energy level UDDS for kart testing. This limits the regeneration currents seen from the traction motors. Much more potential for improvement would exist if the kart was operated at the full energy levels of the UDDS for the size of the vehicle. Full scale road tests will be discussed in Chapter 9.

Thirdly, the control algorithms for the INSATR in both energization and de-energization are not optimal, and many improvements can be made. It is also worth noting that the energy calculated for the threshold regeneration strategies is simply a sum of all energy levels not exceeding the set current limit, which may or may not reflect a real-life braking scenario for commercial hybrid vehicle.

Modifications to the flywheel throttle control to gain more efficiency

Though the pure open loop control algorithm was successful in reducing battery currents, some efforts were made to increase the efficiency by altering the control algorithm. A strategy which resulted in increased efficiency was to only charge the flywheel when the motor discharge

current was over 9 amps, and to regenerate from the flywheel when the motor discharge current was below 2 amps. The strategy was implemented by placing a minimum threshold on the start of the flywheel throttle algorithm, when the threshold was reached, the open loop controller would provide the flywheel with throttle signals. When the discharge current sank below the minimum threshold, the open loop controller would turn off and the flywheel would hold the energy until a brake signal was sent to the flywheel motor controller. Brake signals were again sent manually to the controller, using the same strategy as the throttle and brake signals for the traction motors.

This strategy is sufficient for exploring the possibilities the INSTAR system can provide; however, it is not an optimized control algorithm. When the traction motor regeneration currents are between 9 and 2 amps, the energy stored in the flywheel, will decrease due to the parasitic losses inherent of the design. Additionally, only a single braking signal was used to control the flywheel. A more optimized way to control the braking signal would be to implement a PID controller to ramp up the braking signal as the flywheel speed decreases. And most significantly, some unknown internal code of the Sevcon controller read a fault when implementing this control scheme, necessitating a manual restart of the controller, delaying flywheel braking by around 1 second. The cause of this fault is unknown, and could not be determined through the Sevcon communication software. Future work in the area should address this issue to capture better results in this type of control strategy.

With all of the losses associate with this control strategy, an increase in the system efficiency was still realized. The efficiency was increased to 59.14%, from the 58.91% of the initial INSTAR system testing. This new efficiency lies between the optimal 5 amp maximum regeneration and the optimal 10 amp regeneration, which is where the control strategy was expected to be. (The 5 amp and 10 amp regeneration cases represent targets for the INSTAR system.) This increase in efficiency shows potential for improvements to the efficiency to exceed that of the optimal 10 amp maximum regeneration strategy, especially when one considers the shortcomings of this somewhat primitive control strategy.

Table 7: System efficiencies using threshold INSTAR strategy

Strategy	**Energy efficiency (Motor energy/battery energy)**
Maximum 10-amp regeneration target	.6052
Maximum 5-amp regeneration target	.5892
Test with INSTAR active	.5914

Using this INSTAR strategy, the battery current during regenerative braking remained below the 10 amp desired maximum. In Figure 33 two charging peaks above the 10 amp desired current can be observed, one at about 450 seconds, and the other at about 1250 seconds. These charging peaks are from the removal of current from the flywheel. Because a single brake value

was selected for flywheel braking, this can be expected. In a system which would be implemented in a commercially available vehicle, the braking signal would vary depending on flywheel speed and current read by a sensor. With further work on the control algorithms, these peaks can be limited to 10 amps, preserving the design intent of the INSTAR system.

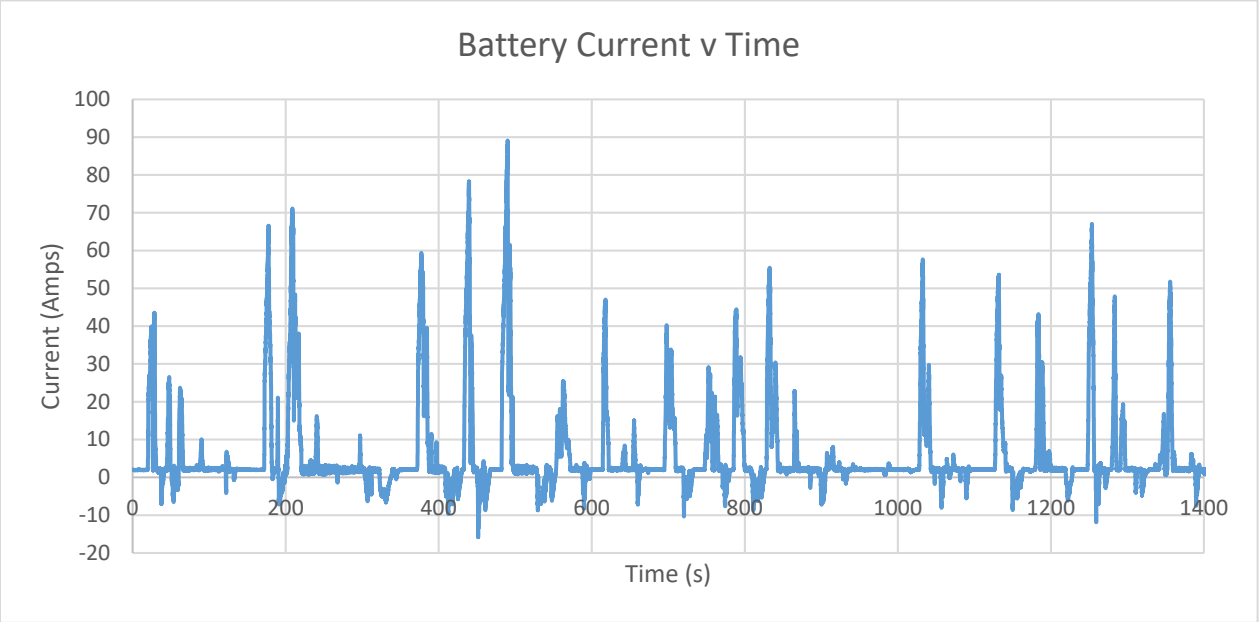

Figure 33: Battery Current v time for threshold INSTAR strategy

Another strategy attempted to increase flywheel efficiency was to put a minimum threshold on the flywheel throttle, this however did not work as intended, but is worth reporting. For the strategy, if the calculated flywheel throttle was below a certain value, the program would send 0 throttle to the flywheel motor, and would instead send a brake signal. The selected value for the minimum threshold was 35, and the selected brake value was 342 out of a potential maximum signal of 2560, which is the same brake value as used in the previous braking algorithm. This strategy brought the efficiency down to 55.49%, which is almost as bad as the no regeneration case. The reason for this seems to be in how the open loop throttle control reacts to the braking of the flywheel. The modifications to the algorithm sent oscillations through the flywheel power flow, as can be seen in Figure 34. This likely is the reason for the decreased efficiency.

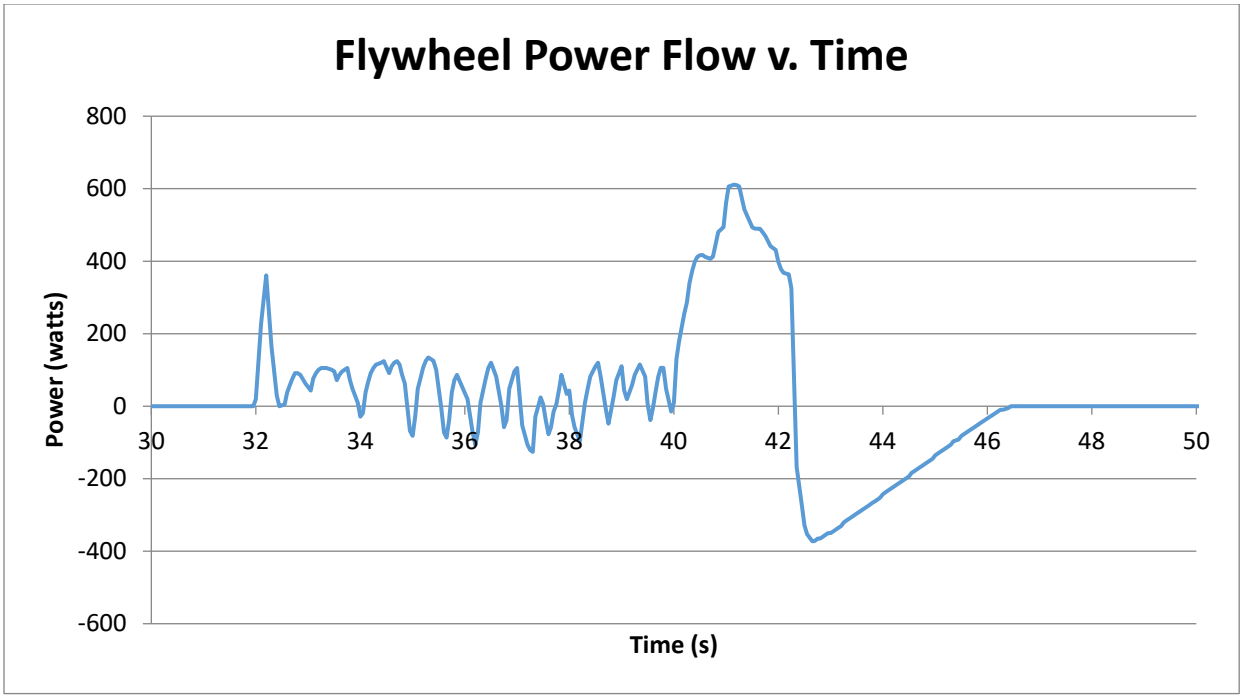

Figure 34: Flywheel power flow v. time of open loop controller with a minimum threshold placed on flywheel throttle.

Chapter VII Numerical Modelling

A computational model of a triple hybrid vehicle was created to assess different control schemes which may be applied for power system operation. The goal of the model is to simulate a standard size passenger vehicle as it travels over a predefined driving profile. The simulated vehicle will incorporate a simulated flywheel with the same parasitic losses as the INSTAR flywheel. No cap was placed on the energy storage of the flywheel partly because these modelling exercises will be used to determine the size flywheel necessary for a full-scale vehicle.

Section 7.01 Construction of numerical model

Parameters

The simulated vehicle is meant to represent a typical hybrid vehicle. For the purpose of this study, the vehicle considered is a Toyota Prius, which as a mass of 1380 kg [24]. The Toyota Prius has a drag coefficient of 0.26 with a frontal area of 2.22m^2 [25], which are necessary for calculating air drag on the vehicle at speed. A driveline efficiency of 89% was assumed for the vehicle. Meaning, that that 89% of energy would be transferred from the power devices to the wheels, or in the reverse direction. This efficiency is taken from the rolling friction of the tires on the ground [26]. A traction motor efficiency of 100% was assumed for the study. The 2017 Toyota Prius has a nominal battery voltage of 207.2 V, and a battery capacity of 3.6 Ah, or 0.75 kWh [27].

The simulated flywheel was mean to represent the INSATR flywheel deployed in the lab. The flywheel motor efficiency was set to 90%, which is actually a higher efficiency than the experimental device, but more representative of a commercially available motor. The power loss of the flywheel was set to 200W, which is a good approximation of the actual losses seen with the INSTAR flywheel. A full list of parameters can be seen in Table 8.

Table 8: Numerical Modelling Constants

Constant	**Value**	**Units**
Mass	1380	kg
Frontal Area	2.22	m^2
Drag Coefficient	0.26	
Air Density	1.225	kg/m^3
Driveline Efficiency	0.89	
Flywheel Motor Efficiency	0.90	
Power Loss Flywheel	200	W
Battery Voltage	207.2	V
Battery Capacity	0.75	kWh
Battery Capacity	3.6	Amp Hour

Model Equations

The input to the numerical model is a speed profile which the vehicle is intended to travel. From the speed profile, the vehicle power profile can be calculated. As the vehicle is moving, there are 2 conditions; one where the vehicle is inputting power to the drivetrain to propel the vehicle, and one where the vehicle is recovering energy through regenerative braking. In practice, there are three conditions, the third being when the vehicle is neither applying power to the wheels, or intaking power through regenerative braking, however, this condition was not observed in the model. In the condition where the vehicle is inputting power to the wheels, the power required to meet the speed target can be modeled by Equation 9.

Equation 9: Power required to propel vehicle

$$Power_{required} = f\left(\eta_{driveline}, m, v_i, v_f, \rho, A, C_D, \Delta t\right) = \eta_{driveline} * \frac{m\left(v_f^2 - v_i^2\right) + \rho A C_D v_{avg}^2 * d}{\Delta t}$$

When the vehicle is in the state where it is recovering energy through regenerative braking, the power recovered can be modeled as in Equation 10. This is similar to the relationship for power required to propel the vehicle, except that the drag force is subtracted from the power generated.

Equation 10: Power captured from regenerative braking

$$Power_{regen} = g\left(\eta_{driveline}, m, v_i, v_f, \rho, A, C_D, \Delta t\right) = \eta_{driveline} * \frac{m\left(v_f^2 - v_i^2\right) - \rho A C_D v_{avg}^2 * d}{\Delta t}$$

There are two power devices in the model; the flywheel and a battery. The ICE output was not placed explicitly in the model, however, the necessary output from the ICE could be calculated from the outputs of the battery and flywheel. In the model, the flywheel starts with an initial energy of 0, and its change in energy is calculated at each time step of the model. The change in energy of the flywheel can be calculated from Equation 11. The change in energy of the flywheel is used in the model to determine how much energy is available for acceleration. If the flywheel has no energy remaining, then it cannot output any power to the wheels, and the battery or ICE must be used for acceleration.

Equation 11: Change in Energy of Flywheel

$$\Delta Energy_{flywheel} = \left(Efficiency_{flywheel} * Power_{input\ flywheel} - \frac{Power_{flywheel\ output}}{Efficiency_{flywheel}} - 200W\right)\Delta t$$

In Equation 11, the power input to the flywheel could be power coming from regenerative braking, pre-charging from the battery, or pre-charging from the ICE. The power removed from the flywheel could be going to the traction motors, the battery, or both the traction motors and battery. The power loss is dissipated as heat through the ball bearings of the flywheel.

Section 7.02 Driving Profile

The driving profile selected for the model is the UDDS. For the purposes of the model, it was assumed that the driving profile was on a perfectly flat plane. The driving profile can be seen in Figure 35. The driving profile consists of many starts and stops with little to no periods of constant velocity driving.

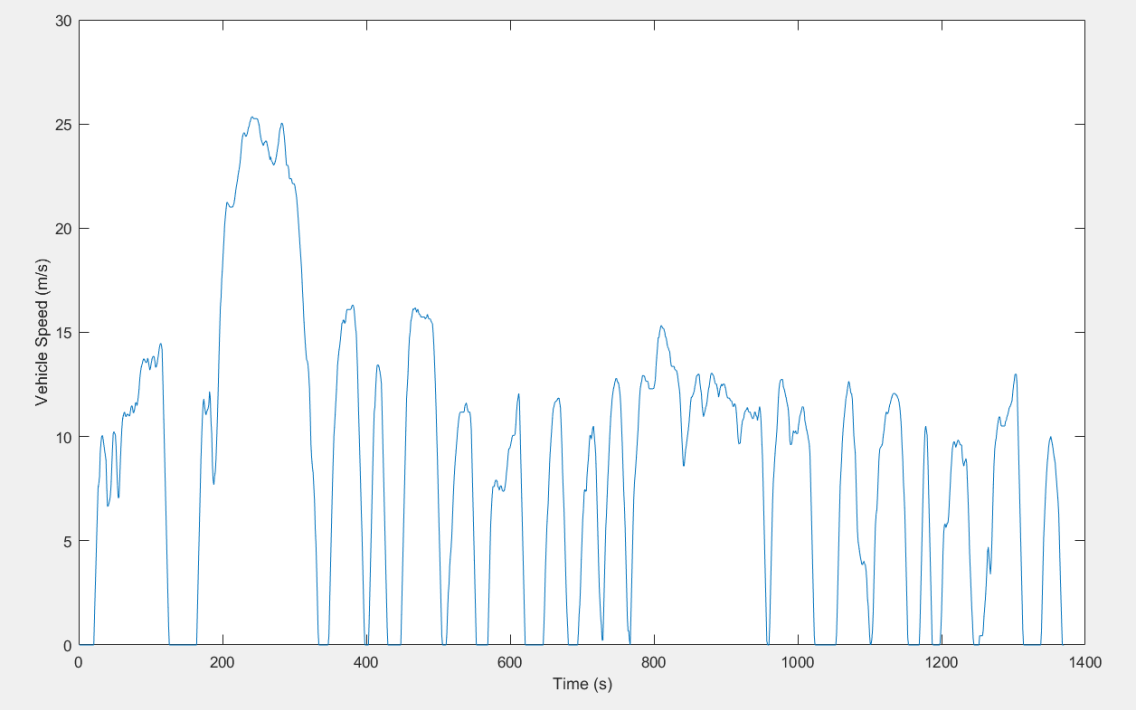

Figure 35: Driving Profile (UDDS). Speed v. Time

The power required to complete such a driving profile can be seen in Figure 36. On the graph, the power levels corresponding to a 1C, 5C, and 10C battery output are shown. It is clearly visible that almost all of the power peaks exceed the 1C level, and most peaks exceed the 5C level. If the battery were to be used exclusively for these power instances, a result would be unacceptable battery degradation. To combat this, the ICE must be used to accelerate the vehicle. But because of the narrow range of efficient operation inherent with ICEs, this may not be the best solution if one wants to create the most fuel-efficient vehicle possible.

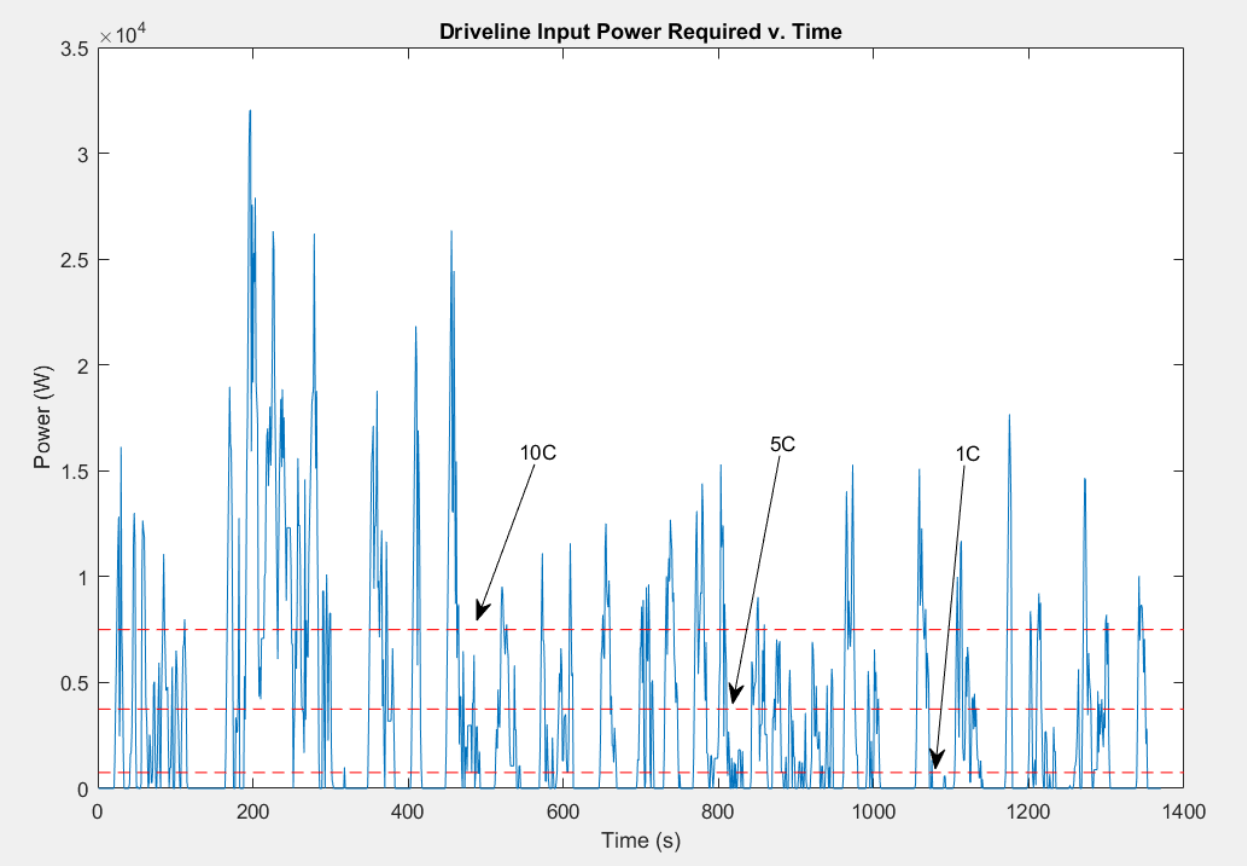

Figure 36: Driveline input power required to complete the UDDS for a typical hybrid vehicle

The peak horsepower required for acceleration of the vehicle is 43.6 according to the model. However, the average HP required is only 4.62. Thus, it is conceivable that if another device could be used for acceleration, and the ICE only be used as a generator, a much smaller and efficient ICE could be used.

Section 7.03 Utilizing a flywheel for regenerative braking and acceleration

A reasonable approach to reducing these peaks could be to use the energy captured by the flywheel to accelerate the vehicle. In such a control scheme, the energy captured from regenerative braking could be held in the flywheel until an acceleration event was observed. This would mean more energy available for acceleration, but would also mean higher parasitic losses associate with keeping the flywheel spinning for a longer period of time. Another approach is to slowly discharge the flywheel into the battery, maximizing efficiency, but would mean less energy is available in the flywheel for acceleration. It is likely that a smart control system would be needed to optimize the control strategy of the flywheel, but in this study, we will focus on the two distinct cases, and ignore a blended strategy.

First the strategy to maximize energy efficiency, where the maximum safe amount of electricity (1C for the purpose of this study where C represents the C-rate, and C-rate is the current draw which would empty the battery in one hour) is used to charge the battery, is tested.

During regenerative braking, 1C of the generated electric current is sent to the battery for charging, the remainder is sent to the flywheel. If the electric current generated from regenerative braking is less than 1C, all of the current is sent to the battery. Once the braking current drops below 1C, and the power demand of the traction motors is 0, the flywheel begins to discharge at a rate of 1C to the battery.

When the power demand of the traction motors is not 0, but there is energy stored in the flywheel, the battery and ICE combination was set to power output of 3 kW. 3 kW is the average power output required for a traditional hybrid vehicle to complete the driving cycle, and would equate to a 1C battery discharge plus a 2.25 kW (about 3 HP) ICE generator. If the power demand was in excess of 3 kW, the remainder of the power was taken from the flywheel. If the power demand was less than 3 kW, the excess power was sent to the flywheel. When the flywheel is depleted, the power must come wholly from the battery and/or the ICE. Plots showing the flywheel energy as well as the power required from the ICE/battery can be seen in Figure 37. In this strategy, the flywheel does maintain a positive energy through most of the cycle, and does not return to zero save for a few times. This may result in a larger amount of energy being dissipated than required. A more sophisticated control strategy would likely solve this issue.

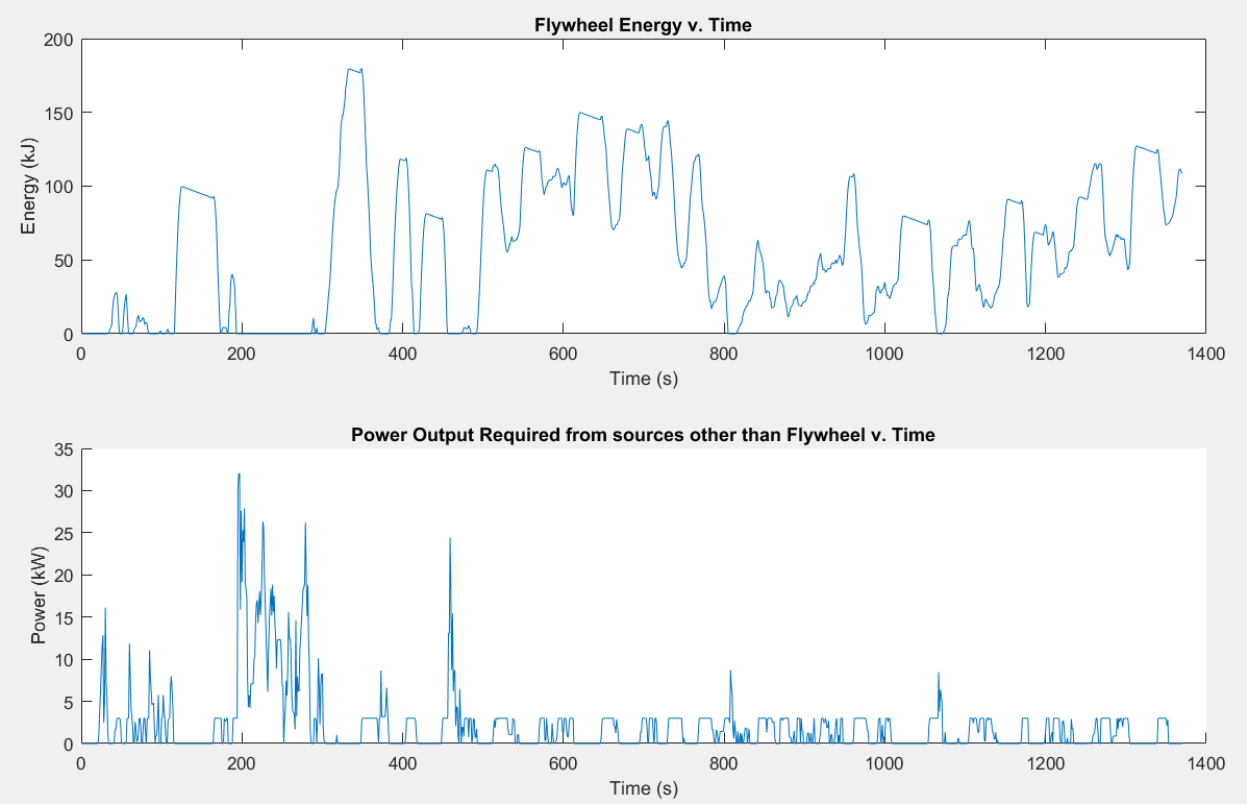

Figure 37: Plots showing flywheel energy (top) and power required from sources other than battery (bottom) for a driving strategy attempting to maximize efficiency while minimizing battery charging current.

Using this strategy, the amount of energy needed to propel the vehicle through the driving cycle reduced from 4,650 kJ to 2,490 kJ, a 46% reduction over a conventional vehicle. This

reduction in power required is calculated at a 1C charge and discharge level for the battery, and ICE output of 2.25 kW. However, the peak horsepower required from the ICE and battery combination did not change. Though peak horsepower was not reduced, there are observable reductions in the power peaks from the battery and ICE, particularly after 500 seconds of the driving cycle, which is the stop and go portion of the UDDS. This observation is shown in Figure 38.

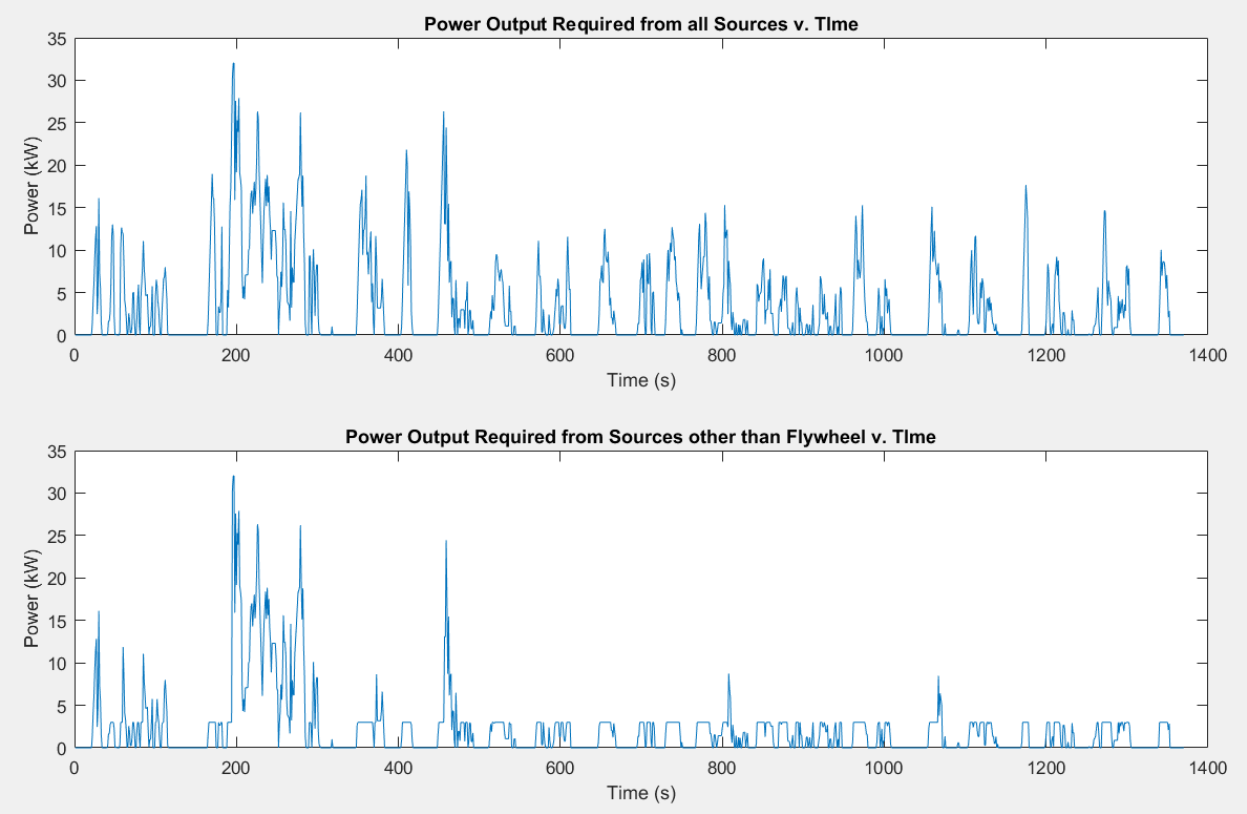

Figure 38: Total power required to complete driving cycle (top) and power required from sources other than the flywheel (bottom) for a driving strategy attempting to maximize efficiency while minimizing battery charging current.

The other strategy looked at was capturing all of the regenerative braking energy in the flywheel and sending none to the battery. This energy would be stored in the flywheel until an acceleration event occurred, where the energy in the flywheel would be used to augment a 1C discharge from the battery and a 2.25 kW ICE. In this strategy, it is known that the efficiency is likely to decrease, however the potential tradeoff could be a reduction in magnitude of power peaks required from the ICE/battery combination.

The results of this strategy had some similarities as well as some differences from the previous strategy. One major difference is that the flywheel energy steadily increases from time 500 onward, as seen in Figure 39. This results in excessive energy being stored in the flywheel, which leads to higher parasitic losses than necessary. Another difference is that the flywheel has enough energy to keep all power requirements from the ICE/battery combination below 3 kW after the 500 second mark (Figure 40), where in the previous strategy, there were two instances where the ICE/battery combination would have to provide more than 3 kW of power (Figure 38).

Figure 39: Plots showing flywheel energy (top) and power required from sources other than battery (bottom) for a driving strategy attempting to minimize discharge peaks while sacrificing a small amount of efficiency.

Where the result of the two strategies were the same was in the beginning of the driving cycle, before 500 seconds. In both strategies, the flywheel was unable to limit the discharge peaks required from the ICE/battery combination (Figure 38 and Figure 40). During this part of the driving cycle, the vehicle undergoes a small bit of driving similar to a suburban area, followed by a short trip at highway speeds. During this time the vehicle requires the highest power input to hit the UDDS acceleration targets, and also has undergone the least amount of braking, keeping energy stored in the flywheel low. Sending all of the regenerative braking to the flywheel was not enough to eliminate these peaks, but the energy consumed did increase to 2,970 kJ from 2,490 kJ in the first strategy. This increase in power is unacceptable given the limited benefit observed in the ICE/battery discharge peaks.

Table 9: Overview of power requirements needed for completion of the UDDS

Scenario	Energy Used	Average power Output from Battery/ICE Combination
Conventional Vehicle	4,649.1 kJ	3.4 kW
Traditional hybrid 1C battery limit	4,169.9 kJ	3.04 kW
Maximum efficiency with flywheel and 1C battery limit, 2.25 kW ICE	2,490.0 kJ	1.82 kW
Power Peak minimization with flywheel and 1 C battery limit, 2.25 kW ICE	2,970 kJ	2.17 kW

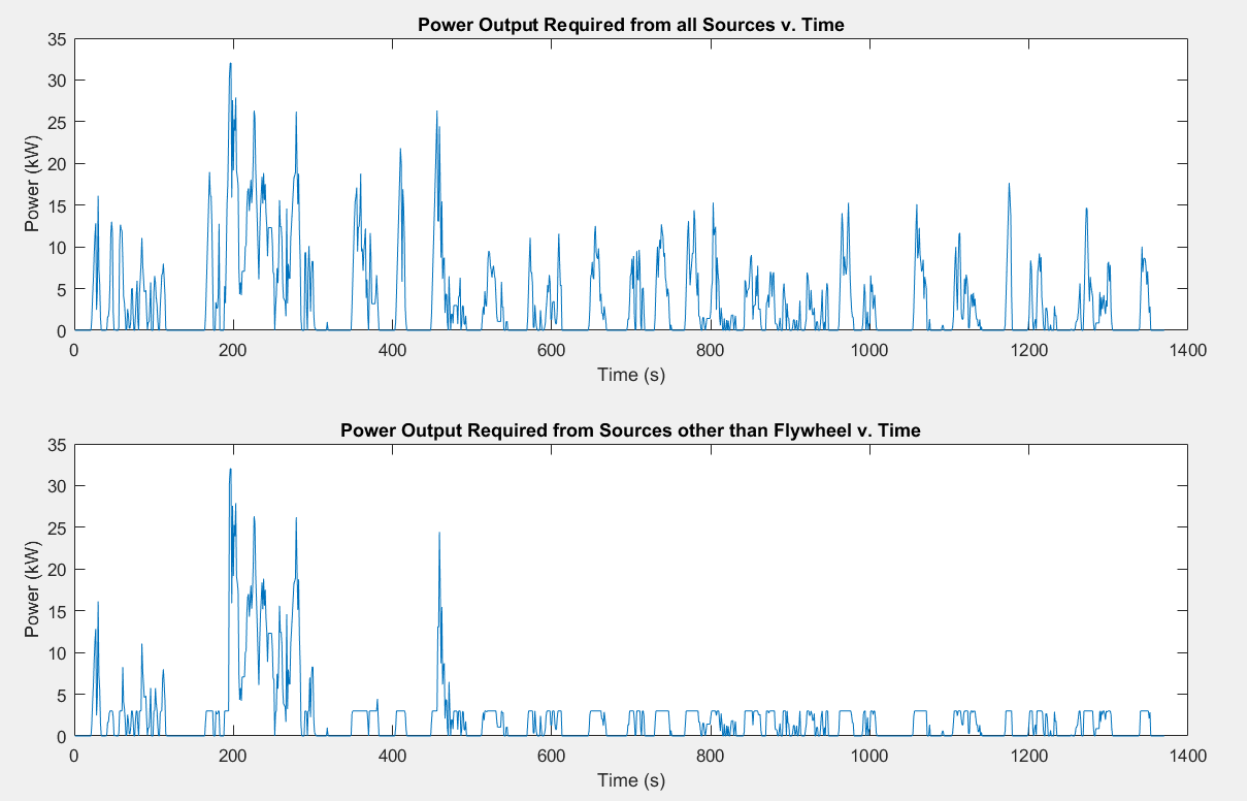

Figure 40: Total power required to complete driving cycle (top) and power required from sources other than the flywheel (bottom) for a driving strategy attempting to minimize discharge peaks while sacrificing a small amount of efficiency.

A full overview of the power energy and power levels needed to complete the UDDS for the two strategies discussed, as well as a conventional hybrid vehicle, and a conventional ICE vehicle can be seen in Table 9. Based on the overview, the strategy where the flywheel served to absorb extra braking power and was depleted as fast as possible while maintaining a 1C battery charging level was the better of the two strategies. However, and important take away is that if the power discharge peaks at the beginning of the cycle are to be eliminated, additional energy must be placed on the flywheel.

Section 7.04 Pre-charging strategies

To reduce the size of the internal combustion engine needed to power the vehicle, we must reduce the magnitude of the power peaks seen in the model. If the energy recovered from regenerative braking is not enough, then additional energy needs to be placed in the flywheel. A solution to this problem may be to pre-charge the flywheel. The pre-charging power could come from the on-board ICE, battery, or a combination of both. The goal of the pre-charging is to decrease the magnitude of power output from the ICE/battery combination so that a smaller ICE could be used, or an ICE could be designed to operate much more efficiency at a lower power level.

The large acceleration events in the driving profile occur mostly after the vehicle has come to a stop, and must accelerate up to speed. In the initial pre-charging work, the flywheel was pre-charged whenever the vehicle was stopped. The first pre-charging strategy utilized a pre-charging power of 3 kW, which is the average power output required to complete the UDDS with the flywheel activated plus a 1C discharge from the battery. This would be the most ideal set-up for energy efficiency. With such a vehicle, the ICE could act as a constant power generator, and the battery would neither lose or gain power between the end and beginning of the driving cycle. However, for this type of vehicle to work, enough energy must be placed in the flywheel at the correct times such that the flywheel always has enough energy for the upcoming acceleration event.

The strategy employed was to pre-charge the flywheel with a 3 kW power level, and to have a desired power output from the ICE/battery combination of 3 kW. The goal of this strategy is to reduce the magnitude of discharge peaks required from the ICE/battery combination, particularly before the 500 second point of the UDDS. It is known that this strategy will result in excessive energy being stored in the flywheel, as well as a decrease in the efficiency of the system, but that is not of concern for this analysis as it can be addressed with a more complex control algorithm for the flywheel.

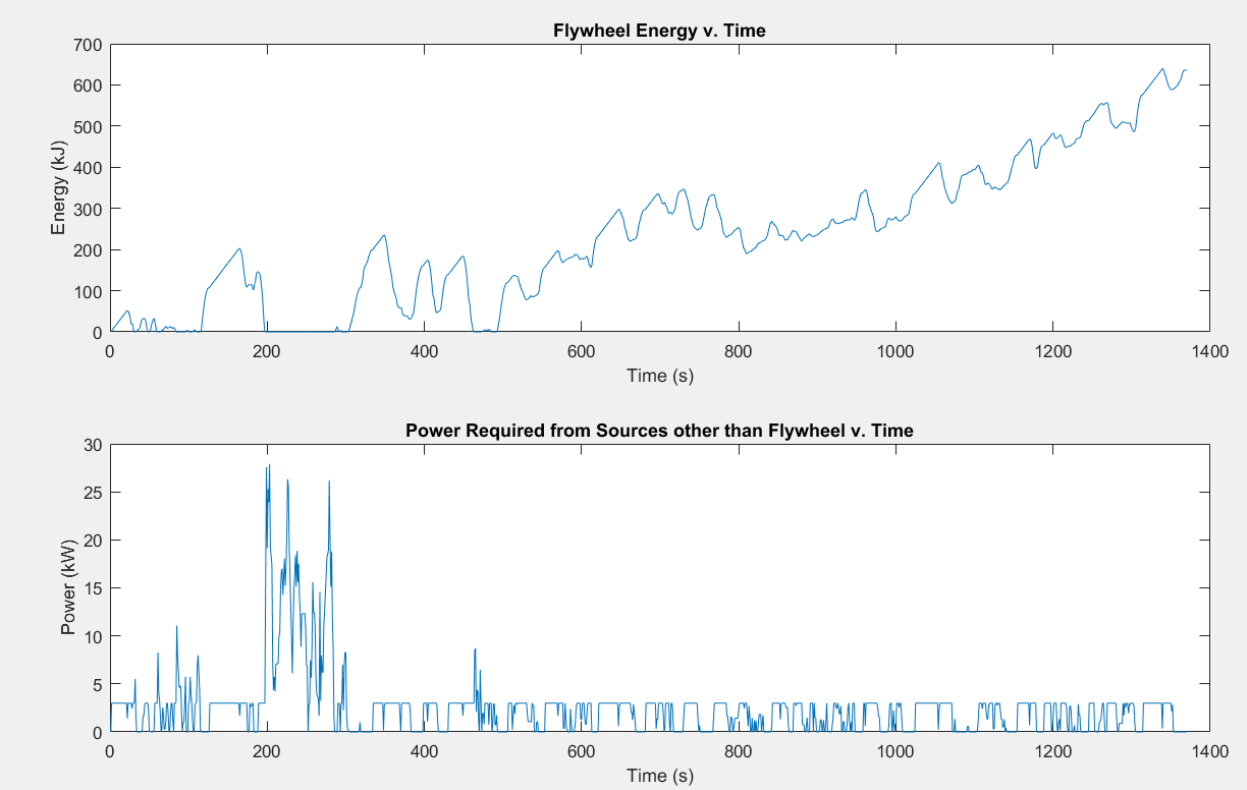

Figure 41: Plots showing flywheel energy (top) and power required from sources other than battery (bottom) for a driving strategy involving pre-charging the flywheel with a 3 kW power level.

Figure 41 shows the flywheel energy and the power output required from the battery/ICE combination. It is obvious from the figure that an excessive amount of energy is stored in the flywheel using this pre-charging strategy. However, this was expected and could be addressed with a more complex control scheme. What is more important is that the power peaks required from the ICE/battery combination have decreased in magnitude as seen in Figure 42. Power Peaks over 10 kW were completely eliminated except for the section between 200 and 300 seconds where the vehicle is travelling at highway speeds. Moreover, the peak power output required from the battery/ICE combination decreased from 32.1 kW to 27.9 kW. This reduction in power output required would have positive impacts on both the battery lifetime as well as the size of the ICE required to power the vehicle.

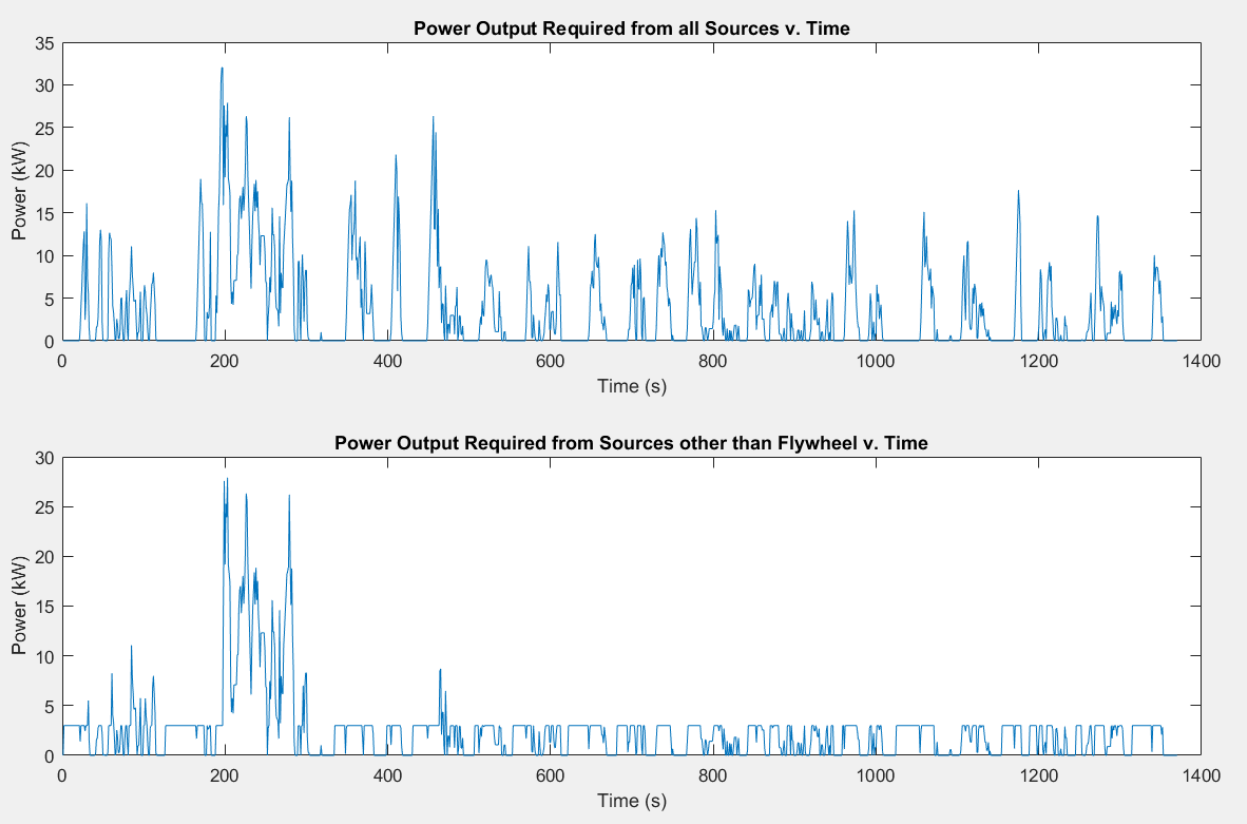

Figure 42: Total power required to complete driving cycle (top) and power required from sources other than the flywheel (bottom) for a driving strategy involving a 3 kW pre-charge of the flywheel.

The power spikes between 200 and 300 seconds are still large and would require a large ICE or battery for their output. It was desired to see what level of pre-charge and desired battery/ICE power output would eliminate these power spikes. Figure 43 shows a plot from a strategy where the power output from the ICE/battery combination never exceeds its desired power output. In this strategy, the pre-charge level was set to 6 kW, and the ICE/battery output was set to 7.5 kW. Using this strategy, the ICE could be downsized because a power output over 7.5 kW would never be required. But it is important to remember that if this strategy were used, there would be excessive energy stored in the flywheel resulting in less than maximum energy efficiency. In a production triple hybrid system, some sort of blended control algorithm would be implemented to gain the benefits of all the strategies discussed here.

Figure 43: Total power required to complete driving cycle (top) and power required from sources other than the flywheel (bottom) for a driving strategy involving a 6 kW pre-charge of the flywheel, and a 7.5 kW power output of the ICE/battery combination.

Chapter VIII Flywheel Pre-charging Laboratory Experiments

It may be desirable to decrease the output peaks of the battery of a hybrid vehicle, as it has been shown that large discharge peaks can degrade the battery at an accelerated rate [7]. Modelling has shown that regenerative braking alone is not sufficient to decrease discharge peaks out of the battery, and that pre-charging of the flywheel would be necessary. This experimental work is aimed at reducing the discharge peaks of the kart batteries.

Section 8.01 Pre-charging driving cycle

A simplified version of the UDDS was selected for the pre-charging experiments, and only the first acceleration peak was investigated as shown in Figure 44. The goal of this testing is to show the potential for flywheel pre-charging to reduce drivetrain load, not to create a production ready pre-charging algorithm. Selecting one acceleration event allows for tuning of the algorithms for a specific event, and reduces the need for a more complex control algorithm. The kart energy over the pre-charging profile can be seen in Figure 45 where the energy is stored in the rotating wheels on the kart

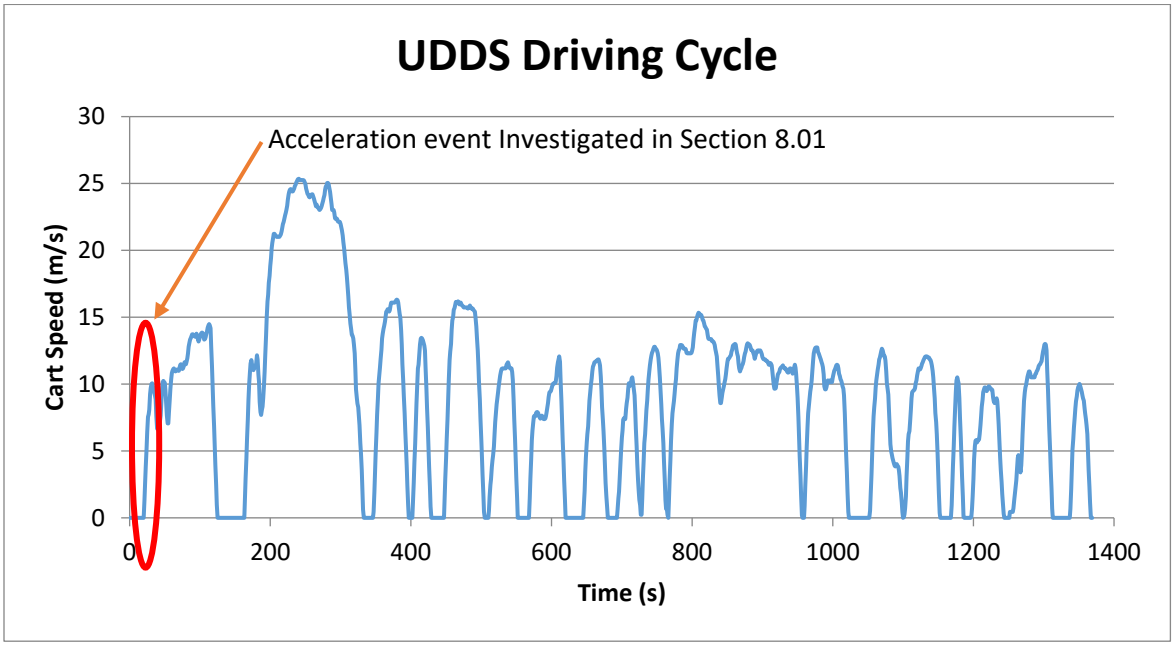

Figure 44: UDDS showing which acceleration event is used for the testing in Section 8.01

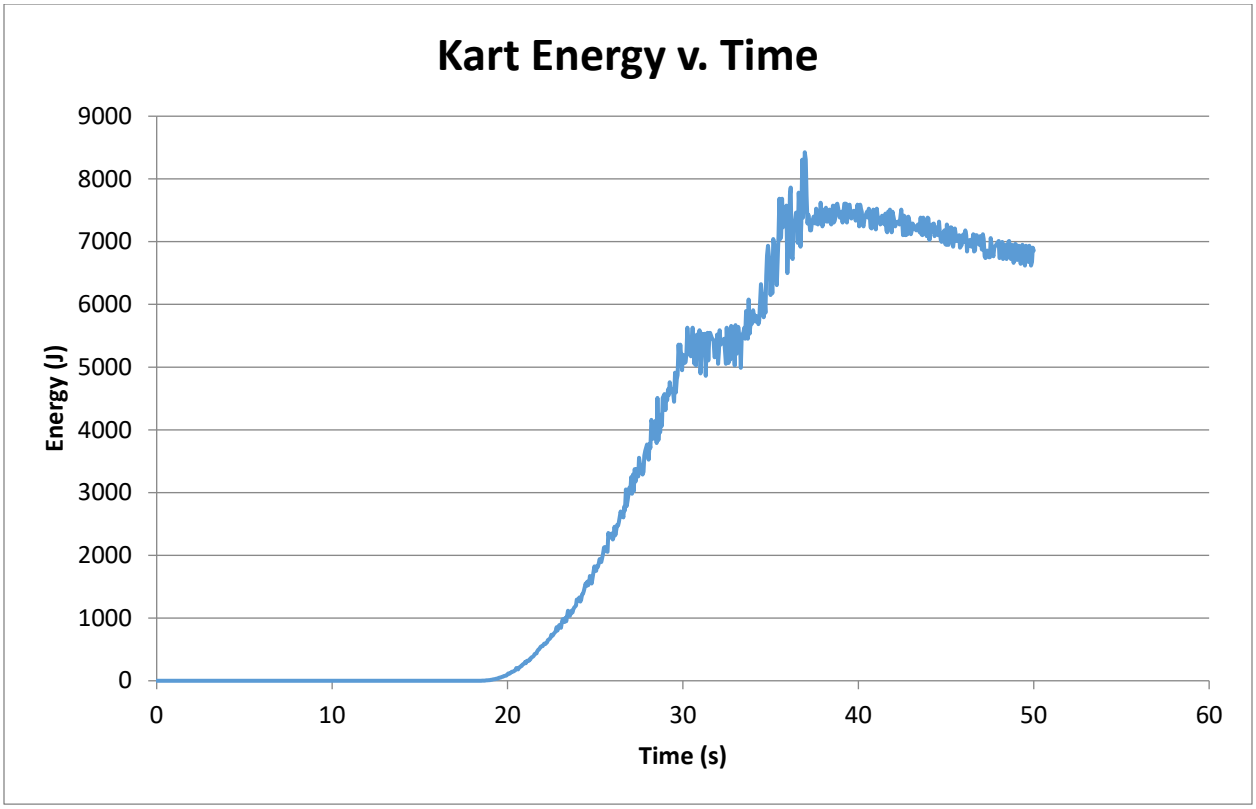

Figure 45: Kart energy v. time during the pre-charging driving profile

The current requirement for the traction motors can be seen in Figure 46. As evident in the figure, there are two distinct current peaks during the acceleration event. The first peak is a gradual rise of current to accelerate the wheels up to the profile speed. The maximum current for this peak is 62.2 amps. The second peak is a much sharper peak, where the kart is already in motion, but is quickly accelerated to a higher speed. The maximum current during this peak is 72.6 amps. For this experiment, it is desired to limit the discharge current to 50 amps, which equates to a 5C output from a 10 Ah battery, and 4 kW at 80 volts.

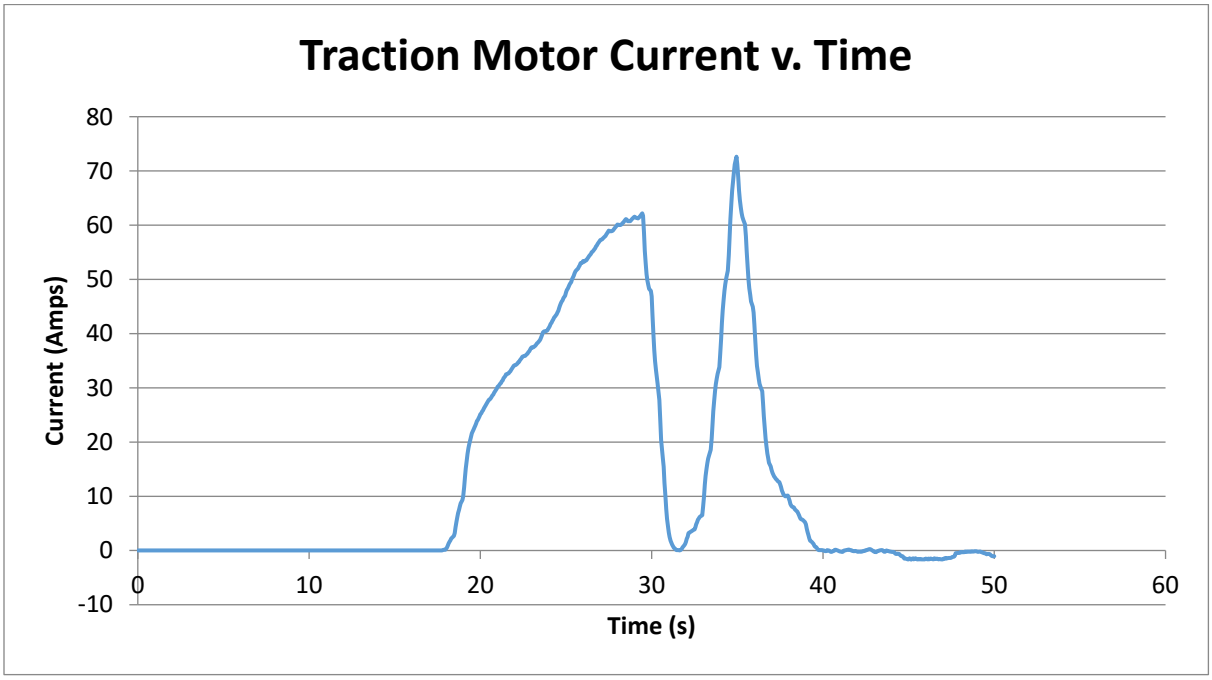

Figure 46: Traction motor current v. time for pre-charging experiments

Section 8.02 Discharging algorithm

In previous experiments, a simple braking signal was sent to the flywheel to extract energy. This was sufficient when the only goal was to remove energy from the flywheel and return it to the batteries. Because the goal now is to reduce the discharging peaks from the battery, a more complex flywheel discharging algorithm is needed. The algorithm should adjust the braking signal at the flywheel to match changes in throttle signals to the traction motors, as well as speeds of the wheels.

The algorithm employed is similar to the algorithm used to accelerate the flywheel during braking events. However, because the current flow is in the opposite direction, the sign convention of the algorithm and the torque directions need to be adjusted. The open loop control algorithm used for this can be seen below (Equation 12). The derivation of the control algorithms can be seen in Appendix A.

Equation 12: Flywheel Braking Algorithm

$$Flywheel\ Brake\ Signal = F\left[\frac{A(T_{Accel} * \omega_{Vehicle}) + BT_{Accel} - C\omega_{Vehicle}}{(D * \omega_{flywheel} - E)}\right]$$

During tuning of the algorithm similar coefficients for A, B, C, D, and E were found to be acceptable. However, a much larger F coefficient was necessary to produce enough current out of the flywheel to offset the traction motor current, which is due to the internal programming of the Sevcon motor controller. The tuned coefficients can be seen in Table 10. The value of E for the tuned algorithm has a negative coefficient, making it the same as the flywheel throttle signal algorithm used before. The impact which E has on the algorithm is small and is mostly seen at low flywheel speeds. Because the flywheel brake signals will mostly be seen at high flywheel speeds, the value of E used in the throttle algorithm was sufficient to have the flywheel brake algorithm work reasonably well.

Table 10: Tuned coefficients for flywheel braking during pre-charging experiments

Coefficient	Value
A	0.4
B	0.4
C	0.12
D	0.4
E	-2.7
F	50

Section 8.03 Pre-charging strategy

For the experiment, the flywheel was pre-charged with a constant throttle signal. The throttle signal was sent to the flywheel via user input, and not by an algorithm. The flywheel throttle signal was initiated 12 seconds before the start of the acceleration event. A constant flywheel throttle signal was used for the experiment, however in production, a more complex and sophisticated throttle signal algorithm should be used to maintain a constant current travelling to the flywheel while minimizing spin up time to reduce parasitic losses. The flywheel speed and current requirements during the pre-charging can be seen in Figure 47.

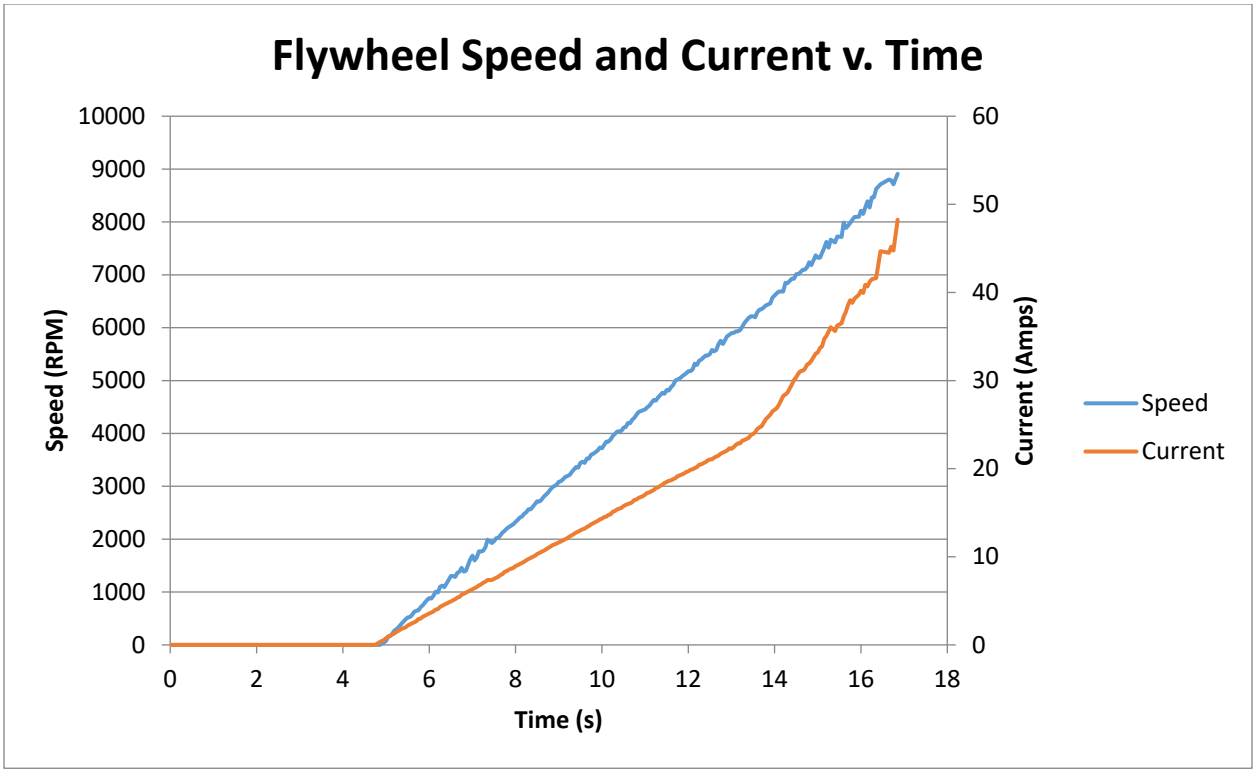

Figure 47: Flywheel speed and current requirements during pre-charging event

The current requirements of the pre-charging event reach 50 amps, roughly 5C of the fictitious vehicle battery pack (1.25C of the actual battery pack which is substantially larger than most hybrid vehicle battery packs). 5C is a reasonable maximum current requirement from the vehicle battery and ICE. During modelling, a 4C pre-charge value was shown to have positive results on current peaks. This 5C current requirement equates to a power output of 4kW from the battery and ICE. A 1C draw from the battery (0.8 kW) would leave the ICE requirement at 3.2 kW, which given the size vehicle, is a relatively small power output. Current racing karts use an 8.56 kW engine as per the Commission Internationale De Karting regulations [28].

Section 8.04 Pre-charging Results

The current results from the pre-charging experiment can be seen in Figure 48. The flywheel algorithm successfully limited the traction motors to 5C during the first current peak. As soon as the traction motor current requirement reached 50 amps, the flywheel brake algorithm sent braking signals to the flywheel. The braking signals produced a positive current out of the flywheel which offset the traction motor current. During the period where the flywheel braking algorithm was activated, total current demand from the battery dropped, and stayed below 50 amps for the remainder of the current peak. To achieve this, the flywheel speed dropped from 9000 RPM down to 0 during the first current peak (Figure 49) and was unable to provide any current during the second current peak.

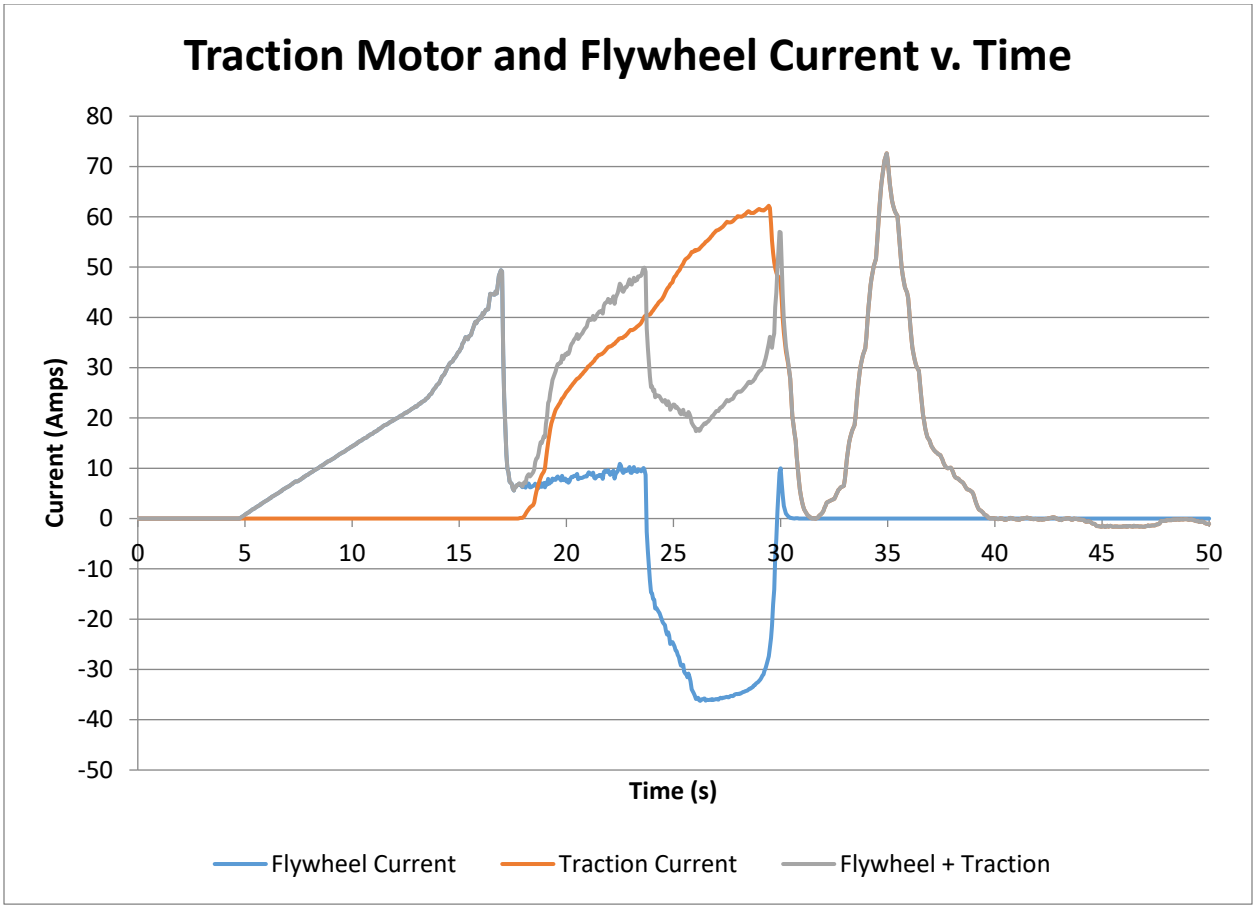

Figure 48: Traction motor current, flywheel current, and battery demand during pre-charging experiment. The Flywheel + Traction profile is the power output required from the battery pack.

The pre-charging experiment was successful in lowering the discharge current required from the battery; however, there are some areas which may be improved upon. Firstly, the braking algorithm provided a larger than necessary braking value to the flywheel. This resulted in the power output required from the battery pack dipping to less than 20 amps during the acceleration event. This overshoot of the flywheel braking algorithm means that more energy than necessary was removed from the flywheel. If the flywheel braking algorithm were to produce a more optimized braking signal, the energy in the flywheel could possibly be preserved through the acceleration event and be used to lower the magnitude of the second current peak.

In the flywheel current profile, a positive offset from 17 to 24 seconds can be observed. This positive value was not intended, as no throttle or brake signals are being sent to the flywheel at this time. This positive offset is likely an artifact of the internal programming of the dedicated Sevcon motor controller. An unintended consequence of the offset is that during this time the flywheel maintains its speed, and even accelerates slightly. And in doing so only draws 10 amps, and does not send the battery current requirement over the 50 amp level. Because this unintended consequence has positive results it was not investigated any further.

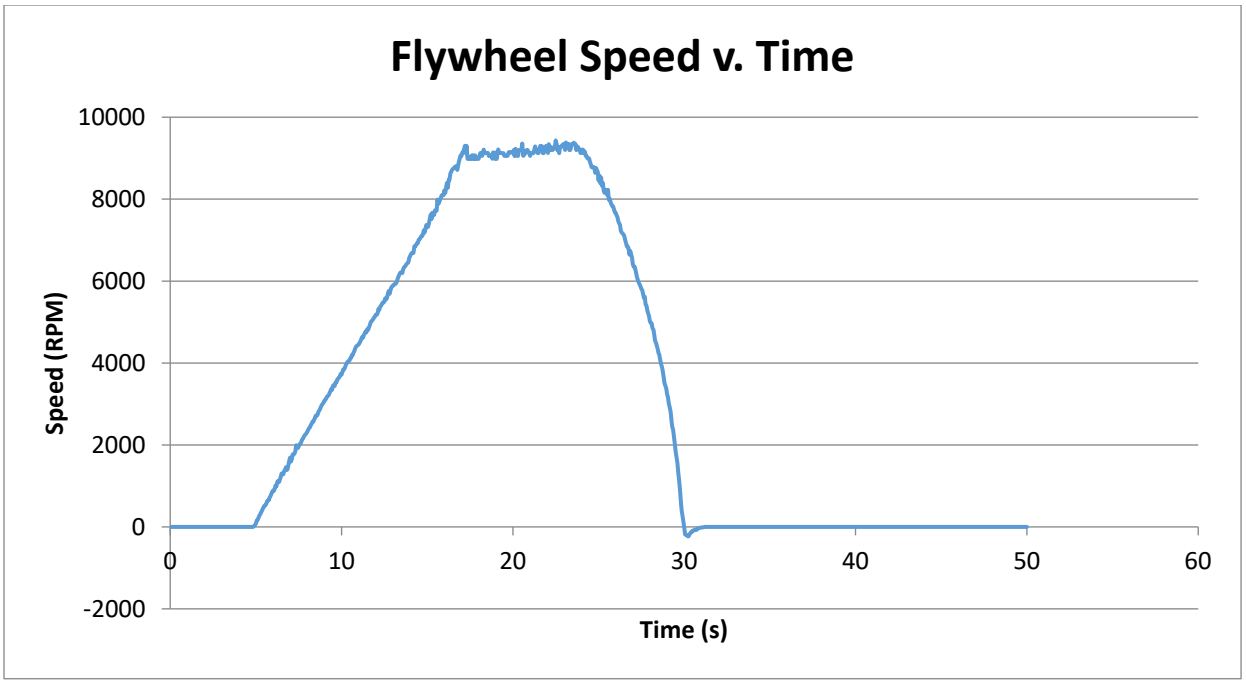

Figure 49: Flywheel Speed during pre-charging experiment

Another aspect of the flywheel current profile which is interesting is the positive spike at the end of the first current peak. This positive value sends the battery current requirement above 50 amps and needs to be investigated. This positive spike could come from the Sevcon controller attempting to bring the motor to a stop as quickly as possible. Figure 49 shows that as the flywheel is discharged, the velocity rapidly approaches 0, then overshoots, and spins in the other direction for a short amount of time at the 30 second mark. The Sevcon controller is attempting to bring the flywheel to a zero velocity as fast as possible by supplying a positive current to the flywheel.

The Sevcon controller has an internal PID controller which converts throttle and brake signals to motion of the flywheel. PID controllers work by correcting errors from a designated set point. The gain values of a PID controller dictate how it responds both with the initial time deal, and if the signal will have any overshoot. Figure 50 shows a PID controller output, and displays both the initial time delay and overshoot, in this case the system is underdamped and the system oscillates around the set point. A similar phenomenon is occurring in the experiment here, where the high braking loads on the controller has sent it spinning on the opposite direction, forcing the Sevcon controller to supply a throttle signal to bring the flywheel velocity to zero.

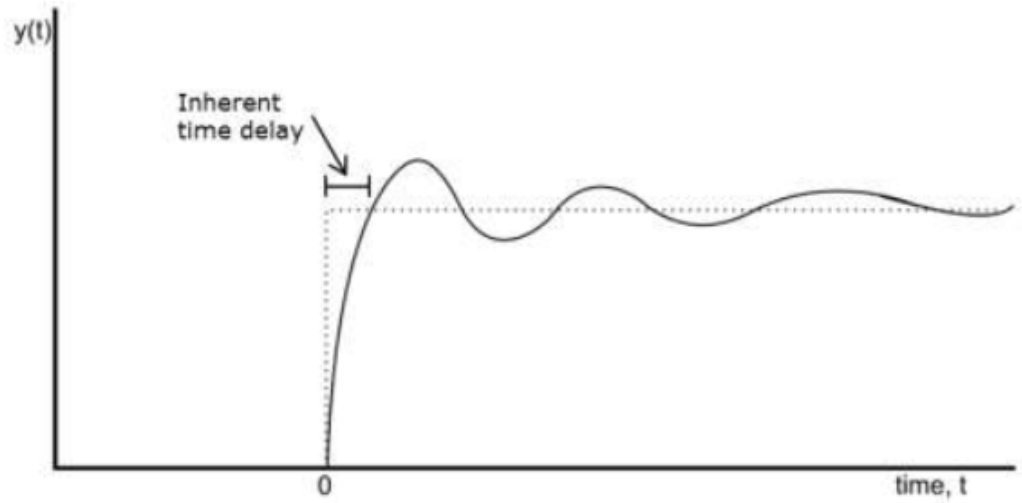

Figure 50: Example of PID step response. Courtesy of Talancon Thesis [22]

Modifications to Algorithm to Address Flywheel Current output

To address the overshooting of the flywheel current output, the coefficients in the algorithms were modified. The most logical approach is to reduce the F coefficient in the algorithm. This would lower the overall magnitude of the algorithm, with the desired result only decreasing the magnitude of the flywheel output, not changing the timing of the output or the shape of the current profile. The value of the F coefficient was changed from 50 to 40, and the new coefficients can be seen in Table 11.

Table 11: modified algorithm constants for pre-charging experiments

Coefficient	Value
A	0.4
B	0.4
C	0.12
D	0.4
E	-2.7
F	40

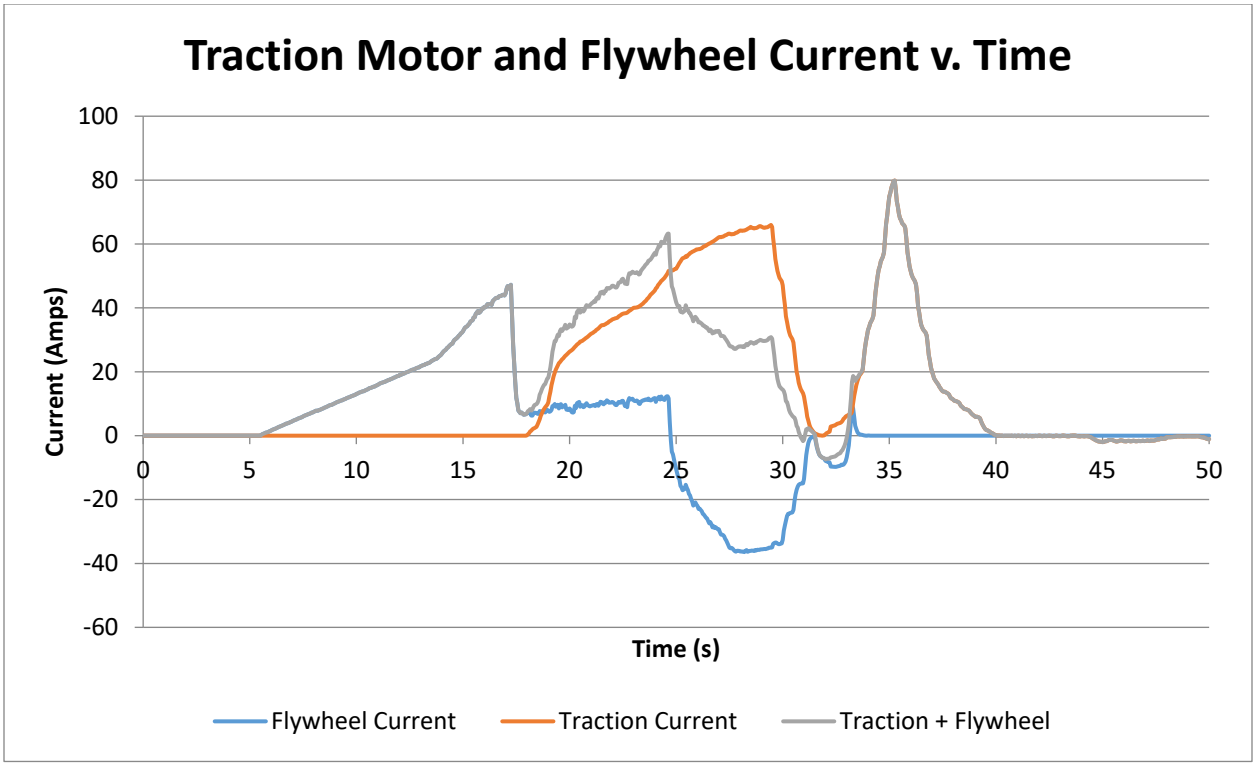

Figure 51: Traction motor, flywheel current, and battery demand with modified algorithm coefficients

The result of the change to the algorithm coefficient was not as desired. The flywheel only had a small amount of energy after the first current peak, and was unable to address the second current peak fully. There was some energy left in the flywheel after the first current peak, which was used to offset the beginning of the second current peak but was insufficient to have significant results (Figure 51). Changing the coefficient value also had the negative effect of decreasing the algorithm effectiveness of reducing the battery output requirement. The algorithm was not able to react fast enough to the changing traction motor current, and the battery current demand crossed the 50 amp threshold before the flywheel was able to provide any current.

The most likely component of the system causing this delay is the dedicated Sevcon controller. The controller is likely expecting a higher braking signal than the algorithm is outputting. Changes to the controller internal programming might be necessary to fix this problem. But if the problem within the Sevcon controller was addressed, the change to the F coefficient seems to indicate that improvements the algorithm could be tuned to better utilize the stored energy within the flywheel.

Pre-charging the flywheel twice

In an attempt to reduce the second current peak, the flywheel was charged in the valley between the peaks. The pre-charging event lasts 1.75 seconds and occurs when the controller current is below 15 amps. A plot of the flywheel throttle and traction motor throttle can be seen in Figure 52. This second charging event is designed to add additional energy to the flywheel

which can be used to offset the power demand of the traction motors. A successful implementation of the strategy would keep the second flywheel pre-charging event below 50 amps, while decreasing the second traction motor current peak, keeping all current peaks below 50 amps.

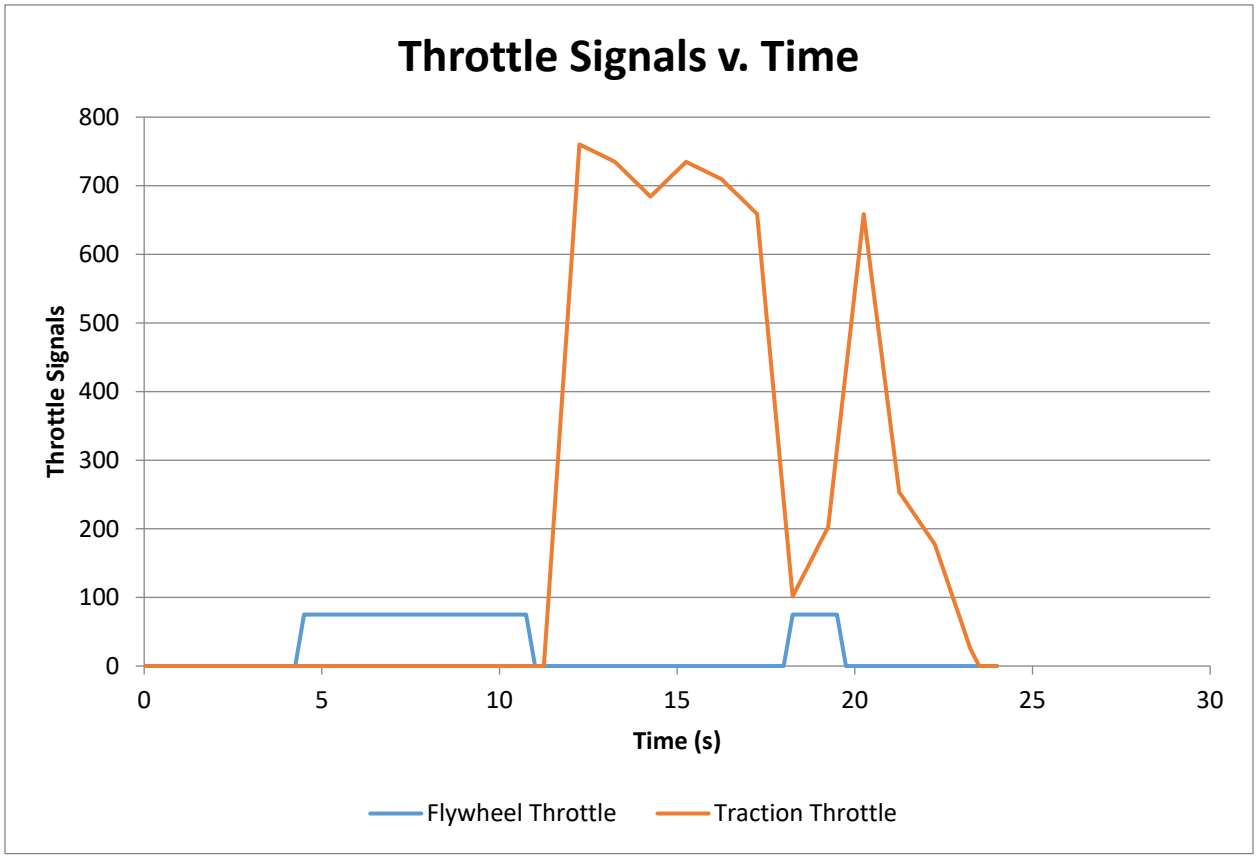

Figure 52: Throttle Signals v. Time for double pre-charging strategy

Using the double pre-charging approach alone did not achieve the desired results. The Sevcon controller was unable to react to the second pre-charging instance once the flywheel had come to a complete stop. Figure 53 shows the currents of the flywheel and motor over the driving cycle with the double pre-charge strategy. The currents do not differ at all from the previous trials, and the second power peak is not reduced at all. To address this problem, the next strategy will attempt to place enough energy in the flywheel that it is still spinning after the end of the first current peak, so that it can be pre-charged for the second current peak.

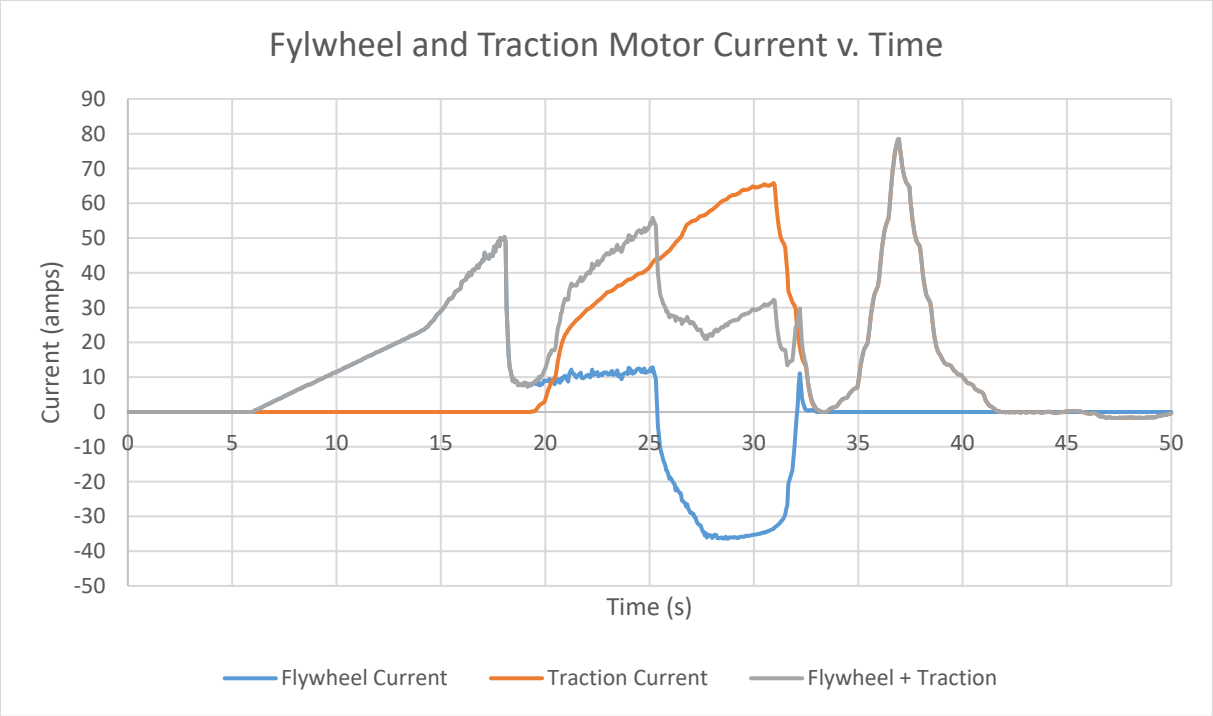

Figure 53: Flywheel and Traction motor current v. Time for a strategy with 2 pre-charging instances and a throttle signal of 75

Increased Throttle Signal with pre-charging two times

To address the issues seen with the Sevcon controller, the flywheel was pre-charged with more energy than needed to offset the first current peak so that it would still have rotational energy at the second pre-charging instance. To achieve this, the throttle signal input was increased to 100 from 75. The timing and duration of the throttle signals remained the same as is observed in Figure 52. The peak rotational speed of the flywheel was 11,000 RPM (Figure 55), 22% higher than the previous experiments. The consequence of this is that the flywheel pre-charge current peaked over 50 amps (Figure 54). This was anticipated, and in a production control system could be eliminated with a more complex pre-charging control algorithm. In these experiments a constant throttle signal is supplied to the flywheel with no feedback from the flywheel. If either an open loop control or closed loop control system were implemented, the current to the flywheel could be kept below the desired setpoint.

The results from the experiment are promising. The combined current demand passed the desired 50 amp level 3 times, during the initial pre-charge, before the flywheel brake was activated, and during the last pre-charge. All of these instances were because of currents drawn by the flywheel, and not from currents drawn from the traction motors. As discussed earlier, placing a more complex control algorithm on the flywheel throttle signal would be able to control these flywheel currents, and keep the desired battery current draw below the desired set point.

During all of the traction motor acceleration events, the flywheel was successful in keeping the battery current below the desired 50 amp level. The flywheel maintained enough energy after the first current peak to keep the second current peak below the 50 amp threshold. This was the desired result of the experimental trial. However, there are aspects of the trial which can be improved upon.

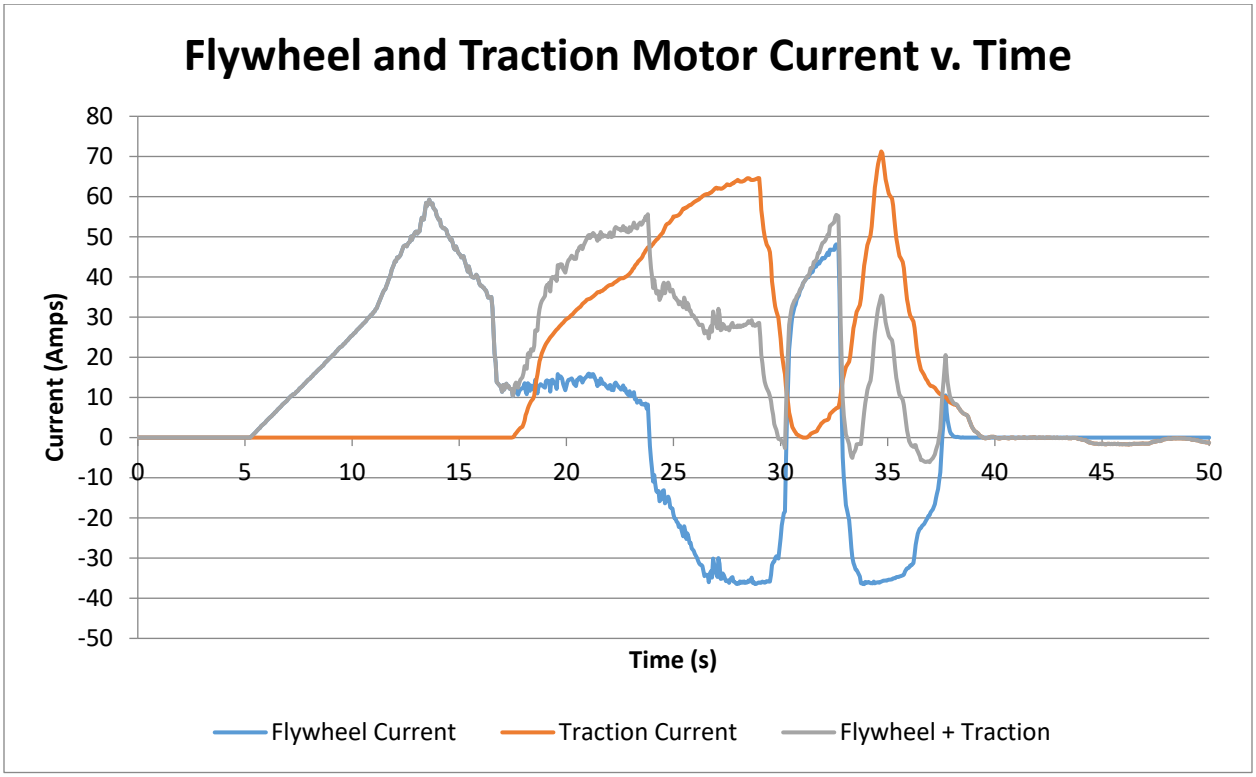

Figure 54: Flywheel and traction motor currents v. time for pre-charging experiment with increased throttle signal.

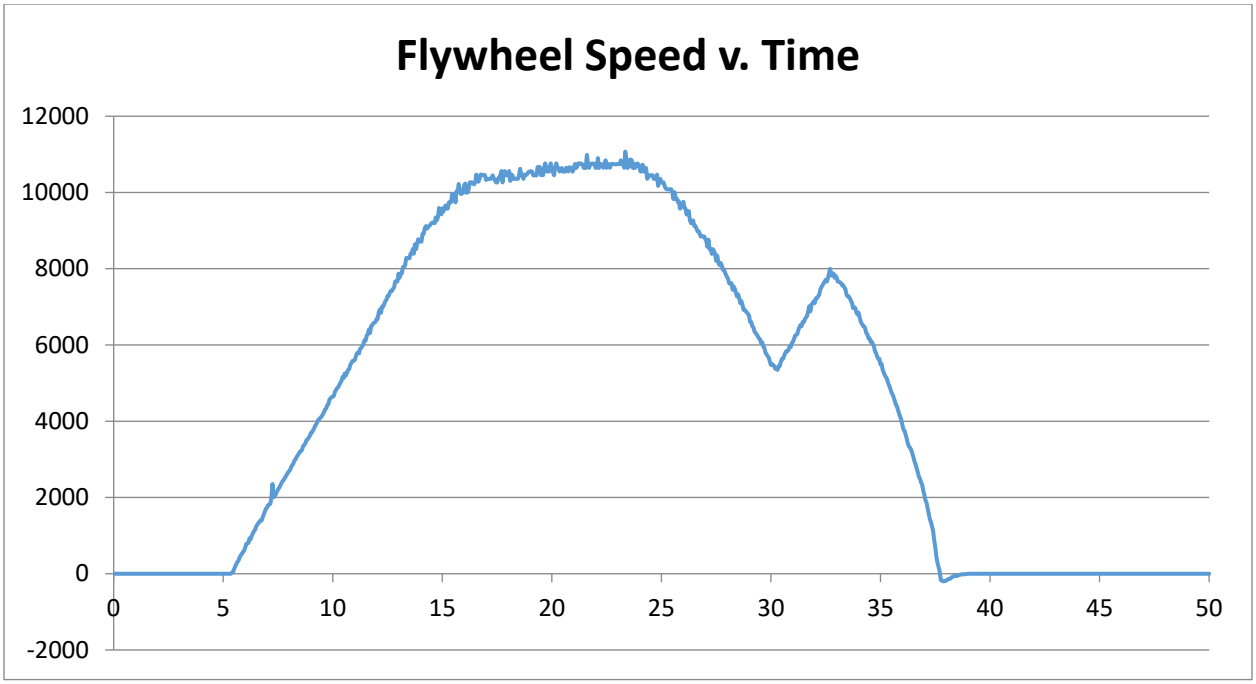

Figure 55: Flywheel Speed v. Time for pre-charging experiments with increased throttle signal.

The battery current draw when the traction motors are activated drops significantly below 50 amps (Figure 55). This is unnecessary, as holding the battery draw at 50 amps would be sufficient. In fact, a more constant power draw from the battery would be more efficient for the vehicle. It would also decrease the amount of energy needed to be stored in the flywheel and therefore decrease the amount of energy dissipated from parasitic losses of the flywheel. A closed loop controller implement on the flywheel throttle signal could solve this issue. Given the difficulty of implementing a closed loop control on the regenerative braking algorithm, a closed loop control on the flywheel throttle is not likely to be successful with the laboratory hardware.

Efficiency of the system was not the goal of this experiment, as a much more efficient control strategy would be needed to maximize efficiency. However, the traction motors used a total of 50.4 kJ of energy during the first 40 seconds of the acceleration event, and the flywheel used a total of 14.8 kJ of energy for the same amount of time. Making the total amount of energy used 65.2 kJ of energy, or a 29% increase over only using the traction motors. Using a flywheel in such a manner will always increase the amount of energy used in a fully electric vehicle as in the lab, because there will be added losses associated with the flywheel bearings and motor efficiency. The tradeoff for this increase in energy usage is the limiting of discharge currents, and the possibility to use simpler, cheaper, and lighter components in the production vehicle.

Section 8.05 Discussion of Pre-charging Experiments

The pre-charging experiments in the lab are meant to be exploratory in determining if pre-charging the flywheel is a viable strategy to reduce battery discharge currents. The laboratory experiments proved that in fact it is a viable strategy. Battery discharge currents during vehicle acceleration were kept below a desired set point. It was demonstrated that the flywheel is capable of storing enough energy to limit the battery discharge through a full acceleration event, and can be recharged with more energy should it be necessary.

More work is needed to increase the effectiveness of the pre-charging throttle signals. A simple constant throttle input was used for these trials. A more complex closed or open loop control algorithm could be used to keep flywheel currents below a certain level, decrease flywheel acceleration time, and decrease parasitic losses. More work is also needed on the algorithm governing flywheel energy discharge. The algorithm was successful in limiting battery discharge current, however, more energy than required was removed from the flywheel. This could have adverse effects on the system efficiency, both in terms of the flywheel, and from a less than optimal operating point of the ICE. The control optimization of these two aspects are left to future members of the INSTAR lab.

Chapter IX Road Testing

Laboratory testing proved to be insufficient for many aspects of the research. In the laboratory, the operating energy levels of the kart needed to be kept lower than what would be expected in a real-world driving situation. This limit of energy, means that the flywheel could not properly be evaluated for its ability to prevent high regeneration currents from reaching the batteries, and an accurate estimation of the energy efficiency the system would be on the road could not be achieved. For these reasons, road testing was conducted at more realistic energy levels.

Section 9.1 Road Testing Set-up

The road testing was conducted at the UC Berkeley Richmond Field Station (Figure 56). The Richmond field station has several flat paved sections of roads which can be used for realistic tests at driving speed. For the testing, it was desired to have a repeatable driving profile, so one was programmed which could be repeated for every test with no human input. The profile for the testing was a simple acceleration and deceleration profile, which can be seen in Figure 57. To obtain the driving profile, the author drove the kart recording throttle and brake inputs, which were used to create the profile.

Figure 56: The testing site at the Richmond Field Station at UC Berkeley

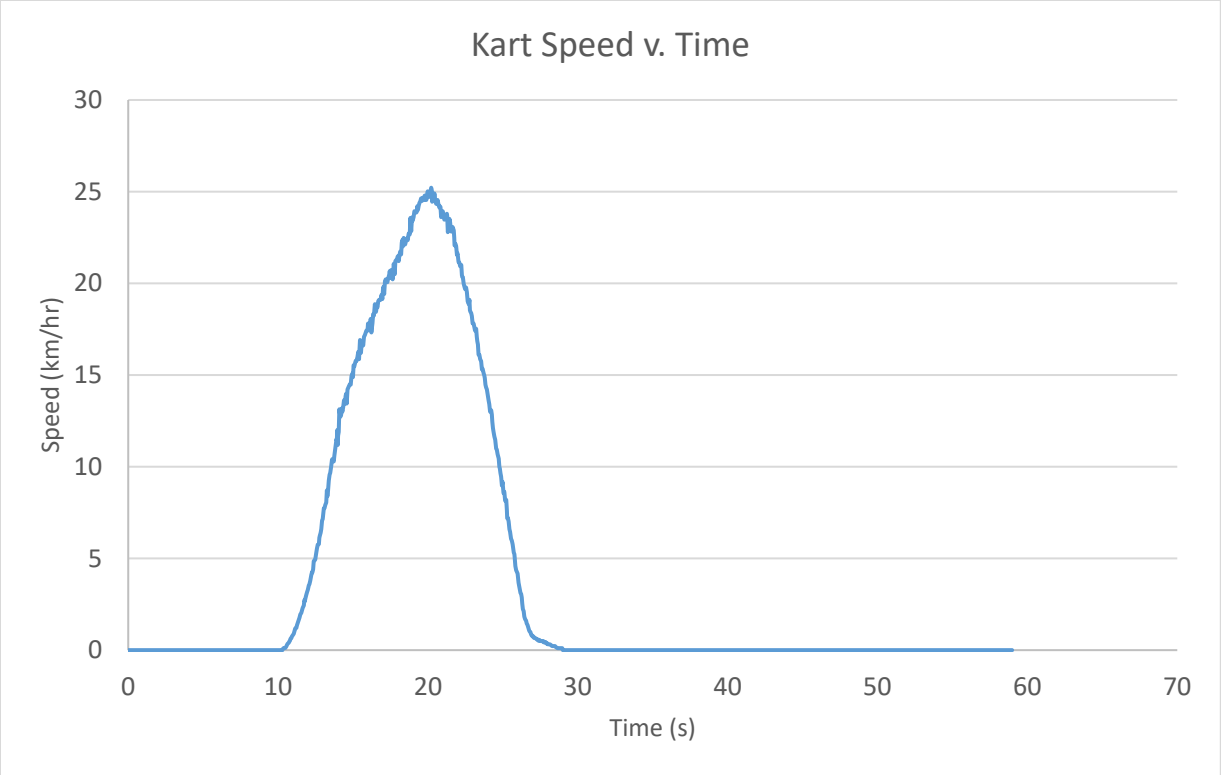

Figure 57: Road Testing Driving Profile

During testing, the same driver was used for all of the runs to maintain constant kart and driver mass. The same stretch of road was used for all of the trials, and the kart was used for no more than 8 driving profiles before it was returned to full charge to reduce any dependence on battery state of charge. The current as read at the traction motors during the driving profile can be seen in Figure 58. The current during acceleration reaches a maximum of 187 amps, with the majority of the acceleration event having a current of over 100 amps. During deceleration the maximum regeneration current from the traction motors is 63 amps.

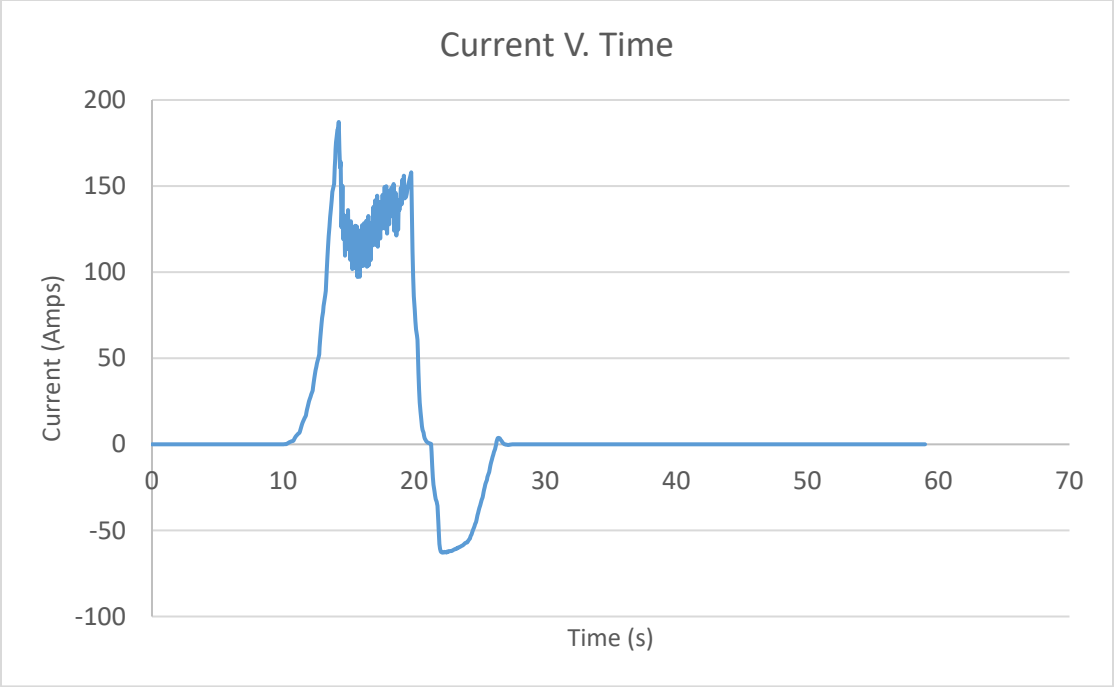

Figure 58: Road Test Traction Motor Current v. Time. This plot displays run 1 from Figure 59.

There was a high repeatability between the trials. Figure 59 shows a graph of the traction motor current during the driving cycle over 5 separate runs. In the graph there are only small deviations from the current profile between the runs. Because of the consistency in the traction motor current, the flywheel results should also show the same consistency.

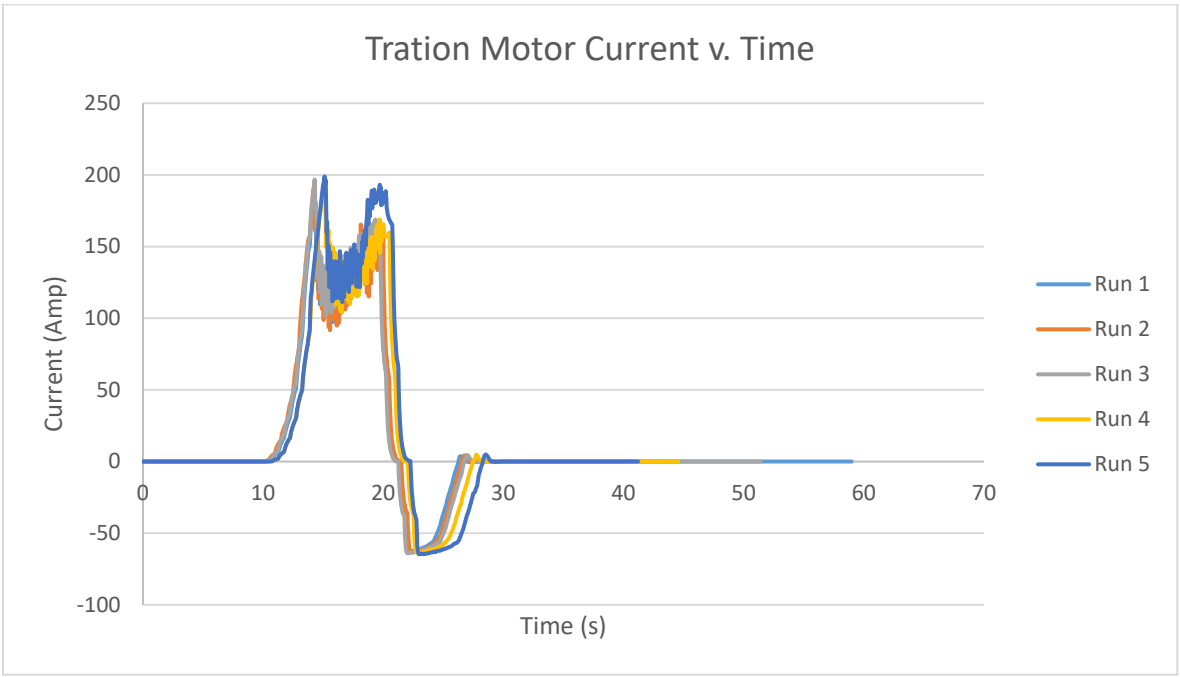

Figure 59: Graph showing traction motor current over 5 separate runs

Section 9.2 Road Testing with the INSTAR Flywheel Activated

It is desired to keep the regeneration current entering the batteries less than 20 amps during the road testing. The same flywheel throttle algorithm was used as described in Chapter V, and a constant brake value was sent to the flywheel to remove the stored energy as was done in Chapter VI. The maximum flywheel braking torque allowed is only 19.5% of the full braking torque of the flywheel motor during the energy removal to keep the current to the battery below 20 amps. Using this simple strategy, the magnitude of regeneration current reaching the battery was greatly reduced. The maximum regeneration current reaching the battery with the flywheel activated was 25.9 amps, a 58.7% reduction in the magnitude of charging current. The current reaching the batteries during the flywheel activation road testing can be seen in Figure 60. The flywheel tests demonstrated the same repeatability as the traction motors. Figure 61 shows the current at the battery for 4 separate runs with the flywheel activated. Figure 62 shows a representation of the electrical systems shown in the plots of Figure 60 and Figure 61.

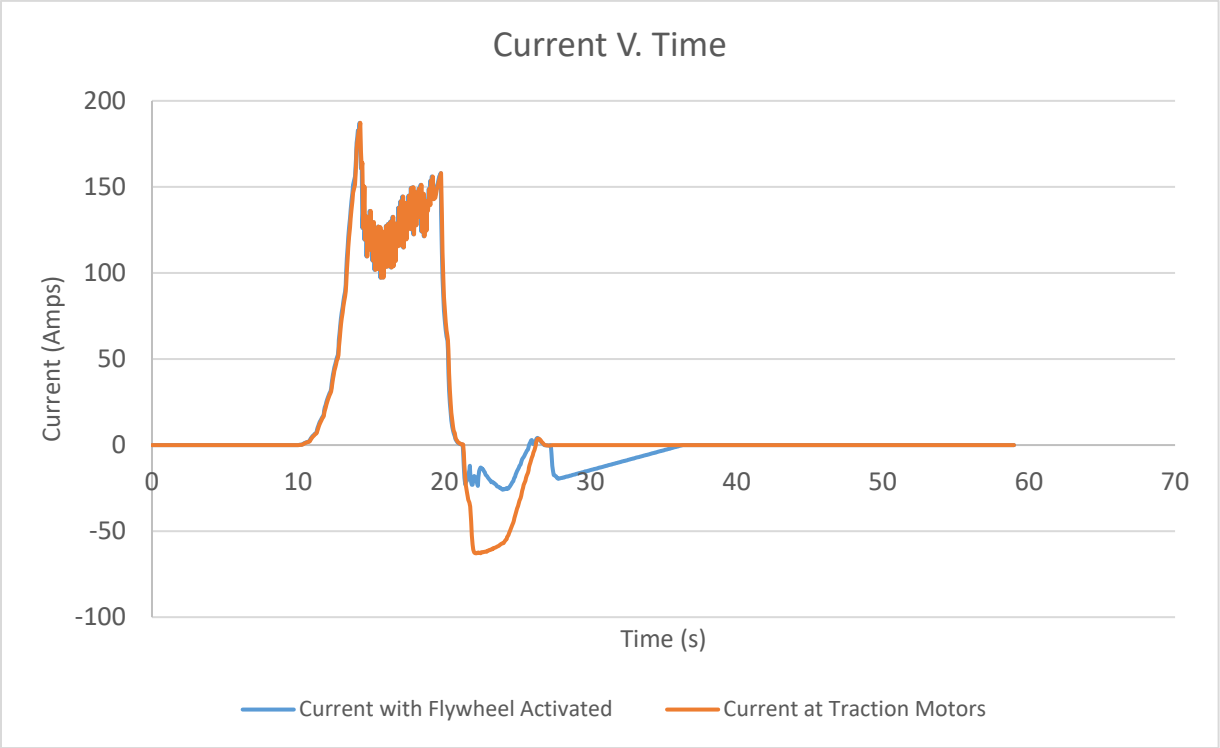

Figure 60: Road Testing Current with the INSTAR Flywheel Activated. In this plot, the current at the traction motors is the amount of current generated or consumed at the traction motor. The current with flywheel activated is the current supplied or consumed by the battery pack.

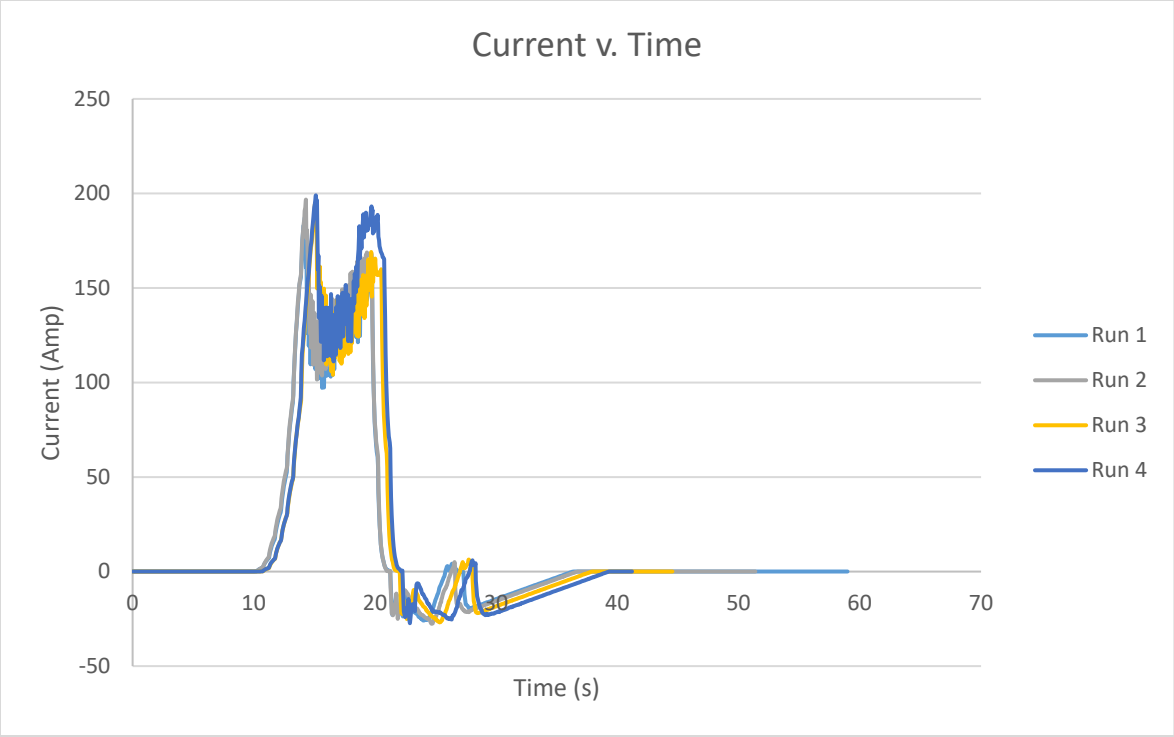

Figure 61: Graph showing the current profiles with the flywheel activated over 4 separate runs

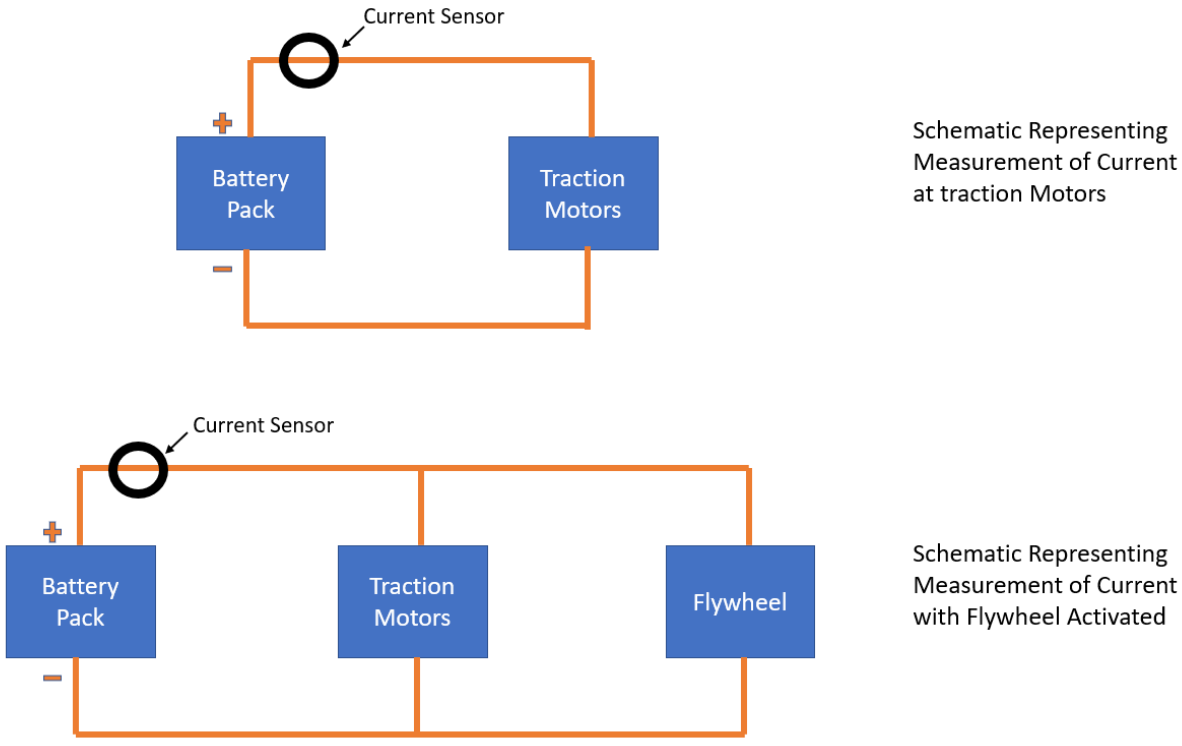

Figure 62: Schematics depicting the measurements of current of the traction motors, and of the system with the flywheel activated

Even though the current reaching the batteries exceeded the desired 20 amps for the testing, significant reductions in magnitude of regenerative braking current at the battery was realized with the INSTAR system. Moreover, the energy used with the INSTAR system was significantly less then with a tradition hybrid vehicle. Figure 63 shows the current profiles of a vehicle which can absorb all of the regenerative braking energy, a vehicle equipped with INSTAR, and a tradition vehicle with a 25 amp maximum regenerative current (the maximum regeneration current the flywheel allowed to reach the battery).

Table 12 shows the energy usage of the road tests, and it is shown that though the INSTAR vehicle uses more energy than a vehicle which can absorb all of the regenerative braking energy, it uses less than a traditional hybrid vehicle with a 25 amp maximum regeneration limit. It is important to remember, that a vehicle which can absorb the entirety of the regenerative braking energy will either have a very large and expensive battery pack, or will absorb the energy at the risk of damaging the battery. It is important to note that the maximum vehicle speed during testing is only 25 km/hr, which is significantly slower than a vehicle might be travelling during a driving cycle. Increased speeds will see decreased energy usage relative to a traditional hybrid vehicle.

Table 12: Energy usage of road tests

Situation	Energy Consumed	Percent from Minimum Energy Usage	Energy Saved over Traditional Hybrid
All Regeneration captured with the batteries	37.0 kJ	Minimum Energy Usage	6.7 kJ
Flywheel used to recapture some of the regenerative energy	39.8 kJ	7.44%	3.9 kJ
Any current exceeding 25 amps is dissipated through the friction brakes	43.7 kJ	18.00%	Traditional Hybrid

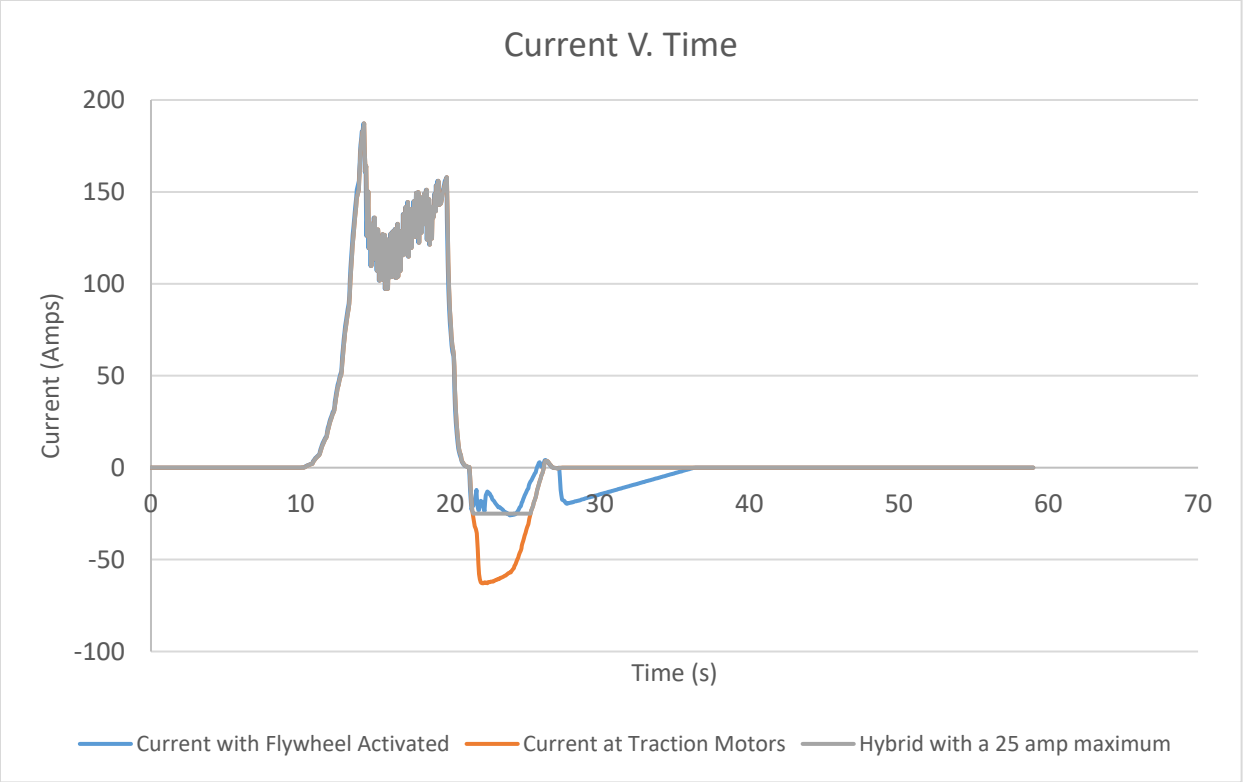

Figure 63: Comparison of current profiles of a fully battery vehicle, the vehicle equipped with INSTAR, and a traditional hybrid vehicle with a 25 amps maximum regeneration limit

Section 9.3 Flywheel Pre-charging

It was desired to lower the discharge current out of the batteries, as was done in the laboratory. The flywheel was pre-charged with a constant throttle signal of 100, resulting in a flywheel speed after pre-charging of around 9000 rpm. The energy from the flywheel could then be extracted using the flywheel brake signal algorithm shown in Equation 12. For the road testing, the flywheel pre-charging strategy was combined with the previous flywheel absorption strategy to attempt to lower battery discharge current, while also lowering battery charging current. The signals sent to the flywheel from the supervisory controller, along with the kart speed can be seen in Figure 64.

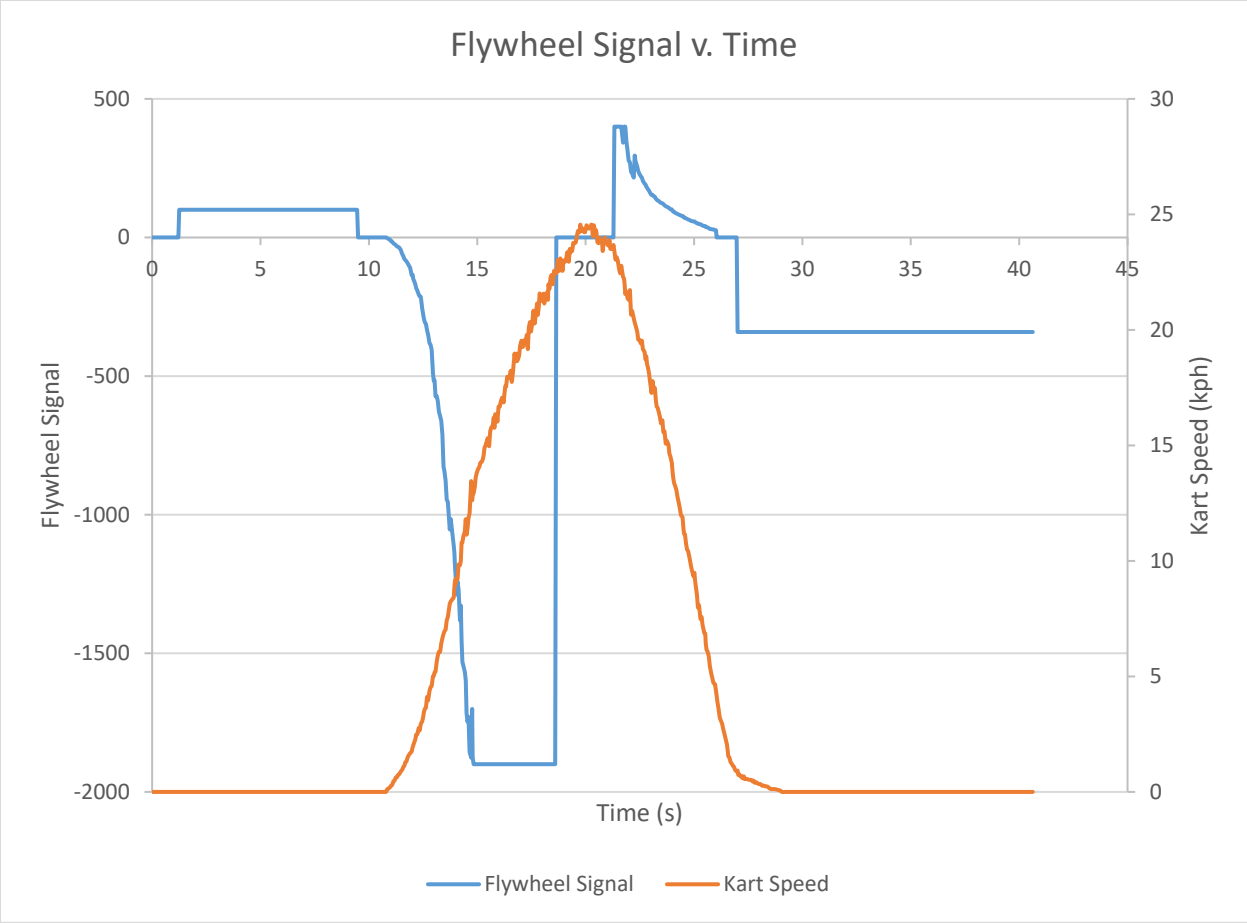

Figure 64: Flywheel signals v time, along with kart speed v. time. Flywheel signals greater than zero are throttle signals, and values less than zero are brake signals.

Using the flywheel pre-charging strategy, the discharge current out of the batteries was reduced from the case without the flywheel activated. Figure 65 shows how the maximum current out of the batteries was reduced from around 190 amps to 160 amps. Figure 66 shows the same currents but with a moving average line plotted for each with a period of 0.3 seconds to reduce the noise coming from the motor controller current readings. Though the pre-charging strategy was successful in reducing the magnitude of current coming out of the battery, the strategy also used more energy than the previous case where the flywheel was only used for regeneration.

Table 13 show the energy use of the kart during the pre-charge trials. The improvement over a traditional hybrid was only 1.152 kJ in the pre-charging case, where it was 3.907 kJ in previous trials where the flywheel was only used for regeneration. It is also important to note that the driving profile in this case is a simple acceleration and deceleration profile and results in a driving profile more representative of the full UDDS may be different. The lifetime benefits of reducing battery current levels would have to be compared against the added cost of the system to determine their worth for incorporation in a production vehicle.

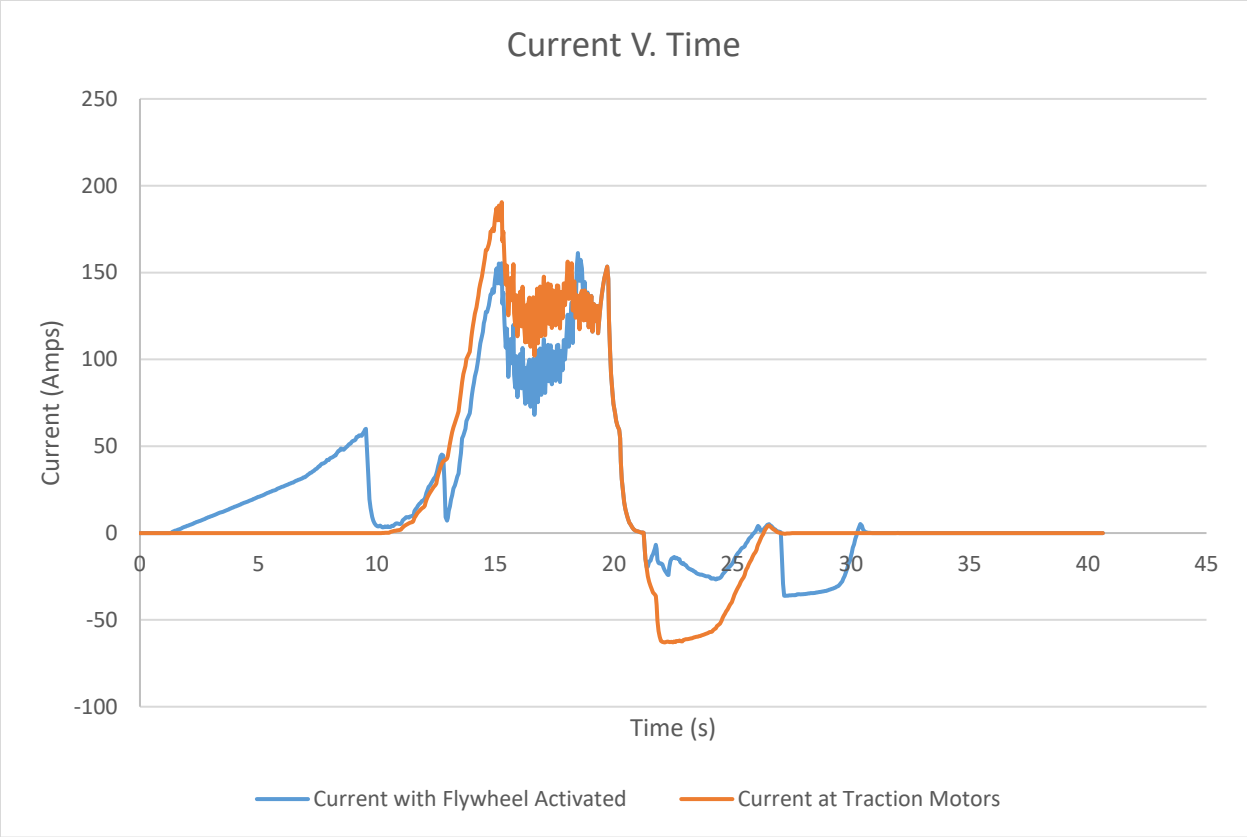

Figure 65: Traction motor currents and the sum of traction motor currents with flywheel current v. time.

Pre-charging of the INSTAR system could be considered worthwhile if the battery discharge currents could be reduced beyond what is shown in the testing here. Attempts were made to place more energy into the flywheel to further offset the discharge currents out of the battery, but the resulting voltage drop from the battery was too much for the hardware on the kart, and would trip fail safe measures on the motor controllers. Increasing the size of the testing platform batteries would allow for higher flywheel speeds to be tested, and this is left for future members of the lab.

Table 13: Energy use of the kart during trials with the flywheel activated for regeneration and pre-charging

Situation	Energy Consumed	Percent from Minimum Energy Usage	Energy Saved over Traditional Hybrid
All Regeneration captured with the batteries	37.1 kJ	Minimum Energy Usage	6.8 kJ
Flywheel used to recapture some of the regenerative energy	42.8 kJ	15.46%	1.1 kJ
Any current exceeding 25 amps is dissipated through the friction brakes	43.9 kJ	18.57%	Traditional Hybrid

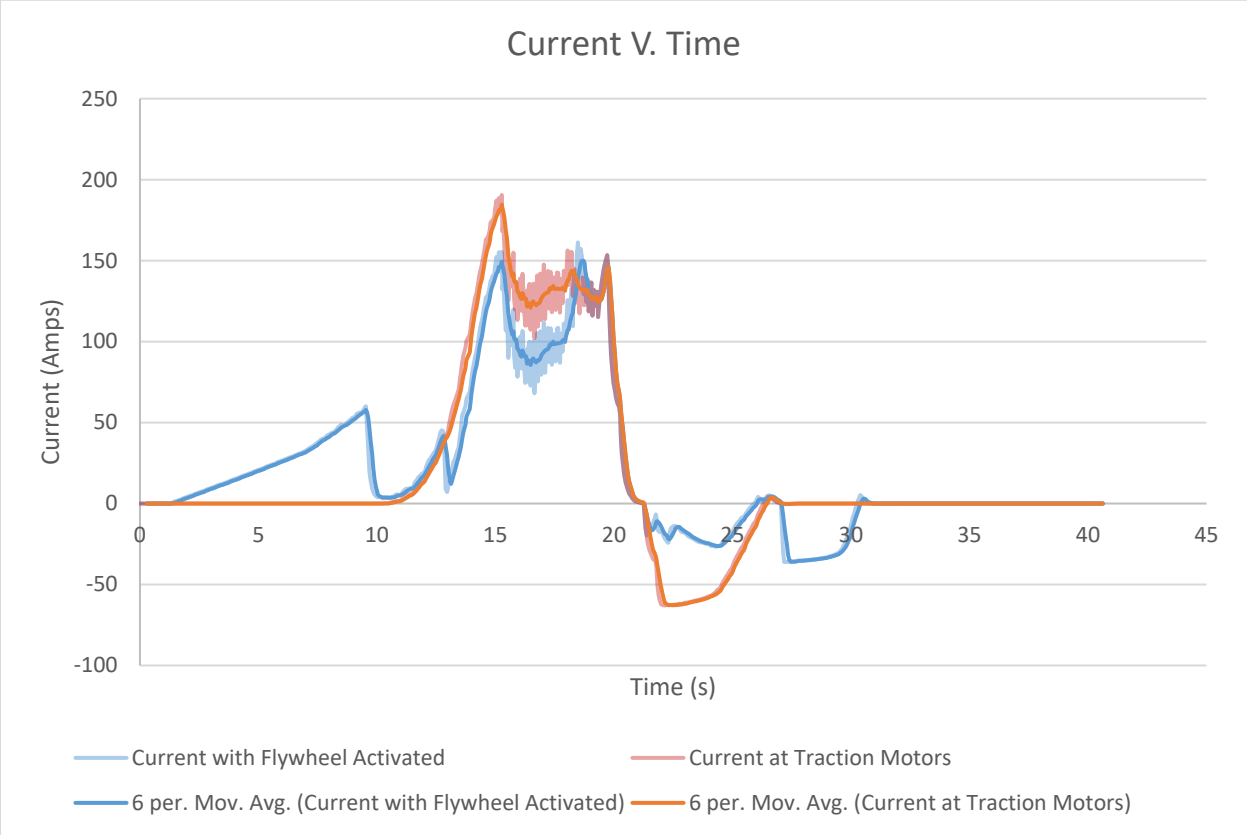

Figure 66: Traction motor current and the addition of traction motor and flywheel currents v time. The solid lines indicate a moving average with a period of 0.3 seconds

Section 9.4 Road Tests with User Input

All previous tests were performed with a preprogrammed driving profile. To determine how well the developed algorithms react to real world driving conditions, a driving circuit was established at the Richmond Field Station. The driving circuit can be seen in Figure 67, and consists of 6 straight segments with 6 stops. The total distance traveled as measure with Google Maps is 2750 feet, or about 0.52 miles. When driving the circuit, the driver drove similarly to how he would drive his personal vehicle. A plot of the vehicle speed over the driving course can be seen in Figure 68.

Figure 67: Driving circuit at the Richmond Field Station

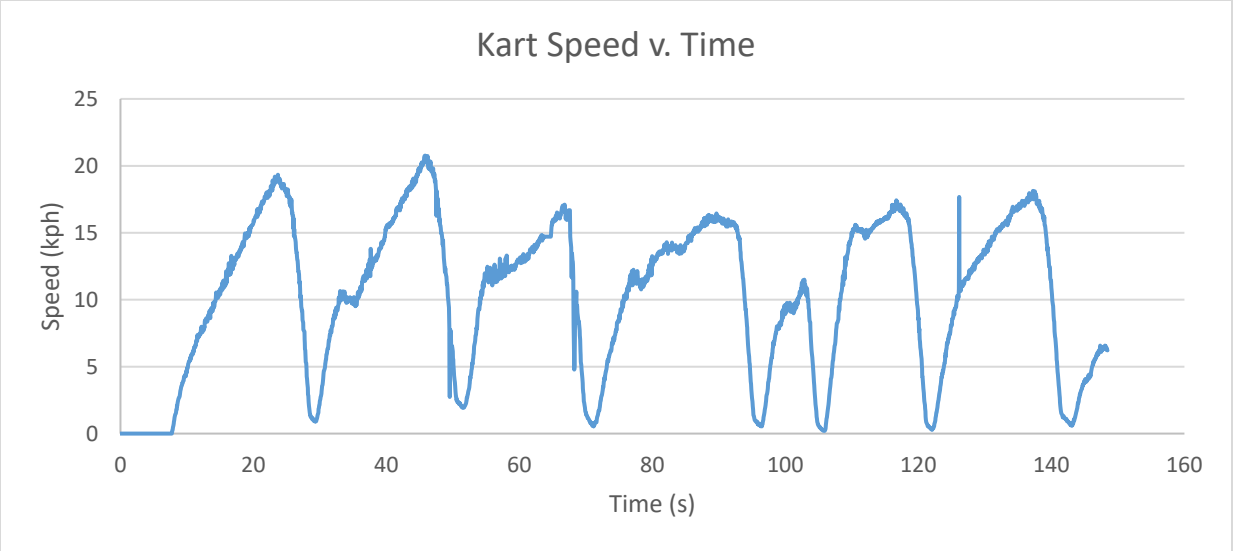

Figure 68: Kart speed v. time over the Richmond driving course

Figure 69 shows the currents over the driving cycle. The flywheel was largely successful in limiting the current reaching the batteries on the kart. The maximum regeneration current reaching the batteries was kept to 25 amps with the flywheel activated. However, the is room for improvement in the algorithms.

Table 14 shows the energy used by the kart over the driving profile with user inputs. While the flywheel successfully reduced the charging currents to the battery, the amount of energy required to propel the vehicle increased with the implementation of the flywheel. In order for the flywheel to be practical, the energy usage must not increase to more than a conventional hybrid vehicle, and should be improved over a hybrid vehicle. Further optimization of the flywheel algorithms would be necessary for practical implementation of the technology.

Table 14: Energy Usage during road testing with pedal inputs

Situation	Energy Consumed	Percent from Minimum Energy Usage	Energy Saved over Traditional Hybrid
All Regeneration captured with the batteries	202 kJ	Minimum Energy Usage	17 kJ
Flywheel used to recapture some of the regenerative energy	223 kJ	10.64%	-4 kJ
Any current exceeding 25 amps is dissipated through the friction brakes	219 kJ	8.37%	Traditional Hybrid

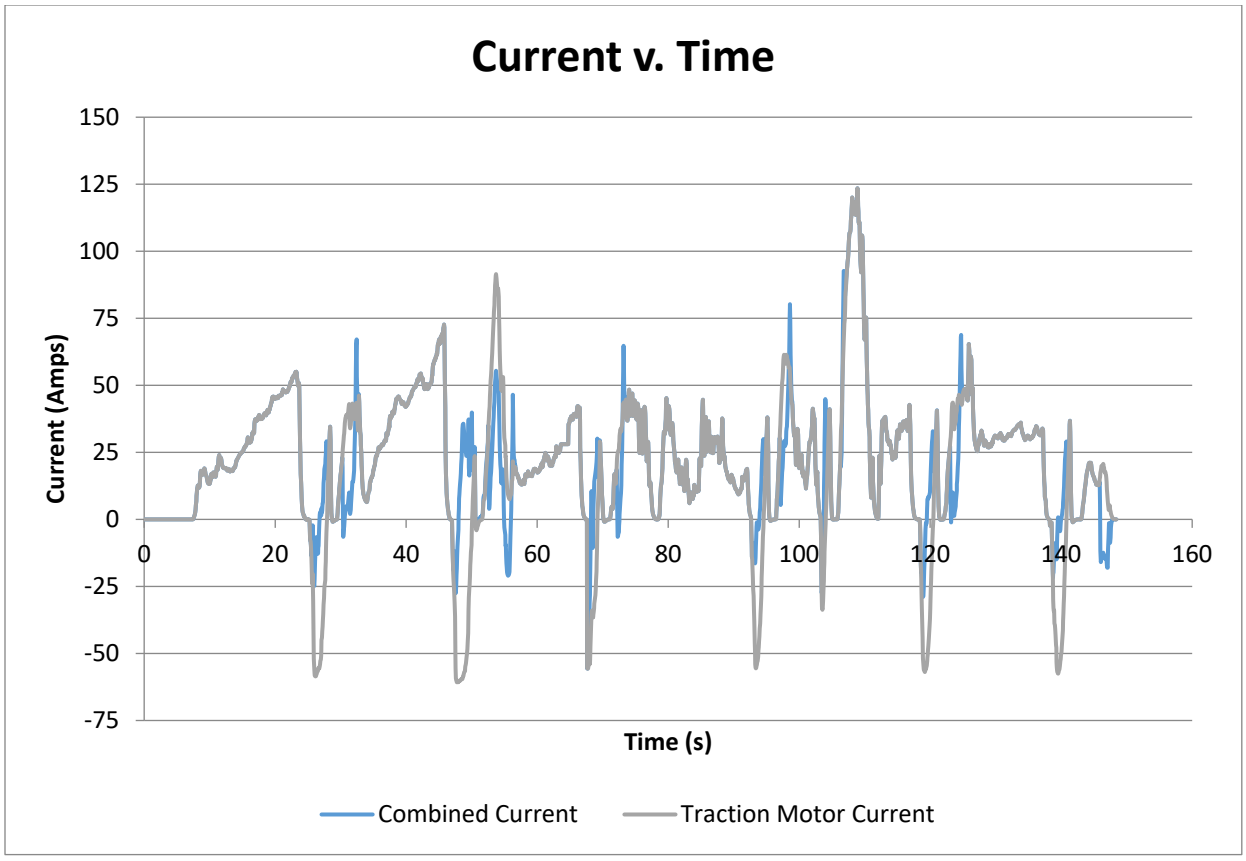

Figure 69: Battery and traction motor currents over the driving cycle

One reason the flywheel used more energy than was necessary in the road test with user input is that the flywheel algorithms overestimate the current generated by the traction motors. Figure 70 shows one braking and acceleration event during the road test. From time 45s to 50s the kart went through a braking event, indicated by the negative current at the batteries. However, the flywheel algorithm overestimated the current which would be sent to the batteries, and sent too high of a throttle signal to the flywheel motor controller. The result is that the flywheel demanded too much power for the regeneration event, and energy was pulled out of the batteries to accelerate the flywheel. To make the flywheel work correctly, a feedback loop to the control algorithm is likely necessary to adapt the algorithm output to each braking event.

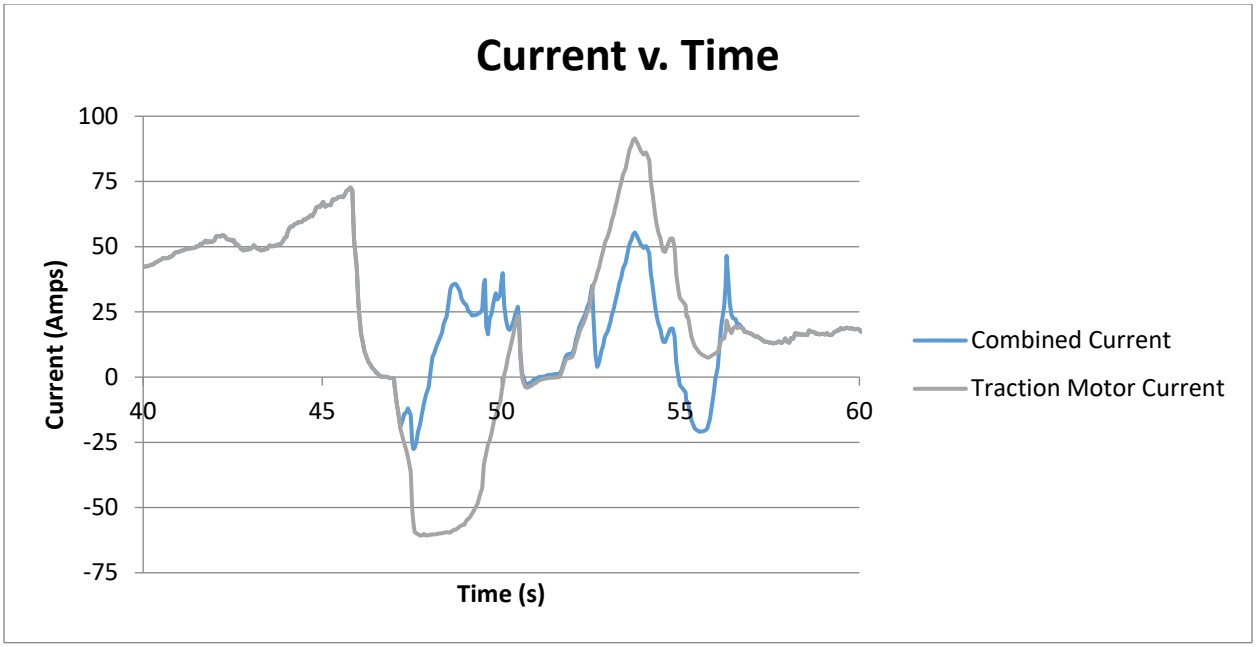

Figure 70: Current v. time for a single braking and acceleration event during the road tests with user inputs

Chapter IX Discussion

Section 9.01 Improvements in battery life and energy efficiency through regenerative braking

The INSTAR system has great potential to decrease the environmental impact of hybrid vehicles. The experiments have shown that the flywheel is capable of absorbing regenerative braking currents which may otherwise damage the batteries. In this study an open loop control algorithm was utilized to control the elctromechanical flywheel throttle signal. By modulating the throttle of the flywheel, some portion of regenerative braking currents were diverted from the batteries and sent to the flywheel. The open loop control algorithm was successful in reducing the regenerative braking peaks over 10 amps from 13 to 1 over the UDDS. From these results a reasonable conclusion can be that the flywheel was successful in increasing the battery life of the vehicle.

Modeling a vehicle composed of an ICE-battery combination plus a flywheel has shown that the flywheel can increase the efficiency of the vehicle. In a scenario where the flywheel absorbed excess currents from regenerative braking and returned them to the battery at a safe level, energy usage to complete the UDDS decreased by 46%. It must be noted that this decrease in energy usage compared a hybrid vehicle which only absorbed 1C of regenerative braking current to a vehicle equipped with a flywheel that can absorb nearly 80% of regenerative braking energy. Many vehicle manufacturers may absorb more than 1C of regenerative braking current, sacrificing some useable battery lifetime to gain energy efficiency.

Work in the lab shows promise for increased energy efficiency over a traditional hybrid vehicle. Lab trials had an energy efficiency between a hybrid vehicle with a 5-amp regeneration limit and a 10-amp regeneration limit. The aim of the experimental trial was to have an energy efficiency greater than the 10-amp regeneration limit case.

During single round trip road testing the INSTAR flywheel was able to demonstrate an increase in efficiency of 9% over a traditional hybrid vehicle while limiting the charging current at the battery to 25 amps. This test showed that the INSTAR flywheel or similar system can have applications in an electric vehicle to increase efficiency while increasing battery service life.

During full driving road tests, the INSTAR flywheel system used more energy than would have been used with a traditional hybrid vehicle, and also showed many areas where the control algorithms did not work correctly with the driving strategies of the driver. The road tests demonstrate the need for a closed loop control algorithm on the INSTAR system, and is an area of research which should be investigated by the INSTAR team.

Section 9.02 Improvements in energy efficiency through flywheel pre-charging

Over the driving cycle, the traction motor power demand varies greatly. Large power peaks in a traditional hybrid necessitate a power producing device which can meet the demand, a large electrochemical battery which can safely provide the power, or accelerated degradation of a smaller electrochemical battery. Through modelling it was shown that the use of an electromechanical flywheel can reduce the power peaks needed from the battery and ICE combination. Through pre-charging the flywheel, power peaks were reduced, and could be kept below a certain threshold.

The benefit of reducing and evening out the power peaks needed from the battery and ICE combination is that the power producing device can be redesigned to better meet the needs of the vehicle. If the power demand never goes beyond a certain value, then the ICE can decrease in output, possibly saving in size, weight, and cost of the ICE. The function of the ICE also changes from a power source to complete the driving cycle to a generator which supplies the energy needed to complete the driving cycle. The flywheel, and to a small extent the battery, take over the role of providing the power necessary to complete the driving cycle. Operating as a generator, the ICE can be redesigned to operate in a narrow, but more efficient power output range.

The ability to pre-charge the flywheel was demonstrated in the laboratory. The goal of the laboratory experiments was to show that the flywheel is capable of reducing the discharge peaks from the battery, and not to maximize the efficiency of the acceleration event. The laboratory experiment was successful in limiting battery discharge current to an upper threshold. More work is needed to create a control algorithm which can more evenly discharge energy from the flywheel to keep power demand from the battery more constant.

During road testing the energy used by the INSTAR system with flywheel pre-charging was 2.62% less than the energy which would be used by a traditional hybrid vehicle. During this test the discharge current peak out of the battery was also reduced, indicating that the total load coming out of the engine/battery combination on a hybrid vehicle was reduced. This application should be investigated further as it shows potential for reducing the size of the generator used on hybrid electric vehicles.

Section 9.03 Potential uses for the INSTAR system

The INSTAR system has the potential to be used in many electrified vehicles, including passenger cars. The most logical place to place the INSTAR system is in hybrid vehicles where the battery is small. In these vehicles, much of the regenerative energy must be dissipated through the friction brakes, because of the low C-rate of the battery. The INSTAR system would allow for more of the regenerative braking energy to be captured and to increase the overall efficiency of the vehicle. As shown in the pre-charging experiments, the INSTAR system also has the ability to lower the power demand from the battery and ICE during acceleration. In hybrid vehicles where the battery is small this becomes important because the battery will be unable to supply large

amounts of power to the drive train, and the ICE must be used to provide the power to the wheels for acceleration. If the INSTAR system were used, the power supply from the ICE could be augmented by the flywheel, lowering the demand from the ICE and increasing vehicle efficiency.

The INSTAR system also has applications in trucking; especially in start/stop applications. Many manufacturers are looking at electrification of the vehicles. Because of the large mass of commercial trucks, large and expensive battery packs must be used if all the regenerative braking energy is to be captured. The INSTAR system can be an appropriate solution for reducing the size of the battery pack necessary to capture all of the regenerative braking energy, and to lower the cost of the system. Unlike batteries, where the cost scales linearly with capacity, the cost of a flywheel will not change much with increasing capacity. The INSTAR system can be used in conjunction with the vehicle battery and ICE to lower the cost of a hybrid truck power system.

The age of autonomous vehicles is rapidly approaching. Many companies are investing heavily in autonomous vehicle technologies, and are developing passenger cars with semi-autonomous technologies. General Motors has stated that they are working to produce an autonomous vehicle to be used on US highways by 2019 [29]. Autonomous vehicles present a great opportunity for the INSTAR technology. If the power demand is known ahead of time, the unpredictability of the driving cycle disappears, and power placement into the flywheel can be planned to optimize efficiency. In this case, the flywheel can supply the majority of power to the drive wheels, and the ICE becomes solely an on-board generator, where a much lower power output is required. Moving toward a power system with dedicated components for energy storage, energy generation, and power supply opens the system design up for a larger variety of energy generating units. For example, fuel cells which have been prohibitively expensive due to the size needed to supply power to the drivetrain, become a viable option for vehicles. The concept of such a power scheme incorporating a fuel cell, battery and high-power device is not new, and has been proposed in existing publications [30, 31, 32].

An ideal use case for the INSTAR system could be small to medium size urban delivery and ride sharing vehicles. These vehicles must operate nearly 24 hours a day, and breaks are not regularly scheduled. Such vehicles have frequent starts and stops, and the average horsepower needed from the generator is likely small from the combination of generally low speeds and start and stop driving. The INSTAR system would be highly advantageous to this type of driving profile. Furthermore, these types of vehicles would need to operate nearly 24 hours a day. Because of this, full electric vehicles are not the best option because of the need for them to charge for long periods of time. Hybrid vehicles offer a solution which can run nearly 24 hours a day with little or no downtime. The INSTAR system can allow for smaller, more efficient generators to be used, and smaller, less expensive batteries which will last longer because less power will be placed through them.

Chapter X Conclusion

The INSTAR system shows that it is possible to create a vehicle with a dedicated high-power device and a battery to limit the charge and discharge currents from the batteries. Research conducted by others has shown that reducing these currents can extend battery service life. Some combination of regenerative braking and pre-charging of the flywheel could allow for a reduction of generator size while still maintaining system efficiency. The system as implemented in this paper should have an updated control system created to increase efficiency.

Flywheels are useful in vehicles because of their inexpensive price tag. The downside to using them is the parasitic losses associated with them. To reduce the parasitic losses, more expensive features such as vacuum and magnetic levitating bearings must be added. These expensive features reduce the attractiveness of flywheels for energy storage. As the cost of ultracapacitors decreases, the cost/benefit tradeoff of ultracapacitors might outweigh the flywheel. However, the work here may be related to any dedicated high-power unit, and the concepts are not specific to an electromechanical flywheel.

This work has shown that there is potential for such a system to be implemented in a hybrid vehicle to increase battery service life, and increase efficiency over a hybrid vehicle with a 1 C-rate cap on regeneration current. This work has also shown that a low cost and low-tech electromechanical flywheel is capable of delivering these improvements. Additional work on the flywheel control algorithms are necessary for commercial implementation, and should be an area of continued study.

References

[1] U.S. Environmental Protection Agency, "Inventory or U.S. Greenhouse Gas Emissions and Sinks," U.S. Environmental protection Agency, Washington, DC, 2016.

[2] Center for Climate and Energy Solutions, "Reducing Greenhouse Gas Emmission from U.S. Transportation," Pew Center on Global Climate Change, ARLINGTON, 2011.

[3] US Department of Transportation, National Highway Traffic Safety Administration, "2017 and Later Model Year Light-Duty Vehicle Greenhouse Gas Emissions and Corporate Average Fuel Economy Standards; Final Rule," United States Environment Protection Agency, Washington, DC, 2012.

[4] Z. Zou, J. Cao, B. Cao and W. Chen, "Evaluation Stategy of Regenerative Braking Energy for Supercapacitor Vehicle," *ISA Transactions,* vol. 55, pp. 234-240, 2015.

[5] L. Tang, G. Rizzoni and A. Cordoba-Arenas, "Battery Life Extending Charging Stategy for Plug-in Hybrid Electric Vehicles and battery Electric Vehicles," *IFAC-PapersOnLine,* vol. 49, no. 11, pp. 070-076, 2016.

[6] S. S. Choi and H. S. Lim, "Factors that affect cycle-life and possible degradation mechanisms of a Li-ion cell based on LiCoO2," *Journal of Power Sources,* vol. 111, pp. 130-136, 2002.

[7] G. Ning, B. Haran and B. N. Popov, "Capacity fade study of lithium-ion batteries cycled at high discharge rates," *Journal of Power Sources,* vol. 117, pp. 160-169, 2003.

[8] J. Shim, R. Kostecki, T. Richardson, X. Song and K. A. Striebel, "Electrochemical analysis for cycle performance and capacity fading of a lithium-ion battery cycled at elevated temperature," *Journal of Power Sources,* vol. 112, pp. 222-230, 2002.

[9] K. J. Kelly and A. Rajagopalan, "Benchmarking of OEM Hybrid Electric Vehicles at NREL," National Renewable Energy Laboratory, Boulder, CO, 2001.

[10] L. Gao and Z. C. Winfield, "Life Cycle Assessmen of Environmental and Economic Impacts of Advanced Vehicles," *Energies,* vol. 5, pp. 605-620, 2012.

[11] Oak Ridge National Laboratory, "An Assessment of Flywheel High Power Energy Storage Technology for Hybrid Vehicles," Oak Ridge, Tennessee, 2011.

[12] S. R. Holm, H. Polinder, J. A. Ferreira, P. van Gelder and R. Dill, "A Comparison of Energy Storage Technologies as Energy Buffer in Renewable Energy Sources with Respect to Power Capability".

[13] Z. Filipi, "Hydraulic and pneumatic hybrid powertrains for improved fuel economy in vehicles," in *Alternative Fuels and Advanced Vehicle Technologies for Improved Environmental Performance*, Cambridge, Woodhead Publishing, 2014, pp. 505-540.

[14] P. Paddu and M. Paderi, "Hydro-pneumatic accumulators for vehicles kinetic energy storage: influences of gas compressability and thermal losses on energy storage capability," *Energy,* vol. 57, pp. 326-335, 2013.

[15] P. Tawadros and N. Zhang, "Integration and performance of regenerative braking and energy recovery technologies in vehicles," in *Alternative Fuels and Advanced Vehicle Technologies for Improved Environmental Performance*, Cambridge, Woodhead Publishing, 2014, pp. 541-563.

[16] S. Hui, Y. Lifu and J. Junqing, "Hydraulic/electric synergy system (HESS) design for heavy hybrid vehicles," *Energy,* vol. 35, pp. 5328-5335, 2010.

[17] M. Ortúzar, J. Moreno and J. Dixon , "Ultracapacitor-Based Auxiliary Energy System for an Electric Vehicle: Implementation and Evaluation," *IEEE TRANSACTIONS ON INDUSTRIAL ELECTRONICS,* vol. 54, no. 4, pp. 2147-2156, 2007.

[18] R. M. Schupbach, J. C. Balda, M. Zolot and B. Kramer, "Design Methodology of a Combined Battery-Ultracapacitor Energy Storage Unit for Vehicle Power Management," in *Power Electronics Specialist Conference*, Acapulco, Mexico, 2003.

[19] K. R. Pullen and A. Dhand, "Mechanical and Electrical Technology to Store Energy in Vehicles," in *Alternative Fuels and Advanced Vehicle Technologies for Improved Environmental Performance*, Cambridge, Woodhead Publishing, 2014, pp. 476-504.

[20] R. T. Douchette and M. D. McCulloch, "A Comparison of High-speed Flywheels, Batteries, and Ultracapacitors on the bases of cost and fuel economy as the energy storage system in a fuel cell based hybrid electric vehicle," *Journal of Power Sources,* vol. 196, pp. 1163-1170, 2011.

[21] C. S. Hearn, M. M. Flynn, M. C. Lewis, R. C. Thompson, B. T. Murphy and R. G. Longoria, "Low Cost Flywheel Energy Storage for a Fuel Cell Powered Transit Bus," in *Vehicle Power and Propulsion Conference*, Arlington, 2007.

[22] D. R. Talancón, "Design, Fabrication, and Testing of the INSTAR [INertial STorage And Recovery] System," University of California, Berkeley, Berkeley, 2015.

[23] United States EPA, "Dynomometer Drive Schedules," [Online]. Available: https://www.epa.gov/vehicle-and-fuel-emissions-testing/dynamometer-drive-schedules. [Accessed 21 November 2018].

[24] Toyota, "2014 Prius Product Information," 2014.

[25] D. SHERMAN, "Drag Queens, Aerodynamics Compared," Car and Driver, June 2014. [Online]. Available: https://www.caranddriver.com/features/drag-queens-aerodynamics-compared-comparison-test-second-place-toyota-prius-page-5. [Accessed 8 October 2017].

[26] K. Holmberg, P. Andersson and A. Erdemir, "Global energy consumption due to friction in passenger cars," *Tribology International,* vol. 47, pp. 221-234, 2012.

[27] Toyota, "2017 Prius product Information," 2017.

[28] Briggs and Stratton Racing, [Online]. Available: http://www.briggsracing.com/racing-engines/world-formula. [Accessed 15 1 2018].

[29] P. LeBeau, "GM is seeking approval for an autonomous car that has no steering wheel or pedals," CNBC, 12 January 2018. [Online]. Available: https://www.cnbc.com/2018/01/12/gm-is-seeking-approval-for-an-autonomous-car-that-has-no-steering-wheel-or-pedals.html. [Accessed 26 January 2018].

[30] A. L. Dicks and D. A. J. Rand, Fuel Cell Systems Explained, Hoboken, NJ: John Wiley & Sons Ltd, 2018.

[31] P. Thounthong, S. Raël and B. Davat, "Energy Management of fuel cell/bettery/supercapacitor hybrid power source for vehicle applications," *Journal of Power Sources,* vol. 193, no. 1, pp. 376-385, 2009.

[32] P. Rodatz, G. Paganelli, A. Sciarretta and L. Guzzella, "Optimal Power Management of an Experimental fuel cell/supercapacitor-powered hybrid vehicle," *Control Engineering Practice,* vol. 13, no. 1, pp. 41-5, 2005.

[33] ASM International Handbook Committee, ASM Handbook, Volume 01- Properties and Selection: Irons, Steels, and High-performance Alloys, ASM International, 1990.

[34] Motion Industries, "Electric Discharge Machining and how it affects Bearings," [Online]. Available: https://www.motionindustries.com/knowledgelinks/bearings/resource.jsp/Electric%20Discharge%20Machining%20Damage%20and%20How%20it%20Affects%20Bearings?slug=common-mode-bearing-currents. [Accessed 31 January 2018].

[35] J. Zhao and M. Xu, "Fuel economy optimization of an Atkinson cycle engine using genetic algorithm," *Applied Energy,* vol. 105, pp. 335-348, 2013.

Appendix A: Open Loop Control Algorithm Derivation

The open loop control algorithm used to accelerate the flywheel during regenerative braking was created by previous students working in the INSTAR lab. The derivation of the control algorithm is reproduced from the dissertation of Daniel Talancon.

The numerator of the control algorithm designed to predict the current produced during regenerative braking by the traction motors, and is $A(T_A * \omega_V) - BT_A + C\omega_V$. The first term of the numerator is intended to predict the current generated by the wheels as a function of torque input, and current wheel speed. The derivation of the current starts with the change in kinetic energy of the wheels and is shown below.

$$E = \frac{1}{2} J * \omega^2$$

$$Power = \frac{dE}{dt} = J * \omega * \frac{d\omega}{dt} = J * \omega * \alpha$$

$$Torque = J * \alpha$$

$$Power = \omega * Torque$$

$$Power = I * V$$

$$\therefore \omega * Torque = I * V$$

$$\therefore I = I_{rotational} = \frac{\omega * Torque}{V}$$

Substituting $A = \frac{1}{V}$

$$I_{rotational} = A * (\omega * Torque)$$

This is the first term of the numerator, and predicts the current produced from the torque signals sent to the traction motors based on the change in kinetic energy of the steel discs of the testing apparatus. In theory, the constant A should be known if the battery voltage is known, however, in practice it was found that varying this parameter was necessary to create a well-functioning algorithm. The second term in the numerator considers the current lost due to the resistive losses of the motor. The derivation of the term is shown below.

$$I_{torque} = \frac{Torque\ Requested}{K_t}$$

Where K_t is the torque constant of the motor and has units of $\left[\frac{N*m}{Amp}\right]$

$$P_{resistive} = I_{torque}^2 * R$$

$$P_{resistive} = \left(\frac{Torque\ Requested}{K_t}\right)^2 * R$$

The relationship above shows that the power dissipated, and thus the current, is proportional to the square of the requested torque, in practice a simple relationship was sufficient for this term, as it is much smaller than the first term of the numerator.

$$\therefore I_{torque} = -B * Torque\ Requested$$

The last term of the numerator is associated with the efficiency losses of the traction motor. The efficiency of the traction motors on the testing apparatus were found to be approximated by a simple linear relationship with wheel speed. Thus, the third term is shown below.

$$I_{efficiency\ loss} = C * \omega_{wheel}$$

Combining each of these terms fives the numerator of the control algorithm

$$I_{vehicle,regne} = I_{rotational} + I_{torque} + I_{efficiency\ loss}$$

$$I_{vehicle,regen} = A * \left(Torque_{Brake,Requested} * \omega_{wheel}\right) - B * Torque_{Brake,Requested} + C * \omega_{wheel}$$

The denominator of the algorithm predicts the current absorbed by the flywheel. Because the flywheel is essentially just another motor with a mass just like the traction motors, the same relationship can be used with new values.

$$I_{vehicle,regne} = I_{rotational} + I_{torque} + I_{efficiency\ loss}$$

The $I_{rotational}$ in this case is the power dissipated from regenerative braking, and is linear with both torque and wheel speed. But in this situation, it is the acceleration torque greater than the braking torque.

$$I_{roational} = D * (\omega * Torque)$$

The second contribution, I_{torque} , is from the current required to generate the acceleration torque. The derivation is the same as with the traction motors and is shown below.

$$I_{torque} = \frac{Torque\ Requested}{K_t}$$

Substituting $E = \frac{1}{K_t}$

$$I_{torque} = E * Torque\ Requested$$

The third term associated with efficiency was left out for the flywheel current model. This is because testing shows that the efficiency of the flywheel was constant at operating conditions, and did not need to be included in the algorithm. Combining the two relevant terms, the current absorbed by the flywheel can be modeled by the below equations.

$$I_{Flywheel,Absorbed} = I_{rotational} + I_{torque}$$

$$I_{Flywheel,Absorbed} = D * \left(Torque_{flywheel} * \omega_{flywheel}\right) + E * Torque_{flywheel}$$

To construct the algorithm, the assumption is that all of the braking current was desired to be absorbed by the flywheel, and the following relationship holds true.

$$I_{Vehicle,Regen} = I_{Flywheel,Absorbed}$$

Substituting in the relationships reached before, we have the following relationship.

$$A * \left(Torque_{Brake,Requested} * \omega_{wheel}\right) - B * Torque_{Brake,Requested} + C * \omega_{wheel} = D * \left(Torque_{flywheel} * \omega_{flywheel}\right) + E * Torque_{flywheel}$$

The algorithm's goal is to predict what torque signal to send to the dedicated flywheel controller. So, to create the algorithm, we solve for the flywheel torque. The rearranged equation is shown below.

$$Torque_{flywheel} = \frac{A * \left(Torque_{Brake,Requested} * \omega_{wheel}\right) - B * Torque_{Brake,Requested} + C * \omega_{wheel}}{D * \omega_{flywheel} + E}$$

During practice, it was observed that adding a term in front to scale output of the above equation into the correct range to be read by the motor controller was a convenient. And thus, the final form of the algorithm is shown below.

$$Flywheel\ Throttle\ Signal = Torque_{flywheel} = F\left[\frac{A(T_{Brake} * \omega_{Vehicle}) - BT_{Brake} - C\omega_{Vehicle}}{\left(D * \omega_{flywheel} + E\right)}\right]$$

A similar open loop controller was needed to produce the braking signals at the flywheel during the pre-charging experiments. This algorithm is new to this study and needed to be created. The same theory and process was used to create the open loop control algorithm used to brake the flywheel during acceleration events for the pre-charging experiments. But, because the current was flowing in the other direction, from the flywheel to the motors, the signs of the algorithm needed to be adjusted, and instead of braking torques from the traction motors, acceleration torques needed to be used. In this case, the current required by the traction motors is shown below.

$$I_{vehicle,accel} = A * \left(Torque_{Accel,Requested} * \omega_{wheel}\right) + B * Torque_{Accel,Requested} - C * \omega_{wheel}$$

At the flywheel side of the equation, instead of a throttle signal, a braking signal is the desired result. So instead of the current absorbed by the flywheel, the current dissipated from the flywheel must be calculated. This is essentially the same as the current absorbed, however instead of adding the power lost due to resistive losses, it must be subtracted. The relationship is reproduced below.

$$I_{Flywheel,dissipated} = I_{rotational} - I_{torque}$$

Setting the currents equal to each other as done before with the flywheel throttle algorithm produces a similar result, with the appropriate sign convention and torque parameters.

$$Flywheel\ Brake\ Signal = Torque_{flywheel} = F\left[\frac{A(T_{Accel} * \omega_{Vehicle}) + BT_{Accel} - C\omega_{Vehicle}}{\left(D * \omega_{flywheel} - E\right)}\right]$$

Appendix B: Analysis of premature bearing failure

During experimental trials premature bearing failure was observed. The bearing would operate as normal for several tests then, suddenly, more than an acceptable level of noise was generated by the rotating bearings. The noise from the bearings was likened to a rough rolling surface rather than a smooth one. The bearings were changed each time, but after the third set of bearings was installed, an investigation was launched into the cause of the failure. This appendix describes the investigation of the bearing failure.

Initial visual investigation

Upon initial visual inspection, it is clear that there is some wear occurring in the bearings. The oil from the system contains fine particulate matter (Figure 71). The matter is dark brown in color, and is not magnetic. The bearings appear to show little signs of wear from the outside. There are no signs of discoloration on the outside of the bearing races on the bottom bearing (Figure 72 a). On the top bearing, the outer race chows no sign of discoloration. The inner race shows a small area of corrosion where it meets the spindle (Figure 72 b). This area of corrosion is unlikely to contribute to the particulate matter in the oil, as there would be nothing to force the removal of these corrosion products off the bearing race. No signs of wear or corrosion were present on the spindle of the flywheel.

Figure 71: Image showing fine particulate matter in the oil reservoir of the flywheel

(a) (b)

Figure 72: Bearings: bottom (a) and top (b)

Inspection of inner races and balls

Two diametrically opposite cuts were made in the bearing with an abrasive wheel to gain access to the inside of the bearing (Figure 73). Great care was taken to ensure no bearing movement during the cutting process to not unintentionally damage the rolling surfaces of the bearing. The bearing was cooled with water during the cutting process to avoid heating the bearing. The bearings in question had been used for less than 2 hours, and being so, the wear makes were only barely visible on the inside of the bearing races.

Figure 73: Bearing cut to gain access to races and bearings

Figure 74: View of inner races of bottom bearing. (a) Inner race (b) ball (c) outer race.

Figure 74 shows photographs of the races of the bottom bearings as well as a ball from the bottom bearing. The bearing shows sign of axial wear, indicated by wear marking which are off centered in the bearing races. No excessive signs of wear are obvious from the initial inspection. Figure 75 shows the races of the top bearing as well as the balls in their cage. Again, now excessive signs of wear are visible on the races or balls. The top bearing is lacking the axial wear marks of the bottom bearing, indicating that the bottom bearing is taking the majority of the axial load of the flywheel rotor.

Figure 75: View of races of top bearing. (a) Inner race (b) ball (c) outer race.

Optical microscope images of bearing surfaces

A USB powered optical microscope was used to more closely inspect the elements of the bearing. Because of the curved and shiny surfaces of the races and bearing elements, it was difficult to capture images using an optical microscope. Figure 76 show images of the outer races of the bottom and top bearings respectively. In the images, the wear marks from the balls are clearly visible, as are some surface markings just outside the wear bands. These imperfections are estimated to be about 0.1 mm in feature size, and exist just outside of the wear bands.

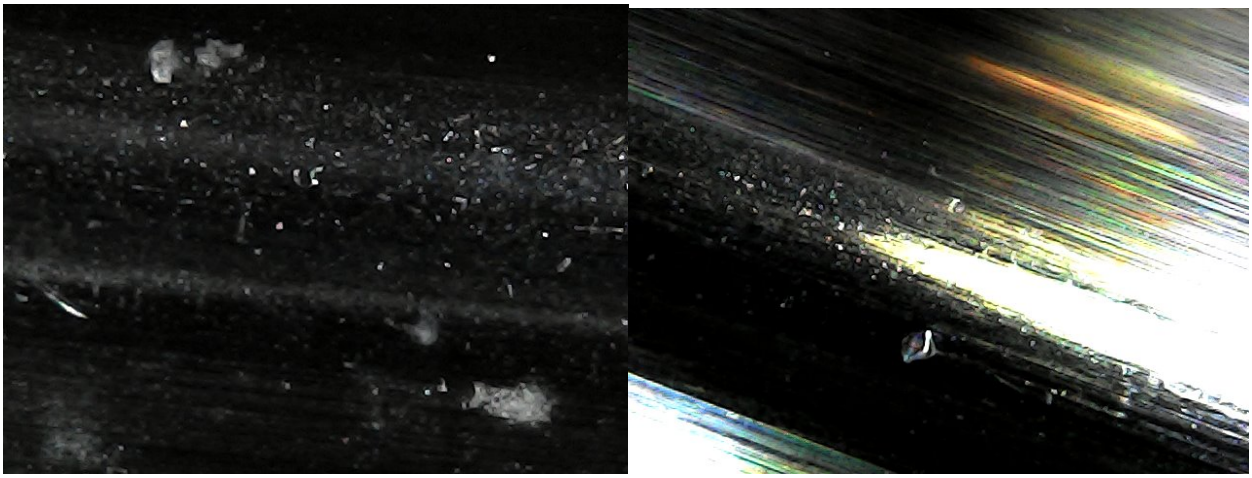

(a) (b)

Figure 76: Images taken with optical microscope of outer race of the bottom bearing (a), and top bearing (b)

Figure 77 shows images of a ball from the bottom ball bearing. Dimpling and pitting of the surface of the ball can be observed in both images. The pits appear to be narrow and deep, and some have raised surfaces surrounding them. Pitting corrosion in stainless steels has been observed to create similar structures, however, the primary corrosion agent for pitting corrosion is chloride ions, typically found in marine environments [33]. The lack of chloride ions in the bearing environment here means that pitting corrosion is unlikely.

The pitting observed on the balls of the bearing as well as the raceways closely resembles electrical pitting (Figure 78). Electrical corrosion commonly occurs in electric motors where the ungrounded shaft develops a charge, which travels through the shaft bearings to the motor housing [34]. The pitting is caused by electrical arcs crossing between the rolling elements and the bearing races, and is a form of Electric Discharge Machining [34]. The pits formed by electrical corrosion are typically 0.1mm to 0.3mm in diameter, consistent with the size of the features observed on the experimental bearings. The lubricant in such electrical corrosion cases is typically darkened in color from the oxides produced from the corrosion process, as well as particles of burned lubricant. The lubricant observed with the experimental flywheel is darkened, consistent with electrical corrosion.

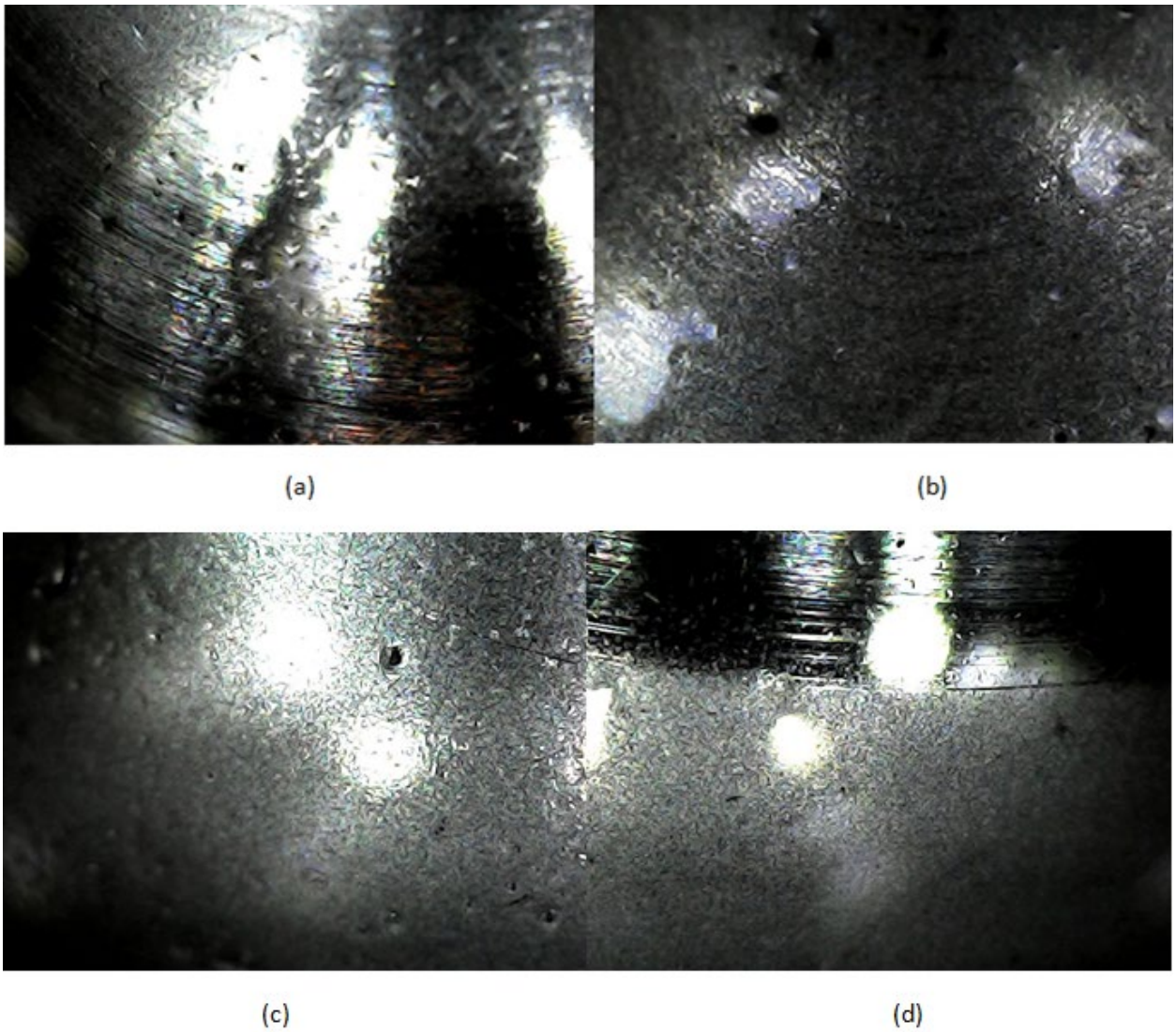

Figure 77: Images of a bearing ball from the bottom bearing using an optical microscope. (a) Image showing dimpling and pitting of the surface (b) magnified image of the ball showing pits (c) additional photo of magnified ball pitting (d) image showing area where wear band meets the unworn surface.

Figure 78: Electrical pitting corrosion on the race of a ball bearing. [34]

Conclusion of bearing investigation

The premature failure of the spindle bearings in the flywheel was investigated through visual analysis of the bearings. The bearings were sectioned to access the races of the bearings as well as the balls. Pitting corrosion was visible on the races, as well as the balls. The pitting corrosion resembles pitting found on ball bearings suffering from electrical corrosion. Because of the application and symptoms, this is likely the cause of the bearing failure. To remedy the situation, the spindle of the flywheel should be grounded to provide an alternative pathway for spindle electrical currents.

Appendix C: Solution to Bearing Electrical Corrosion

To provide an alternate pathway for the spindle currents the spindle was grounded through the top of the shaft. A 303 stainless steel nub was machined and pressed into the center drilled hole at the top of the spindle (Figure 79). A carbon motor brush (Figure 80) was brought into contact with the stainless steel nub to conduct electricity away from the spindle. Contact was made between the motor brush and the flywheel housing such that there would be zero electrical potential between the motor housing and flywheel spindle (Figure 81). At the time of this publication, no signs of corrosion in the oil or unusual sounds indicating corrosion on the bearings have been observed.

Figure 79: Stainless steel nub on top of flywheel spindle

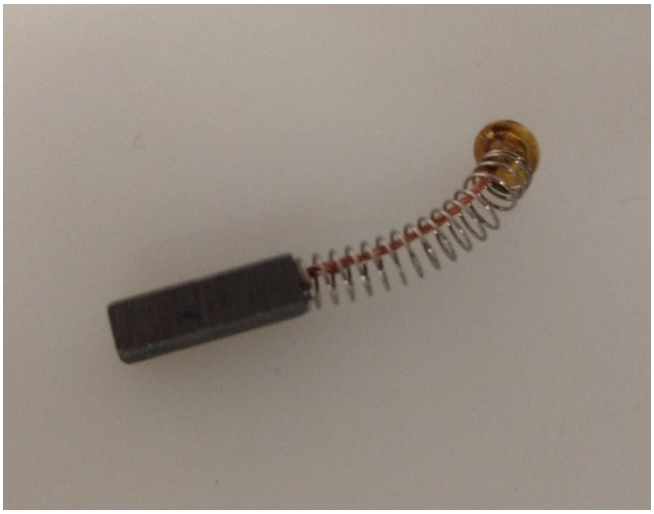

Figure 80: Motor brush contacting stainless steel numb on flywheel spindle

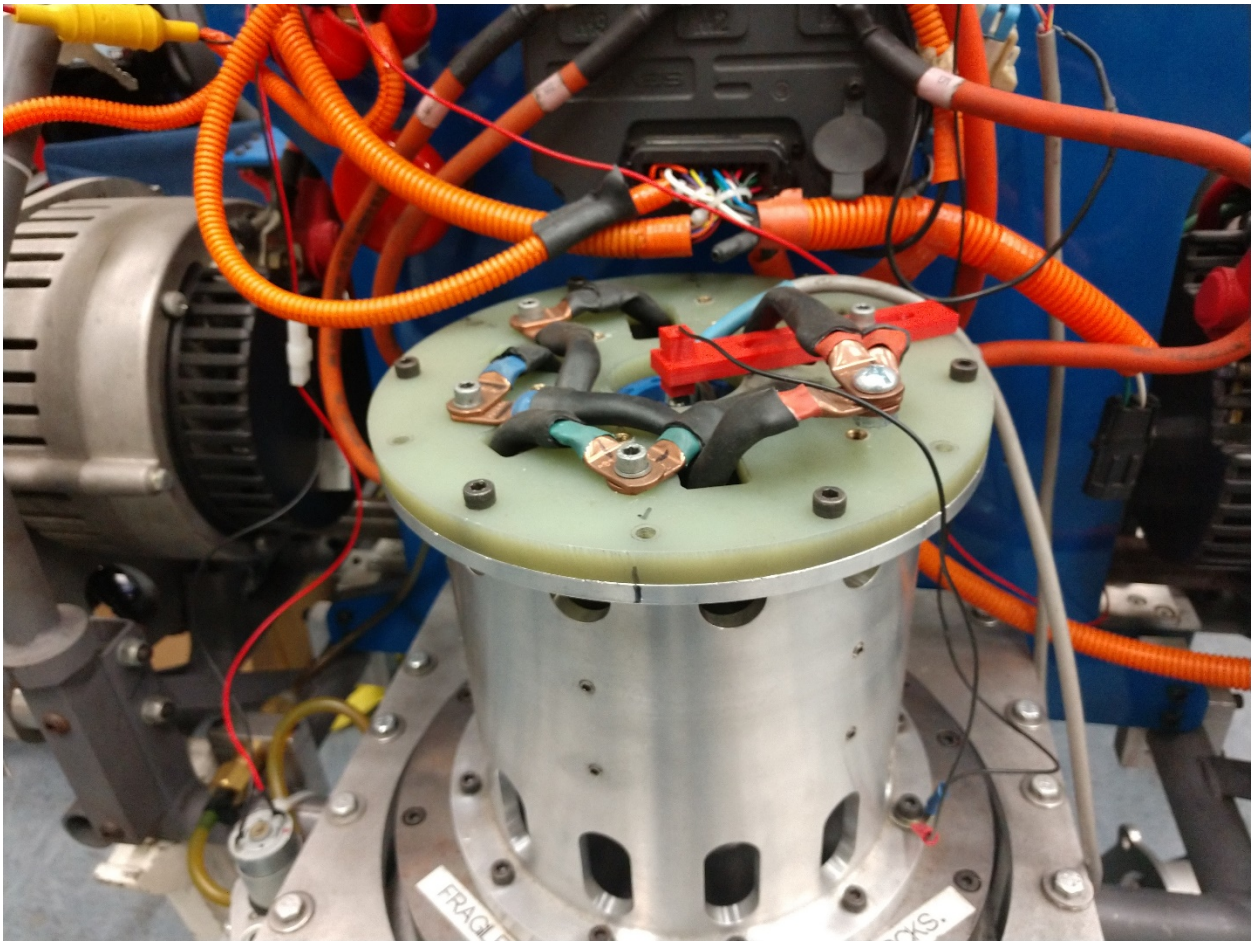

Figure 81: Motor brush holder (red) and grounding wire ensuring zero voltage potential between motor housing and spindle

Appendix D: LabView Code

The code implemented on the INSAR kart is comprised of 2 LabVIEW files. One is a real time program which runs on the dedicated windows computer assigned to the kart. The other program is a FPGA program which runs on the cRio device on the kart. The connection between the two programs is made via wireless connection through a wireless internet router. The purpose of the real time program running on the windows computer is to provide a readout to the operator of the kart, and to allow for the ability to control the kart with user input controls. The real time program also allows the user to import driving profiles to the FPGA code so that a standardized driving profile can be used for all driving tests.

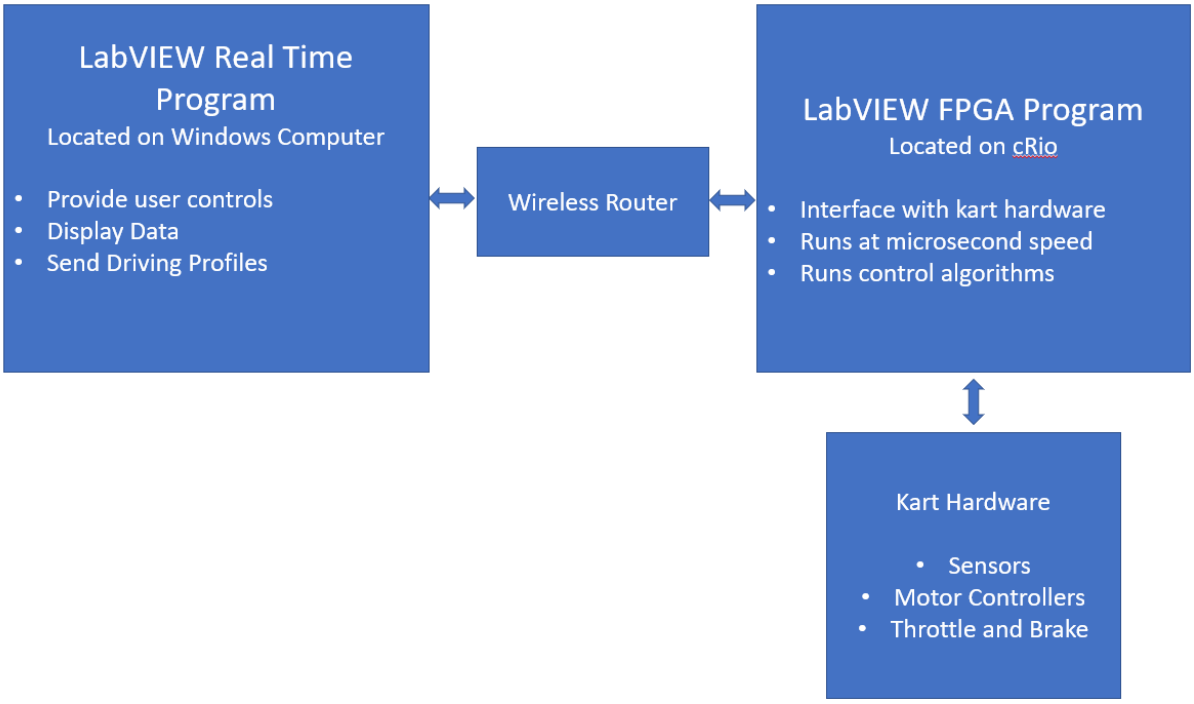

Figure 82: LabVIEW Program Architecture

The real time code serves mostly as a transfer medium of data from the FPGA code to the user, so this section will concentrate on the FPGA code where most of the computations are taking place. The FPGA code consists of 10 loops running simultaneously on the controller. The loops, their purposes, their inputs, and their outputs can be seen in Table 15.

All of the loops in the FPGA run simultaneously which allows for multiple operations and computations to take place at once. It also ensures that operations critical to kart operation are not held up by less critical operations such as sending kart information to the real time code. Most of the loops simply convert sensor signals, or CAN signals into values which can be manipulated, or values into CAN signals for the controllers. The only loop where complex calculations are completed is loop 6 where the throttle and brake signals to the flywheel motor controller are calculated. This loop carries out the algorithms derived in Appendix A.

Table 15: Loops in FPGA and Descriptions

Loop #	Purpose	Inputs	Outputs
1	Read throttle signal from throttle Pedal	PWM signal from rotary encoder	Duty cycle (throttle signal)
2	Read brake signal from brake pedal	PWM signal from rotary encoder	Duty signal (brake signal)
3	Write throttle and brake signals to Sevcon traction motor controllers	• Computer or kart throttle (T/F) • Computer or kart brake (T/F) • Brake pedal duty cycle • Throttle pedal duty cycle • Comp throttle value • Comp brake value	• Throttle signal in CAN to Sevcon controllers • Brake signal in CAN to Sevcon controllers
4	Read CAN signals from Sevcon traction controllers	• CAN signal from left traction motor • CAN signal from right traction motor controller	• Left wheel voltage • Left wheel current • Left wheel speed • Right wheel voltage • Right wheel current • Right wheel speed
5	Read CAN signals from flywheel controller	CAN signal from controller	• Flywheel voltage • Flywheel current • Flywheel speed

6	Calculate flywheel throttle and brake from algorithms	• Traction throttle • Traction brake • Traction wheel speed • Flywheel speed • Pre-charge Throttle • Pre-chare (T/F)	• Flywheel throttle • Flywheel brake
7	Write throttle and brake signals to flywheel controller	• Calculated throttle from algorithm • Calculated brake from algorithm • Computer brake value • Computer throttle value • Computer or algorithm brake (T/F) • Computer of algorithm throttle (T/F)	• Throttle in CAN to flywheel controllers • Brake in CAN to flywheel controller
8	Read voltage and current signals from sensors	• Analog signal from current sensor • Analog signal from voltage divider	• Current at battery • Voltage at battery
9	Capture signals from real time program	• Flywheel computer or algorithm • Traction motors computer or kart • Traction motor throttle computer • Traction motor brake computer	• Flywheel computer or algorithm • Traction motors computer or kart • Traction motor throttle computer • Traction motor brake computer

10	Capture signals from FPGA and send to Real Time as bundle	• Voltage • Current • Left side controller current • Left wheel speed • Flywheel speed • Flywheel throttle • Flywheel current • Right side controller current • Right side wheel speed • Brake • Throttle • Flywheel Brake • Flywheel Battery Voltage	Bundle of Values

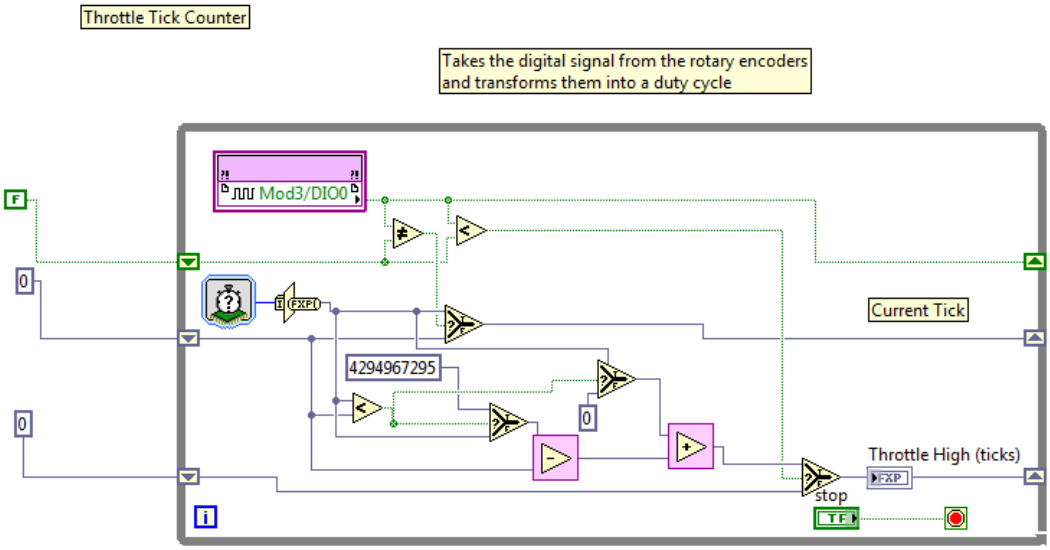

Figure 83: Loop 1, loop which reads the PWM coming from throttle encoder and outputs throttle duty cycle

Figure 83 shows loop 1, which reads the PWM signal from the throttle pedal encoder and translates the signal into the length of time the PWM signal was "high". The longer the "high" portion of the PWM, the further the pedal has been depressed. The signal is read through Module 3 on the cRio device, which is a digital input/output module. Figure 84 shows the second loop, which is the same as loop 1, but the loop reads the PWM signal coming from the brake pedal

encoder. The key to these functions performing their intended function is that they run at real time on the cRio off the clock on the device.

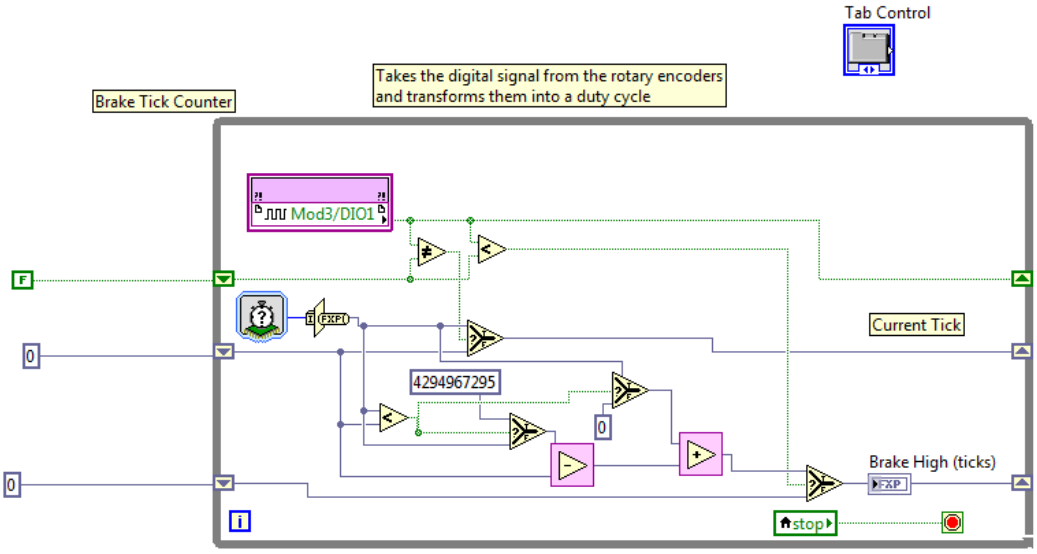

Figure 84: Loop 2, loop which reads the brake pedal PWN and converts to a brake duty cycle

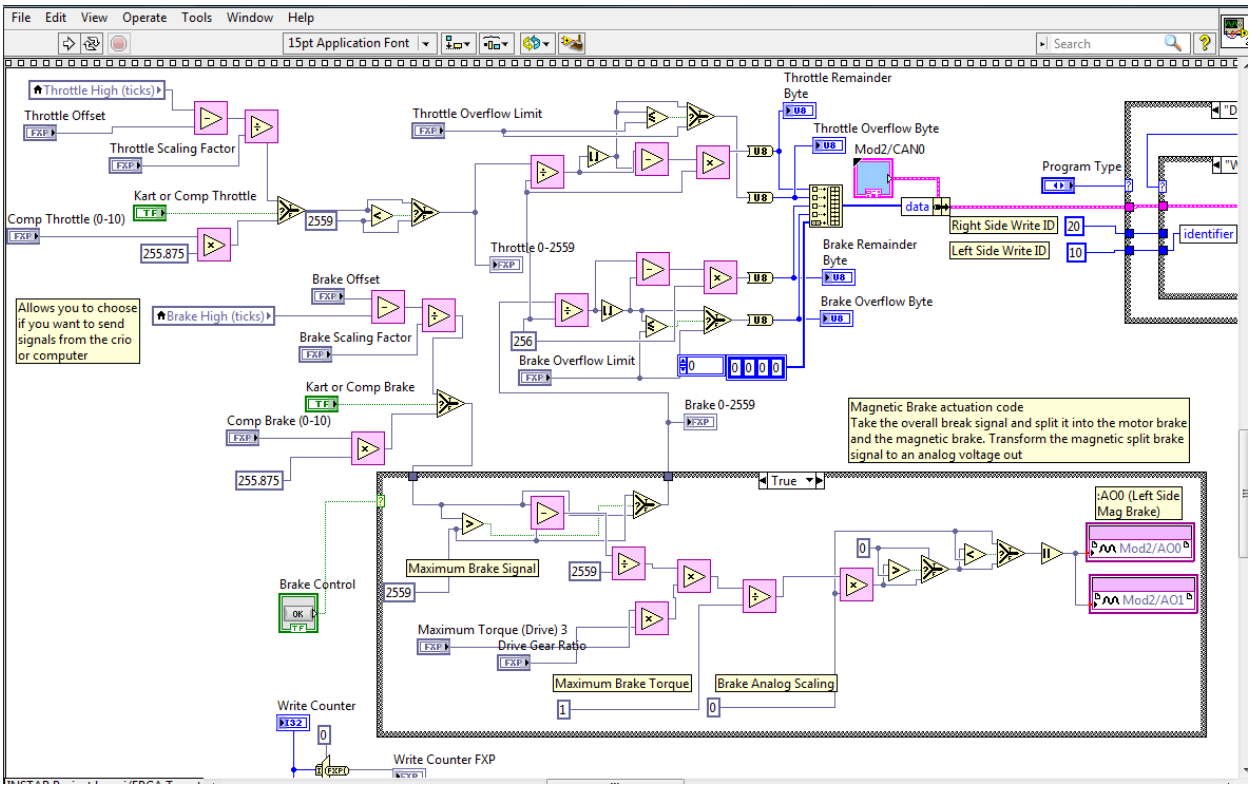

Figure 85: Loop 3, loop which writes throttle and brake signals to the traction motors. Only around 90% of the loop can be seen here because of LabVIEW's lack of a zoom feature

Figure 85 shows loop 3, which is responsible for writing the throttle and brake signals calculated by the program to the traction motors as CAN signals. The loop also has a magnetic brake actuation code, which is legacy and not operational in the context of this experiment. The loop has a selection feature which switches the throttle and brake between pedal signals and computer control signals. This is a T/F indicator selected by the user on the Real time front panel. If the pedal signals are selected, then the loop converts the duty cycle of the pedal inputs to a value 0-2556. If the computer signals are selected, the input (0-10) is converted to a 0-2556 range. A 0-2556 range is used because the controller operates on hexadecimal. This value (0-2556) is then converted to a CAN signal, and sent through the second module on the cRio which is a CAN communication module.

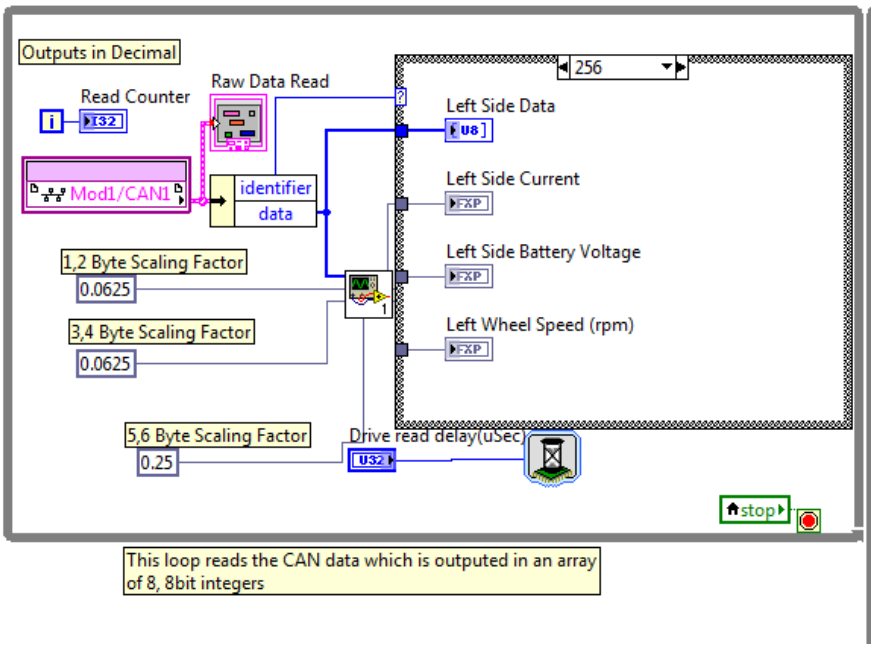

Figure 86: Loop 4, loop which reads CAN signals coming from traction motors

Figure 86 and Figure 87 show loops 4 and 5 respectfully. These loops read the operating conditions of the traction motors and flywheel. The input to the loops is the CAN signals from module 2 on the cRio chassis, which is then fed to a CAN signal processor which extracts the data and the identifier. This is sent to another processor which converts the CAN data to fixed point numbers. The Loops process data for Motor current, motor voltage, and motor speed.

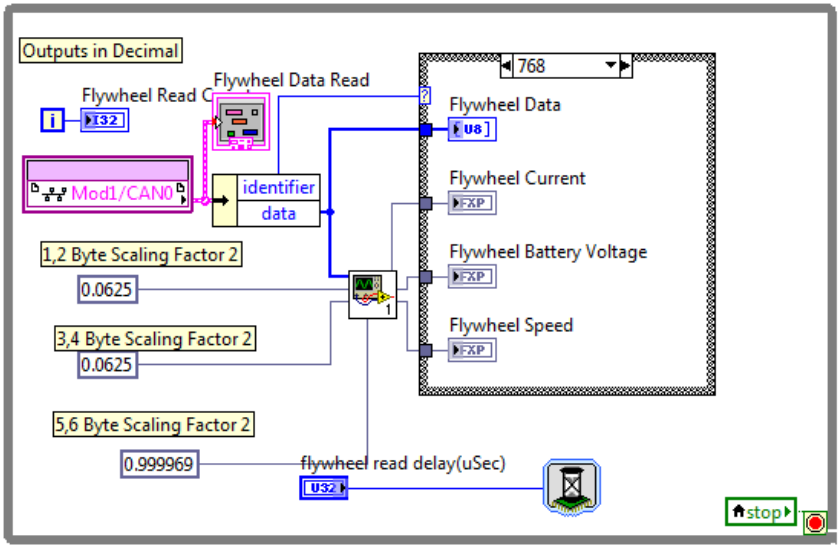

Figure 87: Loop 5, loop which reads CAN signals coming from flywheel motor controller, Loop 7 is identical, except will communicate with the flywheel controller

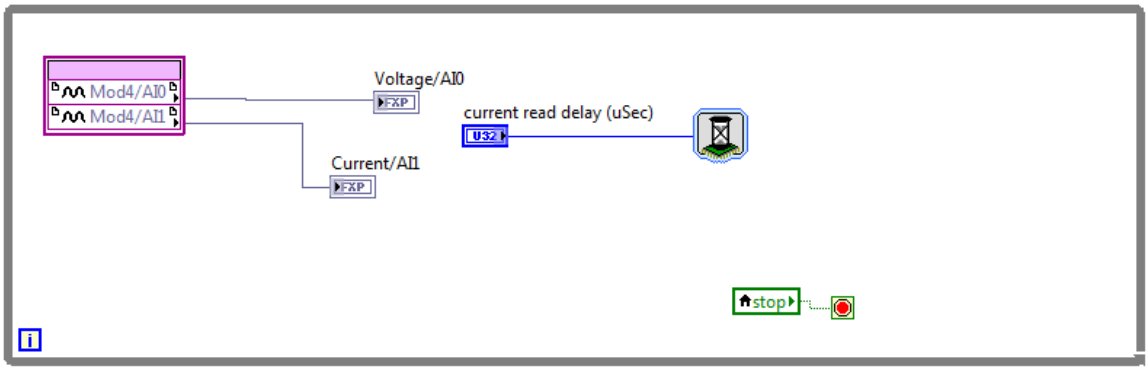

Figure 88: Loop 8, loop which reads the signals from the current sensor and voltage divider

Figure 88 shows loop 8, which reads signals voltages by module 4 on the cRio chassis, which is an analog input module. This data is read and stored as current and voltage signals. This data is then converted in the real time portion of the program to the actual voltages and currents the devices are reading.

Figure 89 shows the loop which runs the algorithms for the throttle and brake signals sent to the flywheel. These algorithms have been detailed previously in the paper, and can be seen in Appendix A. The inputs to this loop are traction throttle, traction brake, traction wheel speed, and flywheel speed. In addition, there are several filters applied to filter out some unwanted disturbances inherent in the algorithm's application. In the code, the maximum throttle signal to the flywheel is set to 400, and anything over 400 is reduced to that value. This eliminated overreaction by the algorithms when the flywheel has zero initial speed at the beginning of a braking event. Similarly, the maximum braking signal allowed by the braking algorithm is 1900, which eliminates unnecessary hard braking by the flywheel algorithm. The code also makes a provision to override the algorithm to send throttle signals to the flywheel when it is desire for the device to be pre-charged.

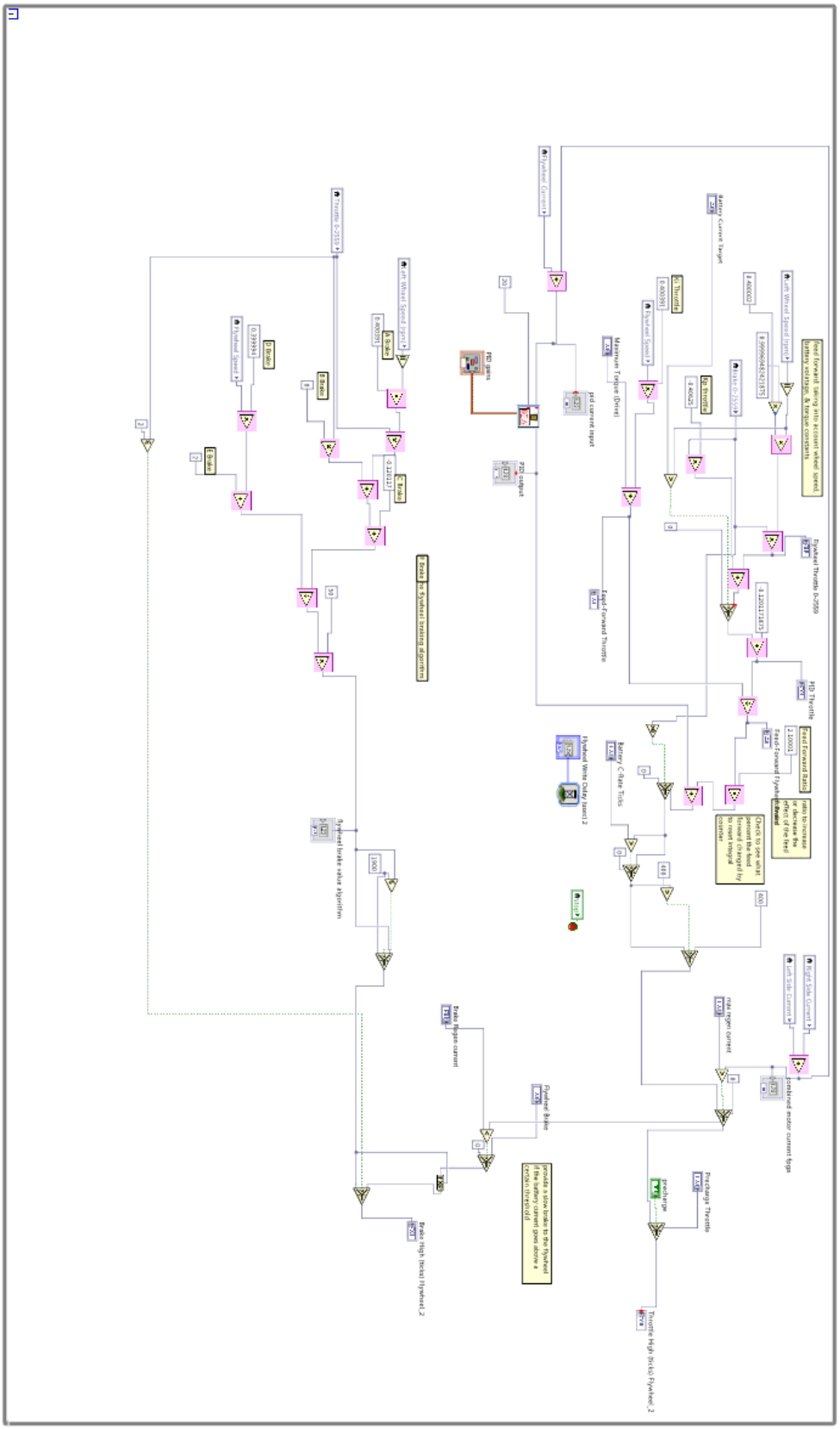

Figure 89: Loop 6, Loop which calculates the flywheel throttle and brake signals from the algorithm